Transverse mechanical responses of unidirectional fibre-reinforced polymers: DEM simulation and deep learning prediction

Submitted by:

Xiaoxuan Ding

This dissertation is submitted for the degree of Doctor of Philosophy

2023

Lancaster University

School of Engineering

Declaration

This thesis has not been submitted in support of an application for another degree at this or any other university. It is the result of my work and includes nothing that is the outcome of work done in collaboration except where specifically indicated. Many of the ideas in this thesis were the product of discussions with my supervisors Prof. Jianqiao Ye, Dr. Xiaonan Hou and Dr. Min Xia.

Excerpts of this thesis have been published in the following conference manuscripts and academic publications.

1. ***Predictions of macroscopic mechanical properties and microscopic cracks of unidirectional fibre-reinforced polymer composites using deep neural network (DNN)***
    - Authors: Xiaoxuan Ding, Xiaonan Hou, Min Xia, Yaser Ismail, Jianqiao Ye
    - Journal: Composite Structures
    - Year: 2022

2. ***Effects of defects on the transverse mechanical response of unidirectional fibre-reinforced polymers: DEM simulation and deep learning prediction***
    - Authors: Xiaoxuan Ding, Zewen Gu, Xiaonan Hou, Min Xia, Yaser Ismail, Jianqiao Ye
    - Journal: Composite Structures
    - Year: 2023

Xiaoxuan Ding and full qualifications

Lancaster University, UK

Abstract

Fibre-reinforced polymer (FRP) composites have broad applications in automotive, aerospace, construction, and marine sectors due to their excellent physical and mechanical properties, such as lightweight, high strength, high stiffness, and corrosion resistance. Laminated FRP composites are among the most commonly used FRP composites that consist of several unidirectional (UD) FRP laminae, which were also widely used. However, predicting mechanical properties and damage progression of UD FRP composites at the laminae scale with high accuracy is still a challenging problem as the damage evolution and failure mechanism is obviously far more complex than those of monolithic materials, and a precise approach is usually time-consuming.

In this thesis, firstly, a 2D plane strain computational micromechanics Discrete Element Method (DEM) model is used to investigate the mechanical behaviour of a UD FRP composite lamina subjected to transverse loading. The damage progression and stress-strain response of the laminae are analysed. The DEM simulation results agree with those from the FEM and experimental tests, which can offer accurate and reliable results for machine learning predictions. Thus, a deep neural network (DNN) model for predicting the macroscopic transverse mechanical properties of UD FRP lamina is investigated when considering the different fibre radii and ratios. The DNN model has a strong ability to predict both the transverse tensile strength and Young's modulus of the UD FRP composite lamina accurately. Then the predictive models for predicting the microscopic cracks are constructed. Two simple ML models are first generated based on the data extracted from 500 DEM model simulations. However, the prediction results indicate that the relation to the target problem is complicated. The deep learning (DL) model is therefore developed to explore the complex inner relation of the prediction problem. Based on the results of 1600 DEM simulations, a multi-layer DNN model with

back-propagation is constructed for the predictions of the crack areas of an FRP composite lamina. It can be found that most of the initial cracks and the overall trends of cracking paths can be predicted successfully. Then, a DNN model is applied to predict the initial and second crack in order in the FRP laminae to obtain a fast determination of the crack initiation, which results could demonstrate the feasibility and effectiveness of the method.

In addition to the defect-free UD FRP lamina, the transverse mechanical response of defective lamina is studied using the DEM model. The DEM model is recalibrated for analysing the effects of the presence of defects in the RVE of the lamina. The crack initiation and propagation in defective RVEs with different fibre distributions are analysed and compared. In addition, the effects of the radii of matrix defects and the distribution of defects on stress-strain responses are also investigated, which shows excellent capabilities in predicting mechanical behaviour. It is found that the crack initiation is highly dependent on the defects. Therefore, back-propagation deep neural network (DNN) models are developed to quickly determine crack initiation and instantaneous critical load of the RVEs based on the data generated by 1000 DEM simulations. The results show that the initial crack and the critical stress of the laminae can be accurately and efficiently predicted by the data-driven DNN models with full consideration of randomly distributed defects.

Acknowledgements

Firstly, I would like to express my thanks to my patient and supportive supervisors, Prof Jianqiao Ye, Dr Xiaonan Hou and Dr Min Xia, who have supported me throughout this research project. It was a great privilege and honour to study and work under their guidance. Their guidance helped me a lot in all the time of research and writing of this thesis.

Secondly, I would like to give special thanks to my parents for their endless love, and unhesitating support they have given to me throughout my life. I would also like to say a big thank you to my husband, Dr. Zewen Gu, for his unconditional love and company, especially the constant encouragement when I encountered difficulties.

Finally, many thanks to my friends I met and spent a happy time with at Lancaster University, UK. I am also very grateful to my two best friends in China, Huiying and Teng, for their encouragement in remote chat, making my doctoral life happier and more fulfilling.

List of Tables

List of Figures

Contents

Chapter 1

1 Introduction

1.1 Background

Fibre-reinforced polymer (FRP) composites have been a popular research area for many years. They have many attractive material properties characterized by lightweight, high strength, high stiffness, and corrosion resistance, making them suitable for many structural applications such as the aerospace industry, the automotive industry, and wind power generation [1]. A major concern in the use of composite materials is the susceptibility to damage resulting from the intrinsic microstructures under complicated external loading. Due to the complex nature of fibre-reinforced composite materials, the onset of damage does not cause the instantaneous failure of the entire structure. Unidirectional fibre-reinforced polymer composite laminates (UD FRPs), as one type of FRP composites, have excellent physical and mechanical properties along the fibre direction. It was relatively difficult to study the microscope mechanisms (e.g., failure strength, damage evolution, etc.) of the UD FRPs in the plane perpendicular to the fibres through experimental tests due to the limitation of the testing environment, the complex implementation of loadings and the complex damage progression. To a certain level, this leads to the overestimation of damage evolution and the failure strength of composites, which means that the capture and usage of their excellent properties cannot be maximized.

One way to study the transverse mechanical behaviour of a UD FRP lamina in the plane perpendicular to the fibres is to conduct experimental tests. However, these tests are typically costing, and the results may not be reliable due to the limitations in

implementing realistic environment and loading conditions and the complex and random nature of damage progression. Alternatively, analytical micromechanics models have been used to predict the mechanical properties of FRP composites. Typically, in an analytical micromechanics model, fibres and matrix are assumed to be homogeneous, linearly elastic and isotropic. More recently, various numerical methods have been used for the micromechanical analysis of composite laminae.

However, it was found that numerical simulation from micromechanical analyses is a significant computational challenge for the computer. In recent years, the rapid development of data science and machine learning techniques has helped new engineering applications due to their high efficiency, great potential in dealing with big data and accurate prediction ability. A machine learning model, once it is properly trained, is very computationally efficient and requires only simple inputs with minimum human involvement. Machine learning (ML) has been used in various studies on composite materials based on either experimental or numerical simulation data.

1.2 Aims and Objectives

Understanding mechanical behaviour of composites is very important for using composites to the maximum potential. This thesis aims to provide accurate and robust data-driven models for predicting transverse mechanical response of unidirectional (UD) fibre-reinforced polymers (FRP) based on numerical simulation data. Machine learning (ML) has a wide range of applications in engineering sectors, which shows its efficiency and accuracy in dealing with complex engineering problems. ML technology analyses the features provided by the users, learns the relation from the inputs and output in the datasets, and then makes predictions for the unseen data. ML predictions depend heavily on the quality and size of data. Due to a lack of experimental data on transverse

mechanical responses of UD FRP, a computational micromechanical model needs to be developed first to provide accurate, experimentally validated data for machine learning models. The main aims and objectives of this study are as follows:

1. To develop a 2D RVE-based DEM model for studying the transverse mechanical behaviour of both the defect-free and defective UD FRP laminae.
2. To develop machine learning approaches based on the data obtained by DEM simulations to predict macroscopic mechanical properties and microscopic crack patterns in defect-free UD FRP laminae.
3. To develop DNN predictive models based on the data obtained by DEM simulations to predict the crack initiation in UD FRP laminae.
4. To develop DNN predictive models based on the data obtained by DEM simulations for the predictions of the initial crack and its instantaneous critical load in defective UD FRP laminae with two periodic distributions of fibres.

In this thesis, the 2D RVE-based DEM model reveals advantages in both predicting mechanical properties and studying the crack evolution of UD FRP laminae. As there are no ML based studies on the stiffness, strength, initial crack patterns, and fracture of UD FRP composites with consideration of randomly distributed fibre or defect position in the literature, the developed data-driven predictive models based on the data of DEM simulation represent a pioneer investigation on predictions of mechanical properties and crack patterns in materials of random anisotropy.

1.3 Thesis structures

The thesis is divided into six chapters.

Chapter 1 demonstrates the background of the studies in composite materials and mentions the challenges and difficulties in precisely investigating its mechanical response. The methods and objectives for solving this problem are also addressed in this chapter.

Chapter 2 contains a literature survey. It starts with an introduction to composite materials. Then the micromechanical analytical and computational modelling of the mechanical behaviour in the UD FRP composite is presented and compared. Lastly, the framework of machine learning (ML) and its applications in composites are introduced and discussed.

Chapter 3 presents the development of the 2D RVE-based DEM models for the UD FRP lamina, including the model calibration and the process of the RVE generation. Also, the simulation results of the mechanical responses in the UD FRP laminae obtained from the DEM model are analysed and discussed. Then a DNN regression model for predicting macroscopic transverse mechanical properties of FRP laminae is developed. The predictive model is based on a data set generated by 2000 Representative Volume Element (RVE) based Discrete Element Method (DEM) simulations.

Chapter 4 presents the constructions of the machine learning approaches for predicting the microscopic crack pattern of the UD FRP laminae. The first prediction problem is a first try at predicting the crack path based on the DEM simulations of a set of reduced-size RVEs. Two different machine learning models, the Gaussian Naïve Bayes classifier and Artificial Neural Networks (ANNs), will be used to give crack path prediction after training feature data. Then, an improved deep learning (DL) model, a back-propagation deep neural network (DNN) classification model based on the results of 1600 DEM simulations, is developed for predicting microscopic crack areas of the

FRP laminae. In order to obtain the position of initial cracks more efficiently, lastly, DNN models are developed for predicting the crack initiation in the UD FRP lamina. After training suitable and representative features obtained from the DEM simulations, the DNN model will be used for predicting the first and second cracks in the RVE in order.

In Chapter 5, an RVE-based DEM model is developed to study the effect of defects on the transverse mechanical responses in defective UD FRP laminae. The defects in both the matrix and the fibre-matrix interfaces are considered in the RVE. The DNN prediction for the initial cracks in the UD FRP lamina with random fibre distribution shows great potential. Thus, multi-layer DNN regression models with back-propagation are generated to predict the position of the initial crack and the instantaneous critical load of defective FRP composite laminae with two periodic fibre distributions. The data is provided by 1000 RVE-based DEM simulations.

In Chapter 6, conclusions and suggestions for future works are presented. The advantages of the developed DEM model for modelling the mechanical behaviour of UD FRP composite are shown and concluded. The efficiency and accuracy of the DL model for predicting the macroscopic and microscopic mechanical response in UD FRP composite are presented. The novelty of the works stated in the thesis is summarized. Finally, a promising trend of using the DEM and DL models for predicting the mechanical behaviour of composite materials is given.

Chapter 2

2 Literature Review

2.1 Introduction of composite materials

A composite material is composed of two or more constituent materials. Every constituent material has its distinct chemical or mechanical features. Typical composite materials include reinforced concrete, fibre-reinforced metals and fibre-reinforced polymers. Compared to traditional materials, composite materials have excellent material properties for using widely in many structural applications [2-6].

As one type of composite, fibre-reinforced polymer (FRP) is defined as a polymer matrix that is reinforced with fibres. Fibres have excellent properties of high strength and stiffness, which makes FRP a material that has highly specific mechanical properties. There are four categories of FRPs according to their matrix types: polymer matrix composites, metal matrix composites, ceramic matrix composites and carbon matrix composites. According to the arrangement of the fibres embedded in the matrix, there are two categories of FRPs: continuous FRPs and discontinuous FRPs. Thin plies of FRP lamina of unidirectional or woven fibres are always assembled as an FRP laminate. These plies of the same matrix material with the same or different fibre orientations are usually bonded together.

Laminated FRP composites (see Figure 2-1) are among the most commonly used ones. However, predicting mechanical properties and damage progression of UD FRP composites at the laminae scale with high accuracy is still a challenging problem as the damage evolution, and failure mechanism are far more complex than those of monolithic materials. One of the major concerns in using UD FRP composites is their

susceptibility to damage resulting from transverse loading, which results in transverse cracking and fibre-matrix debonding. They are complex processes developing simultaneously on all internal length scales, i.e., from micro to macro scales.

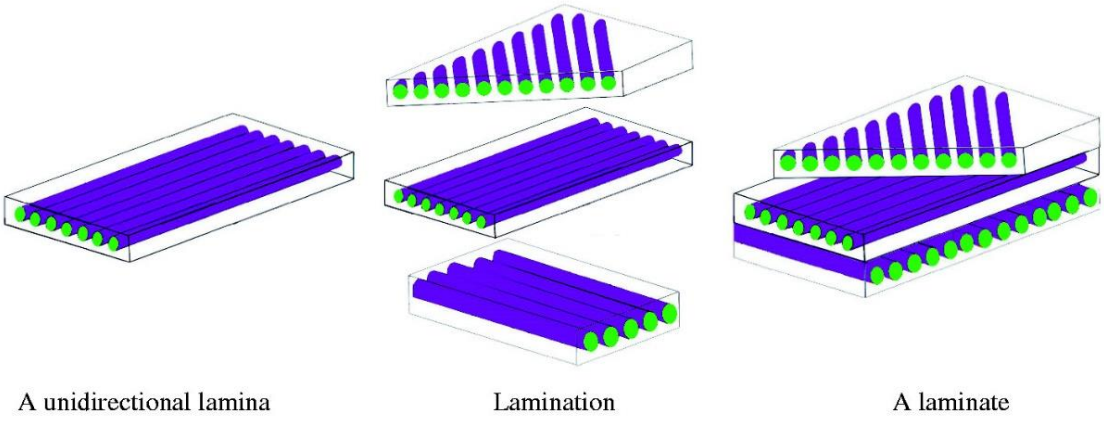

Figure 2-1: Stacking of a number of laminae makes up a laminate [7].

2.2 Analytical models for studying the mechanical properties of FRP composites

2.2.1. Micromechanical analytical modelling of stiffness

Analytical methods are convenient and fast for studying the mechanical properties of the composite from its constituent volume fraction and properties. Transverse properties of UD FRP composites are defined as properties in the direction perpendicular to the fibres (see Figure 2-2). A load of transverse tension is also shown in Figure 2-2.

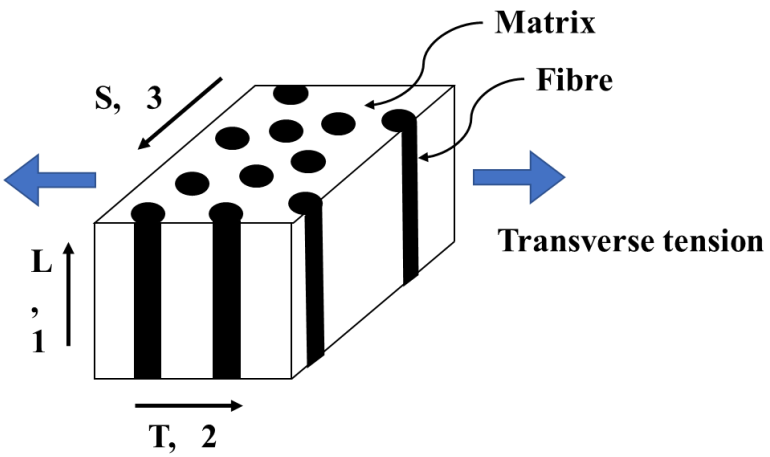

Figure 2-2: UD FRP composite under the loading of transverse tension

2.2.1.1. The slab model

The reinforcements are slabs but not fibres (see Figure 2-3). Thus, this analytical model is called the 'slab' model. It is also called the rule of mixtures method. As shown in Figure 2-3, there is one reinforcement layer between two matrix layers. The total thickness of the composite is t_c, the thickness of the reinforcement is t_f, and the thickness of the matrix is t_m. The transverse elastic modulus E_T given by the slab model is

$$\frac{E_T}{E_m} = \frac{E_f}{V_f E_m + V_m E_f} \tag{2-1}$$

where E_m and V_m are the elastic modulus and volume fraction of matrix, E_f and V_f are the elastic modulus and volume fraction of fibres.

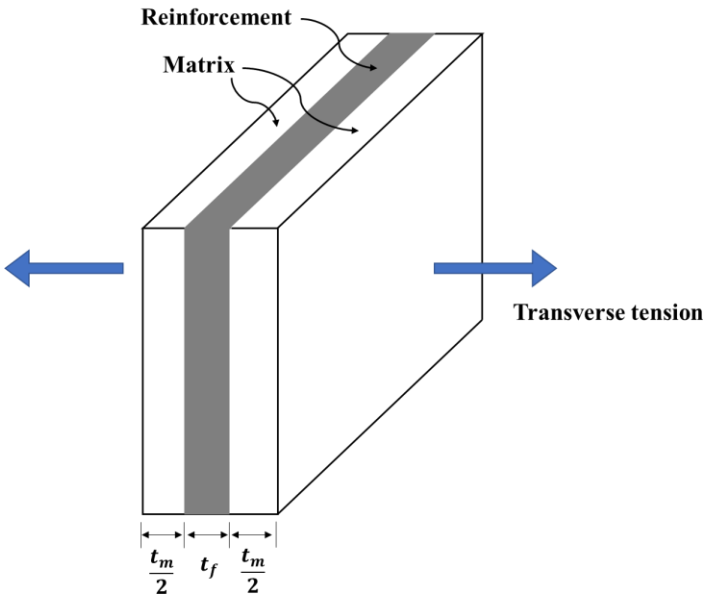

Figure 2-3: The slab model for describing the transverse behaviour of the composite.

2.2.1.2. Halpin-Tsai Equations

The assumptions of the slab model for computing the transverse elastic modulus are relatively too strict, which results in a semi-empirical approach known as the Halpin-Tsai equations. The Halpin-Tsai equations, as the most will-known semi-empirical method, are proposed by Halpin and Kardos [8, 9], and Halpin and Tsai [9],

The transverse Young's modulus is computed as

$$\frac{E_T}{E_m} = \frac{1 + \xi\eta V_f}{1 - \eta V_f} \tag{2-2}$$

where

$$\eta = \frac{\frac{E_f}{E_m} - 1}{\frac{E_f}{E_m} + \xi} \tag{2-3}$$

and $\xi = 2(a/b)$

The ratio a/b is the cross-sectional aspect ratio of the reinforcement (see Figure 2-4).

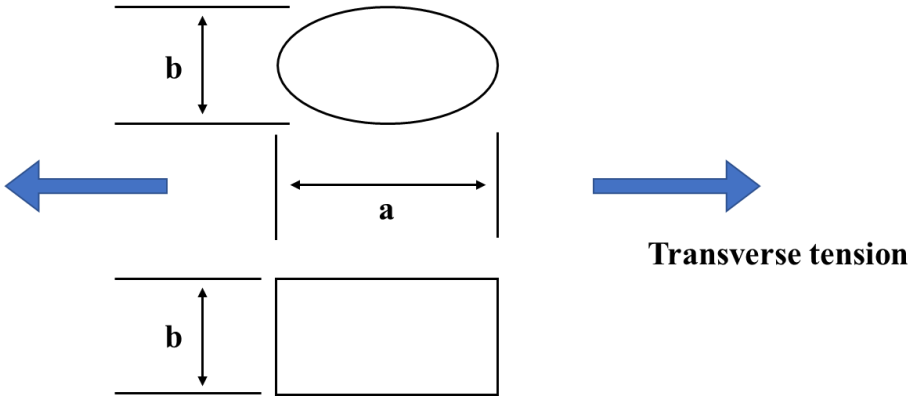

Figure 2-4: The cross-sectional aspect ratio of the reinforcement.

The direction of *a* is the loading direction. The direction of *b* is normal to the load.

For example, Figure 2-5 shows a rectangular cross-section reinforcement.

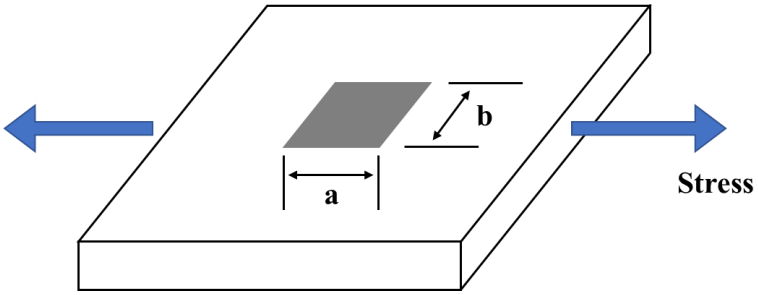

Figure 2-5: An example of a rectangular cross-section reinforcement.

In the case of $\xi = 0$, $a \to 0$, and $b \to \infty$. Figure 2-6 shows this arrangement of the reinforcement.

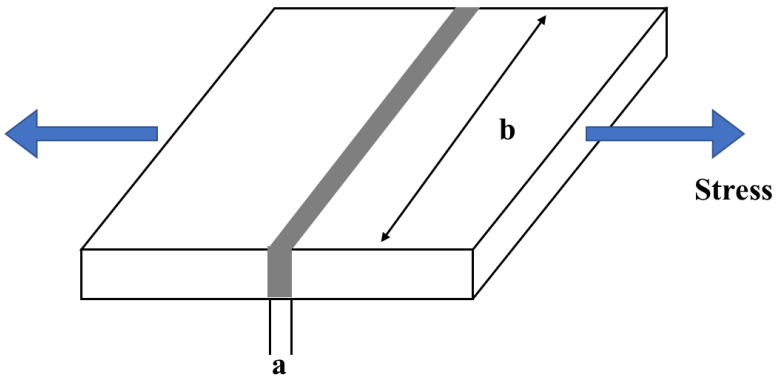

Figure 2-6: The arrangement of the reinforcement for the case of $\xi = 0$.

It can be seen that Figure 2-6 shows the reinforcement shape of the slab model for transverse properties. If substituting $\xi = 0$ into (2-2)

$$\frac{E_T}{E_m} = \frac{1}{1 - \eta V_f} \tag{2-4}$$

and

$$\eta = \frac{E_f - E_m}{E_f} \tag{2-5}$$

Therefore,

$$\frac{E_T}{E_m} = \frac{E_f}{V_f E_m + V_m E_f} \tag{2-6}$$

It can be found that this result is identical to that of the slab model.

2.2.2. Micromechanical analytical modelling of strength

The transverse strength of a UD FRP lamina could also be obtained using a micromechanics approach considering the properties of fibre and matrix constituents. The strength was found to be sensitive to different parameters, such as fibre distribution, the fibre-matrix interface, etc. Several different methods were proposed for obtaining the tensile strength of a UD FRP lamina [7]. One is called the strength of materials approach. In this approach, assumptions were considered. The transverse tensile strength is computed as the production of the transverse elastic modulus and the ultimate transverse failure strain. The ultimate transverse failure strain is obtained in terms of the transverse properties of the fibres and matrix. In addition, there is another model called the Bridging model. Huang [10] derived the ultimate tensile strength by assuming that fibres and matrix are linear elastic until rupture and elastic-plastic, respectively. The stress in the matrix is related to the corresponding stress of the fibres by using the

bridging matrix. In this way, the stresses in fibres and matrix, and the tensile strength can be obtained by determination of the bridging matrix.

2.3 Micromechanical computational models used in FRP composites

In addition to the analytical methods for studying the mechanical behaviours of the composites, micromechanical computational models can also be used to accurately predict the effective properties of composites and simulate the stress-strain responses, the damage evolution, and the failure strength under a specific loading. In a micromechanical computational analysis, fibres in the UD FRP lamina with their distribution embedded in the matrix are generated in a representative volume element (RVE) (see Figure 2-7). The influence of the geometry and spatial distribution of the constituents of the composite can be accurately considered.

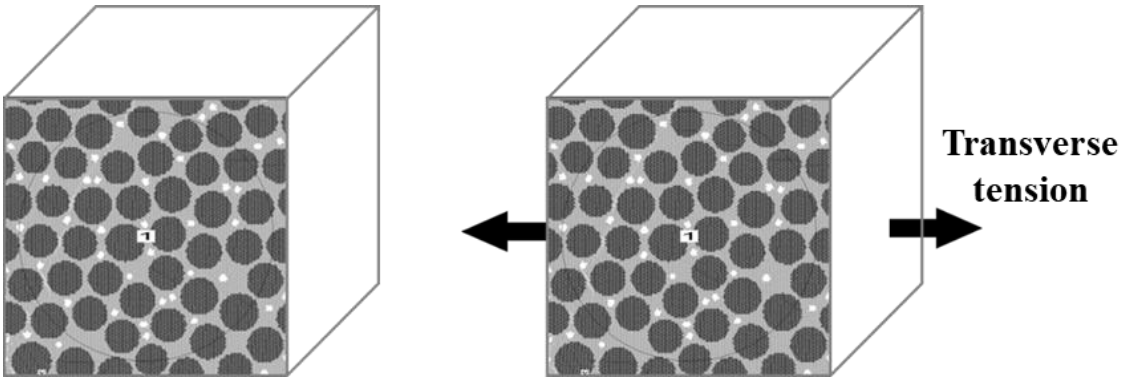

Figure 2-7: The microstructure and micro mechanism of UD FRP composites

2.3.1. Development of the representative volume element (RVE)

With the development of computer-based simulation, the mechanical behaviour of composites has been studied using the micromechanical computational model in the last

few decades. It is usually analysed through a representative volume element (RVE). RVE was first introduced by Hill [11], which is a small sub-region of the composites. The RVE of the composite needs to be small but contains sufficient information, for example, enough fibres within the RVE, for analysing its behaviour.

The development of RVE allows the random generation of fibres with their distribution embedded in the matrix according to a specific fibre volume fraction. Several approaches have been presented in the literature for generating the statistically equivalent RVEs (SERVEs) of composites with uniform or non-uniform distributions of fibres. A SERVE is the smallest sub-region of the composite, and its mechanical behaviour is the same as that of the entire composite [12]. Therefore, the RVE size should be suitable for the computational simulation. Some recent studies found that a few dozen fibres in the RVE were sufficient for studying the micromechanical behaviour of UD FRP lamina [13-16].

For the generation of SERVEs of UD FRP composites, experimental image-based models have been presented in the last few decades [17-18]. In the generation process, digital images of the cross-section of the composite are first obtained by scanning electron microscopy (SEM) or high-resolution light microscopy. Then, computer software is used to locate the fibres according to the digital images. The image-based approach showed its advantage in generating exactly the same microstructure as the cross-sectional area of the composites. However, it always costs much more computer time for image processing.

In addition to the experimental image-based models, there were also numerical approaches. The hard-core model, which is simple to achieve, was commonly used. In the hard-core model, the fibres are distributed randomly without overlap in the domain of a SERVE. The limitation of this model is that it cannot generate SEREVs with a fibre

volume fraction higher than 50% due to a jamming limit [19]. To overcome this limitation, Wongsto and Li [20] developed a method that allowed uniformly arranged fibres to collide with each other to achieve a higher volume fraction and random distribution. Melro et al. [21] constructed a relatively complex algorithm that used the classical hard-core model to generate an initial fibre distribution. Then, they applied very small displacements to the fibres for their random distribution with higher fibre volume fractions. However, this algorithm was complex in implementing the movement of fibres in the domain. Then Yang et al. [22] developed a simpler algorithm called random sequential expansion (RSE) based on the hard-core model. The limitation of this approach was that the radii of fibres must be constant. Moreover, the inter-fibre distance had to be zero if the fibre volume fraction was 68%. This may result in difficulties in the computational simulations of RVEs because there needs to be a certain distance between two adjacent fibres.

To overcome these limitations, a new numerical model based on the Discrete Element Method (DEM) and experimental data of fibre diameter distribution was proposed by Ismail et al. [23]. This approach was implemented in the DEM software package 'PFC 2D'. The diameters of the fibre followed a normal distribution with a mean of $6.6\mu m$ and standard deviation of 0.3106 [16]. The generation process is as follows:

1. Considering a fibre volume fraction of 60%, the required number of fibres, N_f, is approximated calculated by:

$$N_f = \frac{4V_f L^2}{\pi \bar{D}_f{}^2} \tag{2-7}$$

where $\bar{D}_f$ is the mean of the fibre diameter. The diameter of the generated fibres is calculated using a random number, α, in the range of $[-1, 1]$ as:

$$D_f = \overline{D}_f + \alpha\delta_f \quad (2\text{-}8)$$

where δ_f is the standard deviation of the fibre diameter.

2. The fibres are initially packed in a rectangular arrangement (see Figure 2-8(a)). The fibre volume fraction may be smaller than the target fibre volume fraction as the diameters of the generated fibres are not identical. As shown in Figure 2-8(b), more fibres will then be added to achieve the target volume fraction. A random velocity is applied to the fibres like the Brownian motion, which may move some fibres outside the domain of the RVE. To solve this problem, the same number of fibres are added to the RVE from the opposite boundary of the domain to compensate the fibres that have moved outside the domain. This process is called applying the periodic condition in the DEM software package 'PFC 2D'. As shown in Figure 2-8(c), the blue and red fibres are the paired fibres following the periodic condition.
3. As the fibres are randomly moved, some overlaps between fibres may occur. Thus, the radii of the fibres are increased by half the required minimum distance between two neighbouring fibre surfaces before applying the velocity to the fibres. After the distribution of fibres stabilises, the radii of the fibres are reduced to return to the initial values.

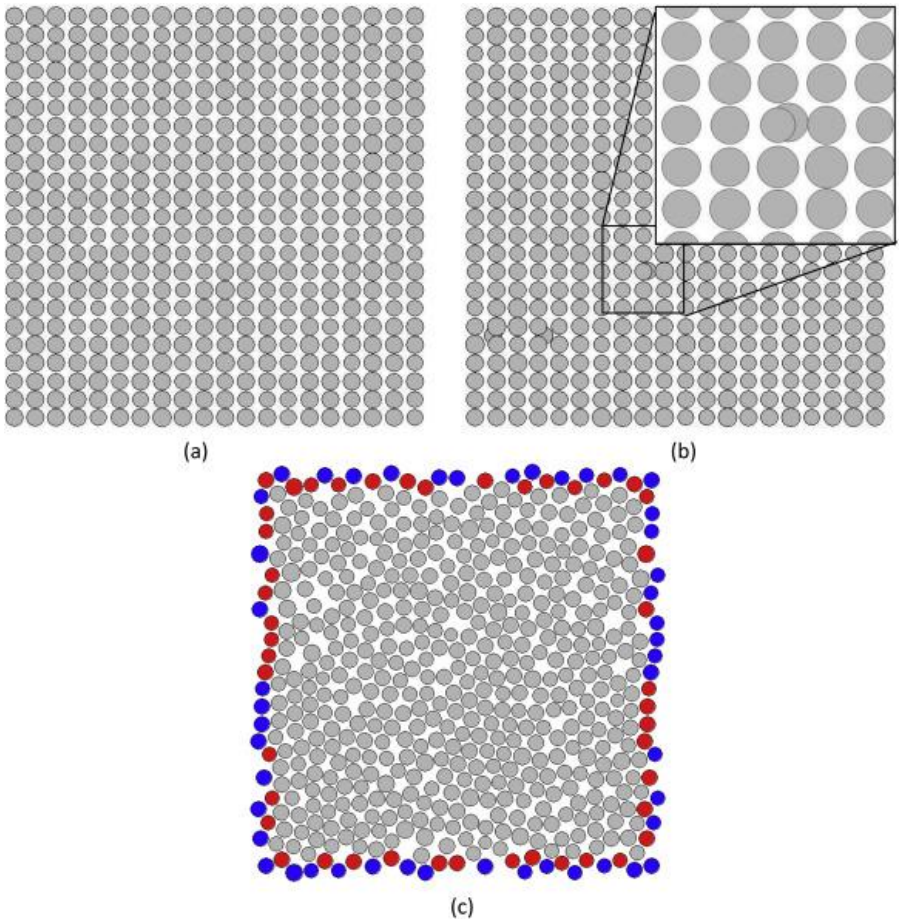

Figure 2-8: Procedure for generating random fibre distributions using DEM. (a) Initial fibre distribution rectangular arrangement. (b) More fibres are added in. (c) Periodic boundary condition is applied to maintain the constant fibre volume fraction [23].

This approach overcomes the jamming limit and can be used to generate randomly distributed fibres with high-volume fractions and any specified inter-fibre distances. In addition, the RVE generated by this approach showed good agreement with experiments in all statistical analyses. The elastic properties of the generated RVEs are better than those of the RVEs obtained by previous approaches. The developed algorithm can be suitable for the computational micromechanical modellings of the elasticity, strength, failure, and damage progression.

2.3.2. Micromechanical computational modelling for FRP composites

The multi-scale computational homogenization modelling approach is an alternative approach to studying the mechanical behaviour of heterogeneous materials, such as composite materials. In contrast to the analytical and semi-analytical models, the behaviour of each constituent and the interactions between them can be studied within the computational homogenization modelling.

In the last two decades, many studies have been presented on predicting mechanical properties of UD composites using micromechanical computational modelling, including strength, stiffness and failure [7]. For instance, Sun and Vaidya [24] determined the elastic constants of unidirectional fibre composites using finite element analysis of a representative volume element (RVE). The simulated elastic constants agreed well with existing theoretical predictions and available experimental data. Gusev et al. [25] employed the Monte Carlo procedure to generate periodic computer models with unit cells containing randomly distributed fibres and used Monte Carlo models to calculate the composite elastic constants. It was found that the fibre distribution affected the transverse composite elastic constants more than the fibre diameter did.

Computational micromechanics using the finite element method (FEM) has been widely employed for studying damage evolution and failure. Several studies began with the micromechanical analyses of unit cells. Li [26] generated square and hexagonal unit cells of the fibre arrangements and employed the FEM to model their mechanical behaviours with appropriate boundary conditions. Zhang et al. [27] developed a micromechanical FEM model for investigating the damage evolution of unidirectional fibre-reinforced polymer laminates. They also generated a three-dimensional periodic unit cell containing a fibre embedded in the matrix. The nonlinear viscoelastic and

cohesive models were used to study the deformation of matrix and the progressive interface debonding. Numerical results were obtained to reveal the local and global response of the laminate, including the damage mechanism. The simulated damage progression was in good agreement with that of the experimental test.

Wongsto and Li [20] studied the effects of incorrectly prescribed boundary conditions on the behaviour of UD FRP. They first used micromechanical finite element analyses of 'unit cells' of UD composites. Correct deformation and stress distribution were obtained from a sub-domain of the unit cell with incorrectly prescribed boundary conditions. Then they extended to study the behaviour and effective properties of UD composites with fibres distributed randomly over the transverse cross-section, which results were also reliable.

Then, using micromechanical FEM models to study the mechanical behaviour of UD composites with randomly distributed fibres over the transverse cross-section started attracting attention [14, 15, 28-32]. The studies include the stress-strain response, damage evolution ductility, effects of fibre–matrix debonding, etc. Specifically, Gonzalez and Llorca [28] studied the mechanical behaviour of UD FRP composites under the loading of compression perpendicular to the fibres by means of the finite element analysis of an RVE of the composite microstructure. In their study, the matrix was assumed isotropic and its behaviour was modelled by elasto-plastic constitutive model following the Mohr-Coulomb yield criterion. The fibre-matrix interface was modelled by cohesive zone model. It was found that the mechanical properties under transverse compression were mainly controlled by interface strength and matrix yield strength in uniaxial compression. Other parameters, such as matrix friction angle, interface fracture energy and thermo-elastic residual stresses, played a secondary role in the composite mechanical behaviour.

To examine the influence of the interface properties on the transverse mechanical behaviour of composites, Wang et al. [29] developed a two-dimensional (2D) finite element analysis to study the effects of the interphase properties on both the effective transverse properties and damage behaviour of composites. The results showed that effective transverse properties, damage initiation, and evolution depended highly on the interphase properties. Vaughan et al. [14] also developed a finite element model to study the influence of the intra-ply properties on the transverse shear deformation of a carbon fibre/epoxy composite material, which showed similar behaviour to the in-situ experimental observations.

Yang et al. [15] studied the microscopic failure mechanisms of UD FRP composites under transverse tension and compression using micromechanical FEM analysis. They used the Drucker-Prager yield criterion, rather than Mohr-Coulomb yield criterion to predict yielding of the epoxy matrix, which can take into account the progressive failure behaviour of the matrix. The simulated stress-strain responses gave reasonable results of the tensile and compressive strength of the composites. The failure mechanisms of the composites under transverse tension and transverse compression obtained using the FEM are discussed and compared. It was concluded that the tension fracture started from interfacial debonding and propagated along with matrix plastic deformation, while the compression failure was mainly caused by matrix plastic damage. It was also found that the damage behaviour was affected by the interfacial properties (including the interfacial stiffness, interfacial strength, and interfacial fracture energy), which provided useful information on the selection of interfacial properties that may be used in the micromechanical analysis of composites to ensure reasonable results.

Naderi et al. [31] proposed an augmented 3D FE analysis to study the influence of fibre–matrix interface fracture properties on the failure behaviour of fibre-reinforced

composites subjected to transverse tensile loading. The study considered the influence of the random distribution of fibre arrangement, stochastic distribution of interfacial properties, and circular and elliptical fibre shapes in the simulation of different RVEs. The 3D FEM simulation results clearly revealed the statistical effect of interfacial fracture properties on the load–deflection response. The simulated damage pattern on the RVE showed that the weak interfaces are not always the locations for dominant microscopic cracks. Other important factors, such as fibre packing density, neighbour interface properties, degree of the enriched region with matrix, and shape and size of the fibre, affected the failure path.

Moreover, Ghayoor et al. [32] analysed a large number of RVEs with different random microstructures using the FEM. They found that the predicted values for stress concentrations and stress distributions in the matrix of a composite were affected by the random microstructure of the RVE. It was shown that the maximum stress in the matrix was largely dependent on the random morphology, minimum distances between fibres, and volume fraction.

In general, it can be concluded that the micromechanical computational model used in the above studies can be used as an efficient computational tool for predicting material characteristics, which are beneficial for designing high-performance composite materials.

2.3.3. Micromechanical computational modelling for defective FRP composites

Defects are usually formed unavoidably in the manufacturing process of composites [33-37], which adversely affect the mechanical properties of the composites. The effect of defects on the mechanical behaviour of composites is a relatively complicated

problem as the diversity of the defects, such as the shape, the size, and the location, for instance, the defects could exist within the matrix or along the fibre-matrix interface. Studies on the effects of defects on the mechanical behaviours of FRP composites have been conducted for many years [38-41].

Computational micromechanical modelling has been widely used to analyse the mechanical responses of composites with defects. The influences of pressure-sensitivity and plastic dilatancy on voids shape and microvoid interaction were studied using the finite element method (FEM) [42]. It was found that the mechanical strength of the material was weakened by an increasingly oblate void. Moraleda [43] et al. used a computational micromechanics approach to study the finite deformation of porous elastomers. RVEs of the microstructure containing randomly distributed circular voids were generated and simulated under three different loading modes (in-plane isotropic elongation, uniaxial elongation, and uniaxial traction). For materials with initial porosities of 5%, 10% and 20%, their corresponding stress-strain curves and microstructural evolution as a function of the applied deformation were given. Liebig et al. [44] worked on an FEM investigation of the effects of voids on the failure mechanism of FRP under compression loading. The results showed that stresses concentrated in the matrix due to matrix voids caused by fibre/matrix debonding and kink-band formation of fibres. This micromechanical analysis focused on examining a single void on the compressive failure of the FRP composites without considering the interactive effects of multiple voids.

In addition, Vajari et al. [45, 46] used the FEM to simulate the mechanical behaviours within a representative volume element (RVE) of porous UD FRP composites subjected to different loading. In their study, two different populations of voids were explicitly represented in the RVE of the microstructure, namely, inter-fibre

voids and circular voids within the matrix. It was found that the crack path and strength of composites were significantly affected by the presence of voids. It was also found that damage often initiates around the inter-fibre trapped voids as inter-fibre voids acted as stress concentrators. The circular voids in the matrix affected the crack propagation when the matrix deformation in the microstructure. However, the use of the cohesive zone model requires that the possible paths of cracking must be predefined.

More recently, Danzi et al. [47] presented a study on the effect of fibre–matrix interphase defects on the mechanical properties of a UD composite using FE analyses. The defects in the RVE of the UD composite were generated by an original damage injection technique for cohesive elements. The effect of fibre–matrix debonding was firstly analysed by means of a quasi-3D unitary cell with a single fibre, with periodic boundary conditions, for different loading cases. The results showed that the position of the interfacial decohesion affected more on the mechanical behaviour more, especially for the transverse tension case. Subsequently, they studied multi-fibre representative volume elements, which confirmed the results of a softening in the stress–strain response of the single-fibre model. Finally, the effect of a 3-D debonding propagation was investigated by analysing a single fibre model with an increased fibre-wise depth. The results showed that the defects propagated in different proportions in both circumferential and axial directions under different load conditions. The results presented in this study showed and confirmed that defects weakened the mechanical properties of composites.

2.4 Discrete element method (DEM)

The discrete element method (DEM), as one of the powerful micromechanical computational models, has been also used in studying the mechanical response in FRP composites. This section reviews and introduces the basics of the DEM model.

2.4.1. Law of motion

DEM was proposed by Cundall, P.A. [48, 49] in the context of rock mechanics and has been implemented in many fields [50-57]. In a two-dimensional DEM, as shown in Figure 2-9, particles A and B (with mass) are used to discretise the domain of material and are bonded together at the contacts. The particles are usually assumed to be rigid and circular or spherical. The particles interact with each other through contact and separate when the contact strength or fracture energy is exceeded. When the internal forces are balanced, the interaction between the particles is considered a dynamic process with equilibrium. Subjected to external loading, the motion of all particles is governed by Newton's second law. In two-dimensional DEM, the motion of a particle is governed by Newton's second law:

$$Translational\ motion \qquad F_i = m(\ddot{x}_{d\_i} - g_i) \tag{2-9}$$

$$Rotational\ motion \qquad M_3 = I\dot{\omega}_3 \tag{2-10}$$

where $i\ (=1,2)$ denotes the $x-$ and $y-$ coordinate directions, respectively, F_i is the resultant force of the particle, m is the particle mass, $\ddot{x}_{d\_i}$ is the acceleration of the particle, g_i is components of gravitational acceleration (body forces), M_3 is the out-of-balance moment in $z-$ coordinate directions, $\dot{\omega}_3$ is the angular acceleration in $z-$ coordinate directions, I is the rotational inertia of the particle.

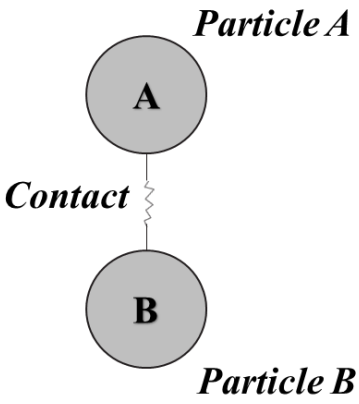

Figure 2-9: Two particles bonded at a contact.

The calculation in DEM is a cycle between the application of Newton's second law of motion on each particle and a force-displacement law for contacts between balls (see Figure 2-10). The contact forces are calculated by tracing particles within a measurement circle. The displacements of the particles are calculated by applying a constant velocity to particles and tracing their movement. From the beginning of the calculation cycle, the positions of particles are given. Then a force-displacement law is employed for every contact bond to compute contact forces. Contact forces are used in the equation of motion, and the positions of new particle can be calculated and updated by using the central finite difference method involving timestep of Δt. $\ddot{x}_{d\_i}$, $\dot{\omega}_3$, F and M_3 are calculated at the primary interval of $(t + \Delta t)$. The translational and rotational accelerations are calculated at time t:

$$\ddot{x}_{d\_i}{}^{(t)} = \frac{1}{\Delta t}\left(\dot{x}_{d\_i}{}^{\left(t+\frac{\Delta t}{2}\right)} - \dot{x}_{d\_i}{}^{\left(t-\frac{\Delta t}{2}\right)}\right) \tag{2-11}$$

and

$$\dot{\omega}_3{}^{(t)} = \frac{1}{\Delta t}\left(\omega_3{}^{\left(t+\frac{\Delta t}{2}\right)} - \omega_3{}^{\left(t+\frac{\Delta t}{2}\right)}\right) \tag{2-12}$$

The velocities at the time $\left(t + \frac{\Delta t}{2}\right)$ can be obtained as,

$$\dot{x}_{d\_i}{}^{\left(t+\frac{\Delta t}{2}\right)} = \dot{x}_{d\_i}{}^{\left(t-\frac{\Delta t}{2}\right)} + \left(\frac{F^{(t)}}{m}\, g_i\right) \Delta t \tag{2-13}$$

$$\omega_3{}^{\left(t+\frac{\Delta t}{2}\right)} = \omega_3{}^{\left(t+\frac{\Delta t}{2}\right)} + \left(\frac{M_3{}^{(t)}}{I}\right) \Delta t \tag{2-14}$$

Finally, the positions of the particles can be obtained by the integration of velocities in (2-13) and (2-14) as

$$x_{d\_i}{}^{(t+\Delta t)} = x_{d\_i}{}^{(t)} + \dot{x}_{d\_i}{}^{\left(t+\frac{\Delta t}{2}\right)} \Delta t \tag{2-15}$$

The forces, $F_i{}^{\left(t+\frac{\Delta t}{2}\right)}$ and $M_3{}^{\left(t+\frac{\Delta t}{2}\right)}$, are calculated by the force-displacement law that will be introduced in the next sub-section.

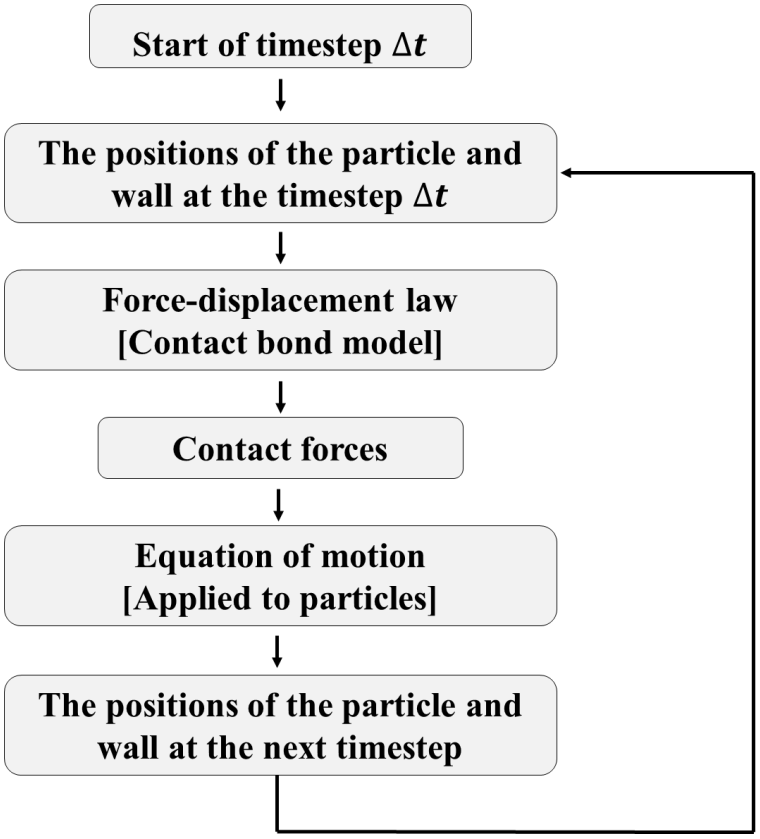

Figure 2-10: The calculation cycle of the DEM model.

2.4.2. Force-displacement law

Bonding models are used to describe the mechanical behaviour of two rigid particles at contact. The particles interact with each other through contact and separate when the contact strength or energy is exceeded. Several bonding models based on force-displacement law are available in the literature [58]. Three of them will be reviewed and discussed.

2.4.2.1. Contact-bond model

The contact-bond model can be described as a set of springs at the contact with constant normal and shear stiffness (see Figure 2-11). The resultant force of the particle is decomposed by a normal force F^n and shear force F^s as:

$$F = F^n + F^s \tag{2-16}$$

These forces are obtained from the product of normal/shear stiffness, the overlap of particles and incremental tangential displacement as:

$$F^n = k^n U^n \, n_i \tag{2-17}$$

$$\Delta F^s = -k^s \Delta U^s \tag{2-18}$$

The resultant contact stiffness k is calculated by:

$$k^n = \frac{k_n^{(A)} k_n^{(B)}}{k_n^{(A)} + k_n^{(B)}} \tag{2-19}$$

$$k^s = \frac{k_s^{(A)} k_s^{(B)}}{k_s^{(A)} + k_s^{(B)}} \tag{2-20}$$

where $k_n^{(A)}$, $k_n^{(B)}$, $k_s^{(A)}$ and $k_s^{(B)}$ are the normal and shear stiffness of the contacted particles.

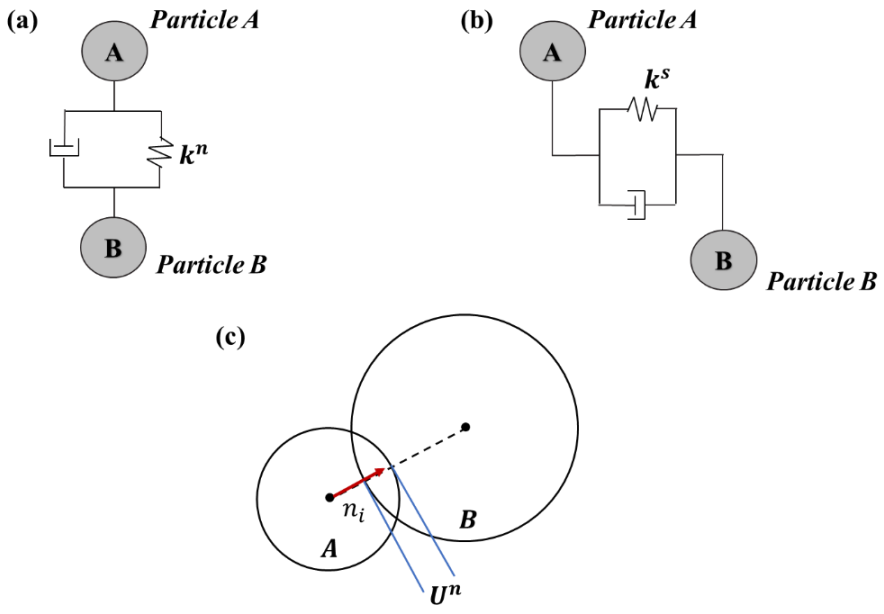

Figure 2-11: A Contact bond between two particles with (a) normal stiffness, (b)shear stiffness. (c)Diagram of a contact bond.

2.4.2.2. Parallel-bond model

A parallel-bond of two contacted particles can be regarded as a set of springs with constant normal and shear stiffness uniformly distributed over a circular or rectangular cross-section lying on the contact plane and centred at the contact point (see Figure 2-12(a)). Both forces and moments can be transmitted by the parallel-bond. The resultant force of the particle $\bar{F}$ is decomposed by normal force $\bar{F}^n$ and shear force $\bar{F}^s$ (seen Figure 2-12(b)) multiplied by normal unit vector n_i and shear unit vector n_j, respectively, as:

$$\bar{F} = \bar{F}^n n_i + \bar{F}^s n_j \tag{2-21}$$

The out-of-balance moment of the parallel-bond $\bar{M}$ is decomposed by normal moment $\bar{M}^n$ (in 2D DEM model, $\bar{M}^n = 0$) and shear moment $\bar{M}^s$ as:

$$\bar{M} = \bar{M}^n + \bar{M}^s \tag{2-22}$$

After a timestep, the increments of elastic force elastic moment are obtained by:

$$\Delta\bar{F}^n = (-\bar{k}^n A \Delta\bar{U}^n)\, n_i \tag{2-23}$$

$$\Delta\bar{M}^s = -\bar{k}^n I \Delta\theta^s \tag{2-24}$$

The area of the cross-section A and the moment of inertia of the disc I are given by:

$$A = 2\bar{R}t \tag{2-25}$$

$$I = \frac{2}{3} t\bar{R}^2 \tag{2-26}$$

where $\bar{R}$ is the radius of the bond as the minimum radius between these two contacted balls:

$$\bar{R} = min\,(R^{(A)}, R^{(B)}) \tag{2-27}$$

As the parallel bond acts in parallel with the contact bond, the overall stiffness K is resolved into contact bond and parallel bond as:

$$K = (k^{n/s})_{contant\ bond} + (A\bar{k}^{n/s})_{parallel\ bond} \tag{2-28}$$

The maximum tensile stress $\bar{\sigma}$ and the maximum shear stress $\bar{\tau}$ on the cross-section of the bond are calculated by:

$$\bar{\sigma} = \frac{-\bar{F}^n}{A} + \frac{|\bar{M}_3|}{I} R \tag{2-29}$$

$$\bar{\tau} = \frac{|\bar{F}^s|}{A} \tag{2-30}$$

Parallel-bond breaks if $\bar{\sigma} > \bar{\sigma}_c$ or $\bar{\tau} > \bar{\tau}_c$ (see Figure 2-13), then a crack occurs.

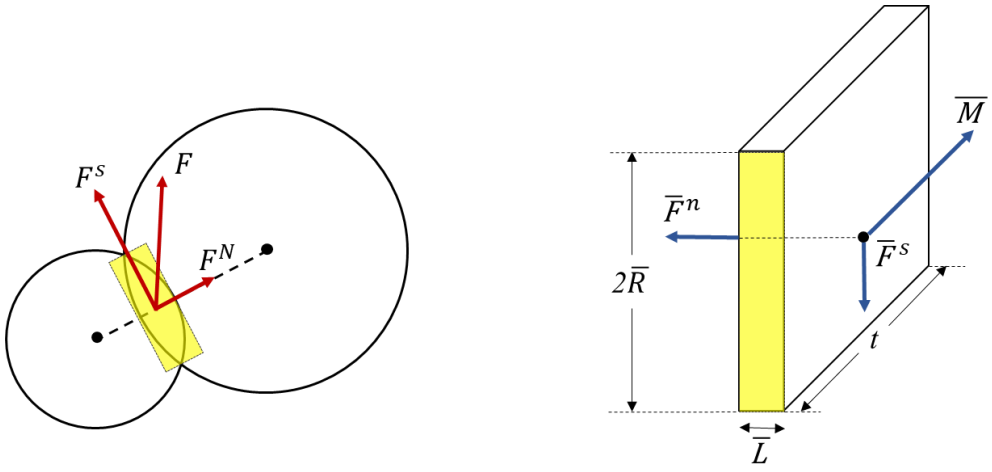

Figure 2-12: Diagram of a parallel bond.

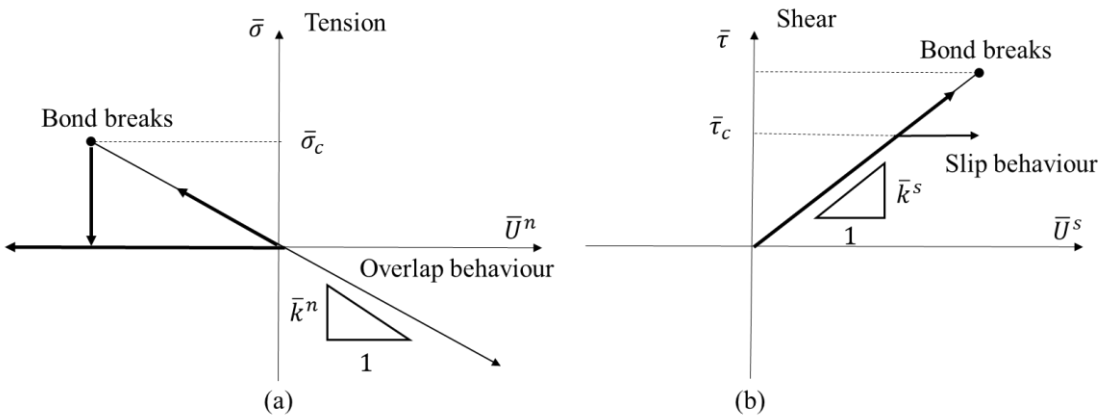

Figure 2-13: Force-displacement laws of the parallel-bond model. (a) Normal behaviour. (b) Shear behaviour.

2.4.2.3. Soft-bond model

The soft-bond model is similar to the displacement-soften model commonly used as a bonding model in the DEM model previously [58]. The model is the same as that of a linear parallel bond model before the force in the contact reaches the peak contact strength. However, the bond is not removed upon failure. The bond will enter a softening regime after the peak contact strength, and the force in the contact will then

reduce as a pre-defined function of the displacement [59]. Two factors determine the softening behaviour: the softening factor and the softening tensile strength factor, respectively.

When the softening factor is zero, the behaviour of the bond in the soft-bond model is the same as that of the linear parallel bond. When the softening factor is one, tensile softening starts with the same absolute slope but with the opposite sign of the slope as an extension up to the peak bond tensile strength. It means that the tensile stress of the bond increases at a rate until the peak stress and decreases at the same rate.

On the other hand, the softening tensile strength factor determines the point for controlling the ending of the tensile softening process. When it is one, the behaviour of tensile softening is inhabited. Therefore, tensile softening can occur if the softening factor is not zero and the softening tensile strength factor is not one at the same time. For controlling the ending of the tensile softening, once the tensile stress of the bond is larger than the peak contact strength, softening continues until the tensile stress is less than the product of the softening tensile strength factor and the peak contact strength. For instance, if the softening tensile strength factor is set to zero, the tensile softening will end when the tensile stress reaches zero.

2.4.3. Mechanical timestep and the uniaxial loading method

The timestep used in the DEM model should be defined carefully for solving the equations of motion. The timestep needs to be within a reasonable range so the calculation can be carried out smoothly at a satisfactory computational cost. The default value of the timestep can be automatically calculated by the DEM software ‘PFC’ at the beginning of each cycle. This default value of the timestep is considered a reference to the actual value of the timestep.

Consider a single one-dimensional mass-spring system (see Figure 2-14) with the mass, m, and the stiffness, k. It was found that the critical timestep is obtained by [60]:

$$t_{critical} = \frac{T}{\pi} \tag{2-31}$$

$$T = 2\pi \sqrt{m/k} \tag{2-32}$$

where T is the period of simple harmonic vibration.

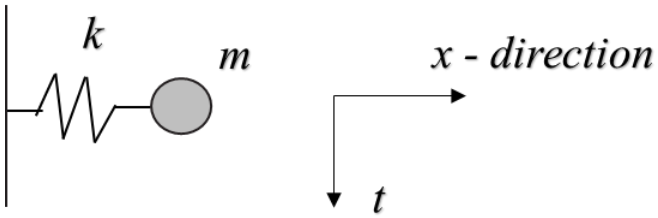

Figure 2-14: A single mass-spring system.

Consider an infinite set of point masses and springs (see Figure 2-15) with particles and contacts. The motion of a single point mass can be described by a system in Figure 2-15(b)-(c). The critical timestep for this system is estimated by:

$$t_{critical} = 2\sqrt{m/4k} = \sqrt{m/k} \tag{2-33}$$

In practice, multiplying the critical time increment by a safety factor is usually recommended [58].

Additionally, in the DEM model, uniaxial loading of tension is always implemented by applying a velocity or force on the boundary where the force acts.

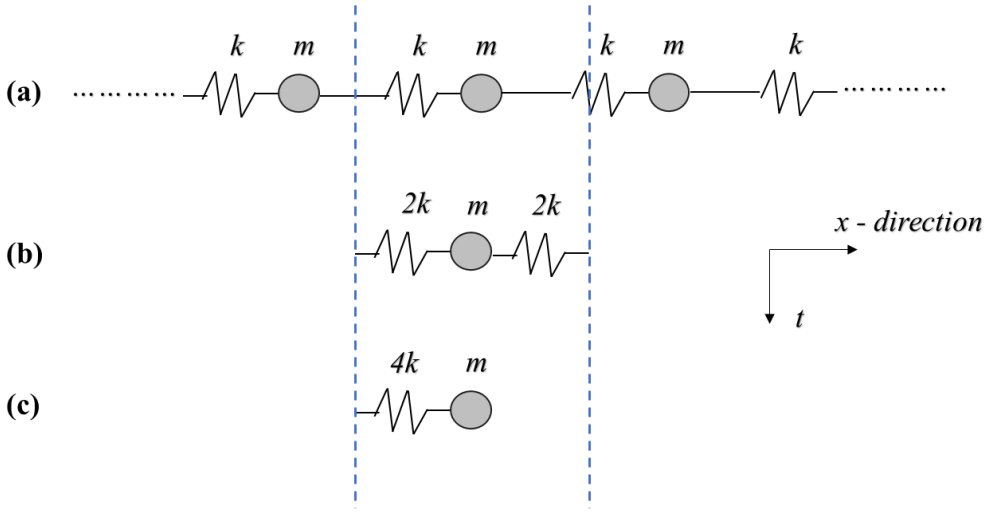

Figure 2-15: A multiple mass-spring system.

2.4.4. The applications of DEM in FRP composites

DEM has been applied to study the material failure process in the past few years. Yang et al. [61] used DEM to simulate the failure process in the micro bond test of FRP composites. In the development of DEM, the displacement-softening model was used to describe the plastic deformation and cracking of the matrix. The DEM simulation of the initiation and propagation of interfacial debonding has been compared and validated by existing experimental observations, which showed that the developed DEM model has great advantages in investigating the material and structural damages of advanced composites.

DEM model for studying transverse cracking in composite laminae with three different types of fibre distributions was then done by Sheng et al. [62]. It was shown that the DEM model can simulate transverse cracking in the forms of matrix plastic deformation and fibre/matrix interface yielding. In addition, the effect of fibre volume fraction was also investigated, and it was found that both the transverse cracking path

and the mechanical behaviours of the composite laminae were affected by fibre volume fractions.

Yang et al. [63] applied the DEM to model progressive delamination of anisotropic fibre-reinforced composite laminates. In this study, the composite laminae were discretised using a hexagonal arrangement of particles where contact bonds between two particles were governed by parallel, and a contact softening model described the residual interfacial behaviour. It was concluded that the proposed DEM model can simulate the composite delamination with the capability of capturing crack extension and plastic zone.

Based on this study, Yang et al. [64] extended the analysis to the dynamic initiation and propagation of transverse cracking and interfacial delamination in cross-ply laminates under uniaxial loading. In the construction of DEM modelling, the 90° and 0° plies were considered isotropic and orthotropic materials, and their mechanical behaviours followed the parallel bond model. The interface between the 90° and 0° plies was represented by the contact softening model. The DEM simulation results of the transverse cracking and interfacial delamination in both $[0°_1/90°_n]_s$ and $[90°_n/0°_1]_s$ cross-ply laminates under transverse loading were analysed by comparing with results of the crack density computed by the experimental data and other numerical predications. It was shown that the DEM model has considerable advantages in modelling damage progression in laminates at the microscopic level as well as predicting crack density and stiffness reduction at the macroscopic level.

In addition, Maheo et al. [65] conducted a 3D modelling of the Discrete elements method (DEM) for a UD composite cell which was restricted to a cubic Representative Elementary Volume (REV) containing one carbon fibre in an epoxy matrix. The simulations of different loadings were performed on the REV using the proposed DEM

model. The results showed that the DEM has powerful abilities in modelling the kinetics of the damage. The study of the damage mechanisms in the REV with several fibres would be expected.

2.5 Applications of machine learning in composites

With the rapid development of high-performance computational modelling, many essential mechanical properties and behaviours of composites can be computed and simulated, which can be implemented on a PC, workstation, etc. It is generally noticed that performing computational simulations for studying the mechanical response of composites is much more convenient and has less labour expense than conducting experimental tests. However, computational modelling is always governed by physical laws consisting of different equations. Consequently, it is a computational burden for computers to solve complex equations, encouraging researchers to find alternative methods. With the latest development in data science combined with powerful machine learning (ML) approaches, machine learning (ML) provides an efficient way to solve problems and make predictions.

2.5.1. The framework of the machine learning application

The concept of machine learning (ML) was first inspired by a brain-cell interaction model created by Donald Hebb [66]. The first notion of ML was defined by Arthur Samuael in 1959 as a field for computers to learn without being explicitly programmed. ML has attracted researchers to use it in different areas, such as data analytics, predictive analysis, self-driving, image recognition, etc. [67-74]. The success applications of ML encouraged researchers to explore its powerful ability in wider fields, for example, in

designing new composite materials with better properties [75]. Moreover, the combination of computational simulations and experimental tests can provide sufficient data used in the ML algorithm.

There are two basic approaches to machine learning: supervised learning and unsupervised learning. Supervised learning enables one to learn a mapping between inputs and a known output and then to predict outputs for unseen inputs [76, 77]. In contrast, unsupervised learning discovers hidden patterns in data without the information about the output, which uses machine learning algorithms to analyse and cluster unlabelled data sets [78, 79]. Supervised learning is employed more in the applications of ML in composite materials. The basic framework of the ML applied in composites is presented in Figure 2-16.

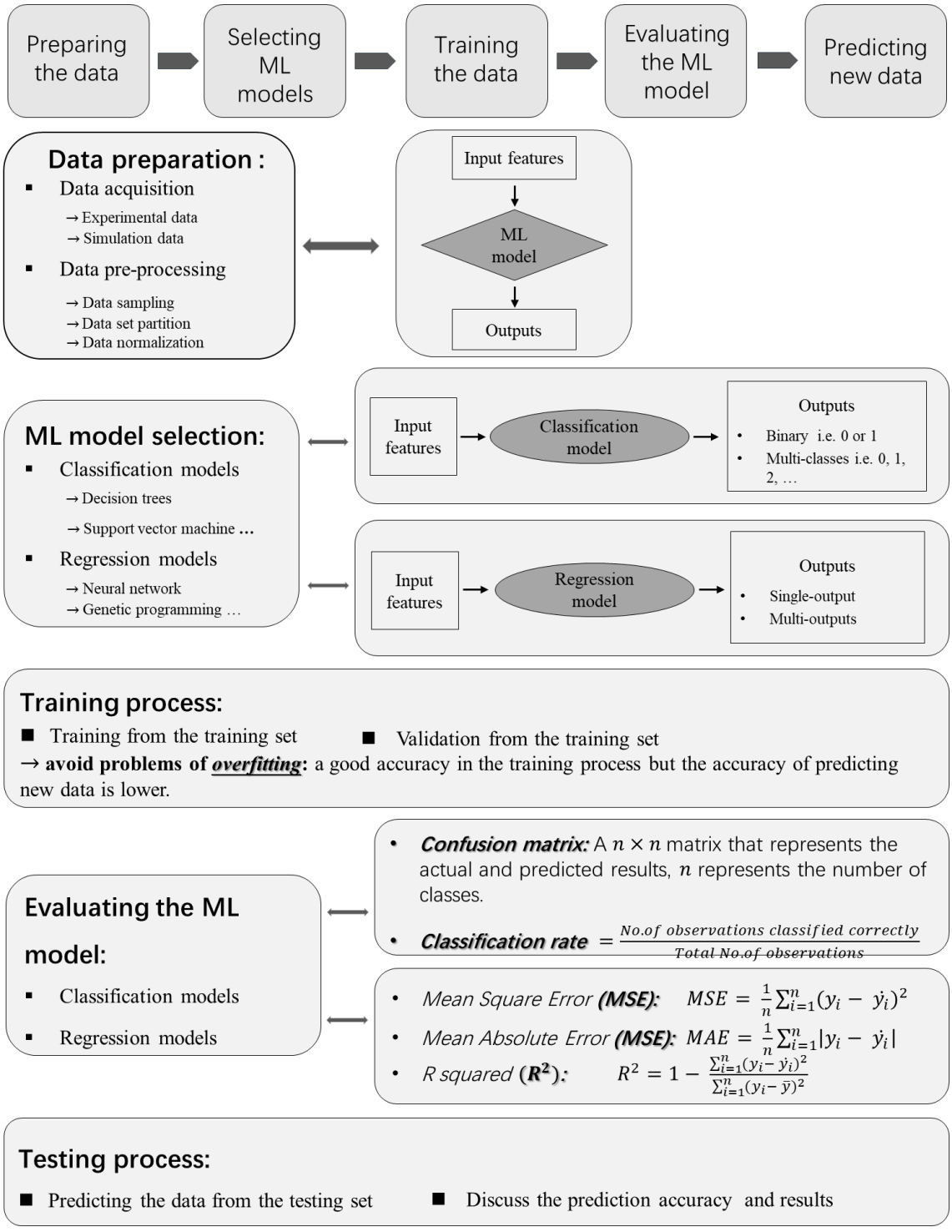

Figure 2-16: The framework of the machine learning application.

2.5.1.1. Data preparation

The first step in ML prediction is data preparation, which is the most critical step. The successful construction of the ML model is highly dependent on the experiment of design (DoE) employed for the data generation. Generally, the data can be from two resources: experimental tests and computational simulations. For the efficiency and accuracy of the ML model, generating optimal sample points that can greatly represent the entire analysis domain is necessarily required. There are several sampling algorithms available, including Latin Hypercube Sampling (LHS) [80, 81], central composite design (CCD) [82], uniform design [83], D-optimal design [84] and orthogonal array sampling [85].

It was found the performance of the ML model based on the data obtained by Latin Hypercube Sampling (LHS) was very good [86]. Gu et al. [87] employed Latin Hypercube Sampling (LHS) for selecting sample data from FEM simulations that were used as the training and testing data for the ML. The study on the application of central composite design (CCD) includes the optimization of machining parameters in drilling hybrid metal matrix composites [88], and experimental and statistical analysis of mechanical properties of nano fly ash impregnated GFRP composites [89]. However, this sampling method was found lacking in dealing with high-dimensional data [90]. In addition, Basavarajappa [91] et al. used orthogonal array sampling to generate the right experimental design and then conducted an analysis of variance to investigate the effect of various process parameters on the wear behaviour of polymer composites. Zhang et al. [92] chose a uniform design method to study the Polypropylene (PP)/waste ground rubber tire powder (WGRT) composites of various concentrations to optimize a recipe for commercial applications having high mechanical properties. Rajmohan and Palanikumar [93] constructed a response surface methodology-based experimental plan

of a four-factor (three numerical plus one categorical) D-optimal design. These studies showed that experimental design played an important role in the parametric study or the data generation for the ML model, which results in a better prediction performance with less computational cost [94-97].

After choosing or generating data, the input features need to be determined [98]. The input features should be representative and related to the outputs to some content because these features are important for the ML model to discover the inter-relation and then predict for the unseen data effectively.

2.5.1.2. Data pre-processing

Data pre-processing, including data sampling, data set partition and data normalization, is needed before training the ML model. Data sampling is required in the case of the distribution of uneven data [99-101]. Undersampling is used to delete some data points if these data is duplicated or overwhelmed. Oversampling is used to add some data if the representative data in the data set accounts for a relatively small proportion.

Then all the data is divided into two sets, i.e., training sets and testing sets. It is usually used 75% or 80% of the data in the data set is the training data. Consequently, the rest 25% or 20% of the data is the testing data. Lastly, data normalization is commonly needed when the features have different ranges. As the magnitudes of the input features and the output are at different scales, applying a data normalization method is crucial to converting the magnitudes of data to the same scale. Two common methods, namely min-max normalization and Z-score normalization, bring different features into the same scale [102]. Between them, Min-max normalization rescales the range of features to [0, 1] by the formula below:

$$x'_{i\_min\_max} = \frac{x_i - x_{min}}{x_{max} - x_{min}} \quad (2\text{-}34)$$

where x_i $(i = 1,2, \dots, n)$ is the original value of a specific feature in the training set, x'_i is the normalized value, x_{min} and x_{max} are the minimum and maximum values of a feature in the training set, respectively.

Z-score normalization rescales the data to the normally distributed data with a mean of 0 and a standard deviation of 1 by the formula below:

$$x'_{i\_z\_score} = \frac{x_i - \mu}{\sigma} \quad (2\text{-}35)$$

where μ and σ are the values of the mean and the standard deviation of a specific feature in the training set, respectively.

2.5.1.3. Selecting ML models

Based on the prediction and the generated data, the types of prediction can be confirmed. There are two types of supervised ML, namely, classification and regression. For a classification problem, ML algorithms include naïve Bayes, support vector machines, decision trees and neural networks [103, 104]. Depending on the number of classes to be classified, there are two types of classifications. One is the binary classification, which means that two classes are considered. Their corresponding outputs are one or zero. The other one is the multi-classes classification, and the outputs are zero, one, …, etc. For a regression problem, ML algorithms include linear regression, genetic programming and neural networks [105]. The categories of regression problems also depend on the target outputs. If only one target output exists, the ML problem will be regarded as a single-output regression. The ML problem is a multi-output regression once the number of the target outputs is larger than two. According to the actual prediction problem, an algorithm needs to be chosen.

There are several commonly used ML regression and classification algorithms.

- ***Linear regression***

  Linear regression is a basic but extensively used ML model when the variables are continuous. The relation between the target output and the inputs is linear and formed by [106]:

  $$Y = W \times X + B \tag{2-36}$$

  Y is the target output, X is the inputs, W is the weight and B is the bias. The weight and bias are constantly changing during the training process in order to make accurate predictions. One common technique to compute the error of the linear regression is the mean squared error (MSE) introduced in the last subsection as one of the performance indicators. Linear regression has been widely used for different types of problems in engineering due to its simplicity and high interpretability. However, linear regression assumes a linear relationship between the inputs and the output, which is a limitation for more complex prediction problems. In some studies, linear regression was tried first before using other ML algorithms to investigate how complicated the relationship is.

- ***Naïve Bayesian model***

  The Naïve Bayesian model is a simple and fast classification algorithm based on Bayes' theorem and an attribute independence assumption [107, 108]. It is an ML algorithm that has usually been applied to high-dimensional data sets [109]. It can provide fast and relatively accurate solutions for classification problems with few adjustable parameters. Given a problem to

be classified, represented by a vector $\boldsymbol{x} = (x_1, x_2, \dots, x_n)$ representing n input features, for each of m possible classes C_m, the probabilities are

$$\boldsymbol{p}(C_m|x_1, x_2, \dots, x_n) = \frac{\boldsymbol{p}(C_m)\, \boldsymbol{p}(x_1, x_2, \dots, x_n|C_m)}{\boldsymbol{p}(x_1, x_2, \dots, x_n)} \quad (2\text{-}37)$$

All the features need to be continuous data [110]. The strong attribute independence assumption causes the limitation of this classifier. When the inputs are not independent, the performance of the naive Bayesian classifier is poor.

- ***Artificial neural network (ANN)***

  Artificial neural network (ANN) has a strong ability to address complex prediction problems in composite materials [111-114], especially in capturing and establishing the interaction between input and output variables by its explicit mathematical formulation, no matter how unknown and complicated the relation is. An ANN structure with more than three hidden layers is called a deep neural network (DNN) [115]. A neural network inspired by the biological nervous network has been a robust and promising deep learning approach in modelling the mechanical behaviour of materials due to its powerful nonlinear mapping ability [116].

  Figure 2-17 shows a simplified structure of a neuron network, forming a single-output predictive model. The model comprises a multi-input layer, one hidden layer and a single-output layer. The multi-inputs denoted as x_i $(i = 1, 2, \dots, n)$, consist of the input layer. The input layer and the subsequent layer are connected with the weights of inputs that are denoted as w_i $(i = 1, 2, \dots, n)$. Each layer needs an activation function f that makes

the dot product of the inputs and their corresponding weights. Several commonly used activation functions are

1. Rectified linear activation function (ReLU) and is defined as:

$$f(x) = \begin{cases} 0, & if\ x \leq 0 \\ x, & if\ x > 0 \end{cases} \tag{2-38}$$

2. Sigmoid function and is defined as:

$$f(x) = \frac{1}{1 + e^{-x}} \tag{2-39}$$

3. Hyperbolic tangent activation function (Tanh) is defined as:

$$f(x) = \frac{e^{x} - e^{-x}}{e^{x} + e^{-x}} \tag{2-40}$$

Then a set of biases is required to add to the dot product of the inputs and their corresponding weights, which finally calculates the value of the single-output y.

$$y = f\left(\sum_{i=1}^{n} x_i w_i + b\right) \tag{2-41}$$

The direction of the connection between neurons can be either unidirectional or bidirectional, resulting in two types of networks: feedforward and feedforward networks with error feedback networks, respectively. The latter is called a back-propagation neural network which simultaneously allows forward signal transmission and error back propagation. In a back-propagation neural network, the inputs propagate from the input layer to the hidden layer, then propagate to the output layer via an activation function with positive orientation, which is regarded as forward learning in the training process. The error will occur if there is a difference between the expected output value and the actual output value, which turns on the

execution of the process of error back-propagation. The error backward stage during the training process aims to ensure that the error is decreased iteration by iteration and within an acceptable or predetermined range by continuously adjusting and updating the weights of neurons in each layer.

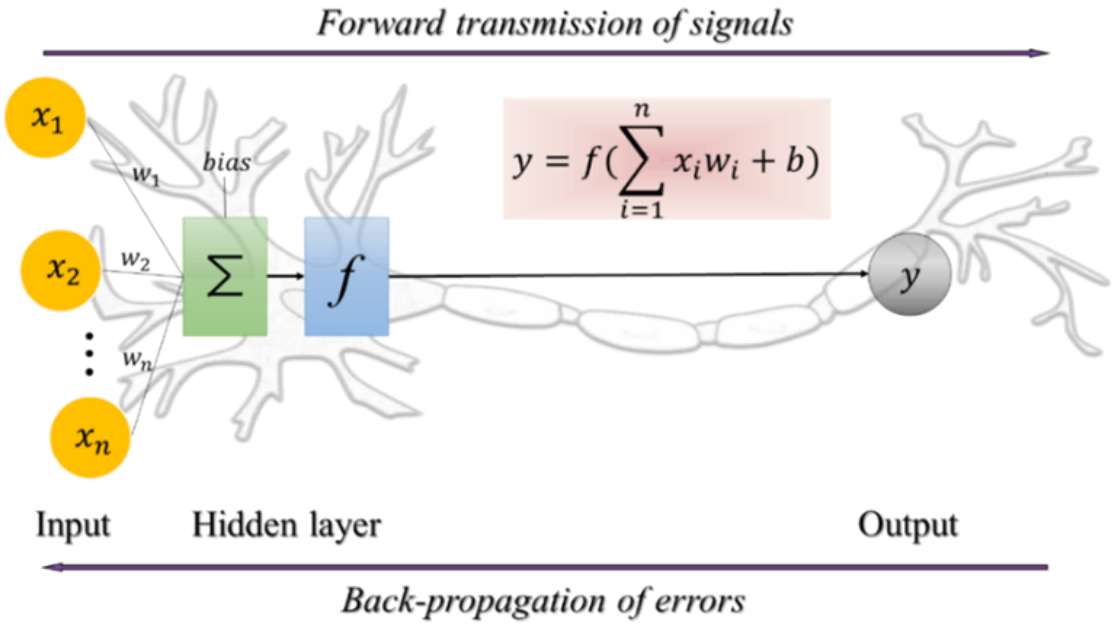

Figure 2-17: Architecture of a simplified artificial neuron network with back-propagation feedback.

2.5.1.4. Training and testing the ML model

The next step is to train the generated data using the ML model. Meanwhile, evaluating the performance of the ML model is carried out. Performance indicators are used to evaluate the model during training and testing. Some commonly-used indicators are presented in Figure 2-16 for both the classification and regression models [117, 118]. Confusion matrix and classification rate are usually used as indicators used for the classification. A confusion matrix is an $n \times n$ matrix that represents the actual and predicted results, where n represents the number of classes. Moreover, the classification

rate is the ratio of the number of observations classified correctly to the total number of observations. For the regression ML model, MSE measures the average of the squares of the errors between the given simulation results and the predicted results. MAE is a measurement of an arithmetic average of absolute errors. R^2 represents the proportion of the variance for the target output in the ML model. From the equations, it is clear that an MSE or MAE value closer to zero represents a better prediction of the ML model, while for the R^2 indicator, a value closer to one suggests a better prediction. It is highly stressed that a high accuracy evaluated by indicators with good value in the training process does not mean high accuracy in the testing process. An ML model sometimes has satisfactory accuracy during the training process but low accuracy during the testing process. This is a problem called overfitting.

To avoid the problem of overfitting, cross-validation is usually used [119-121]. Cross-validation, as a resampling method, uses different portions of the data in the data set to train and test an ML model literately. Figure 2-18 presents a 5-fold cross-validation. It can be seen that the whole data set is divided into five subsets. In each iteration, the ML model needs to train the four subsets, and one last subset will be considered as the unseen data set for validating the model's performance. Hence, a 5-fold cross-validation has five rounds of cross-validation which are then combined for analysing the prediction performance of the ML model.

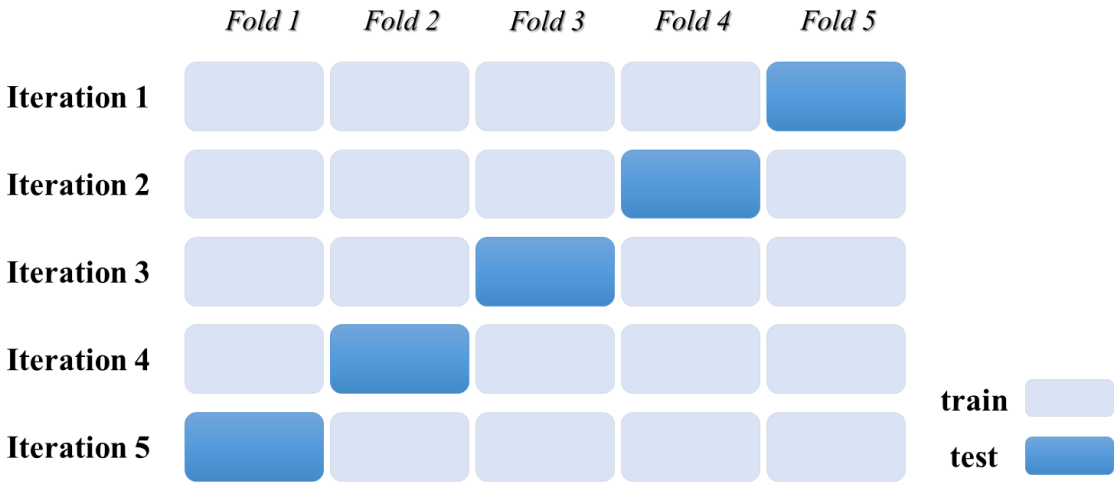

Figure 2-18: Training and test sets of a 5-fold cross-validation method.

2.5.2. Machine learning (ML) prediction for composites

2.5.2.1. ML for predicting the mechanical behaviour of composites

For the applications of ML in the investigations of mechanical behaviour, researchers began to use ML to predict the mechanical behaviours of different composite materials. Liu et al. [122] employed a deep learning neural network to generate a new failure criterion for fibre tows, which can accurately predict the initial failure of woven composites regardless of the material microstructure, mesostructure and failure mechanism. Chen et al. [123] used both artificial neural network classification and regression models to predict the strengths of particulate-reinforced metal matrix composites (PRMMCs) using the data obtained from an RVE-based direct method. Based on recognized patterns, the networks can be used to make moderately accurate predictions on the ultimate strength and highly accurate predictions on the endurance limit. However, the researchers found that more data would be used as the input data for the better performance of the predictive model.

Furthermore, other ML models were considered to compare the prediction accuracies. Gu et al. [87] constructed a deep neural network (black-box) and a genetic programming (grey-box) model for accurately predicting the ultimate failure load of single lap joints based on a large amount of parametric FE model simulations with full consideration of four continuous geometry variables and three discrete material variables. The data sets for training and testing the machine learning models were selected using the Design of Experiment (DoE) method of Latin Hypercube Sampling (LHS). The prediction results and the case study of designing an adhesive layer for a hybrid PPA-Al joint presented in the study showed that the developed DNN and GP models can be used in practice as an effective tool for analysing and designing adhesive single lap joints. Rahman et al. [124] developed a convolutional neural network model based on the data from molecular dynamics (MD) simulations of carbon nanotube (CNT)-reinforced composites. Their model can predict the interfacial shear strength of carbon nanotube (CNT)-reinforced composites, which showed the great success of ML models for both predicting interfacial properties in nanocomposites and optimising the mechanical properties of CNT-epoxy interfaces. Xu et al. [125] developed a DNN method for accurately predict the strengths of brittle specimens consisting of randomly distributed microcracks. The data was based on micromechanical method simulations of a large number of 2D microcracked brittle specimens. Liu et al. [126] developed an efficient approach to predict Young's modulus and ultimate tensile strength of Gr/Al nanocomposites by combining MD simulations and the ML modelling, which can be used to modify the existing Halpin-Tsai model to account for some more important factors for the more accurate prediction of Young's modulus for Gr/Al nanocomposites.

The studies reviewed above used the data generated by numerical micromechanical models. Databases from experimental tests and related literature were also commonly adopted. Zhou et al. [127] built an explicit neural network model to predict FRP-concrete interfacial bond strength from a large database based on an extensive survey of existing single-lap shear tests on FRP-concrete interfacial bonds. The predictive model performed well by comparing a calibration with conventional shear-bond models and a large database. Jahangir et al. [128] collected and compiled a database of experimental test results from the literature to estimate bond strength between FRP strip and substrate concrete through the artificial neural network and the hybrid artificial neural network with an artificial bee colony algorithm (ABC-ANN). More recently, Yuan et al. [129] used the data that was extracted from both the published experiments and a small amount of finite element analysis (FEA) results and proposed a kernel ridge regression (KRR) model for an axial elastic modulus degradation prediction of $[0°_m/90°_n]_s$ cross-ply laminates.

2.5.2.2. ML for predicting the mechanical properties of UD FRP

The study on determining the macroscopic mechanical properties of UD FRP laminae combined with either ML or data mining has also shown its desirability. Pathan et al. [130] combined the principal component analysis (PCA) and the Gradient Boosting Regressor (GBR) to predict the mechanical properties (macroscopic elastic moduli or yield strength) of a UD FRP composite by training the data from numerical micromechanics (FEM) simulations of computer-generated microstructures. The geometry of microstructures was obtained by using the 2-point correlation function and its principal component analysis. Fast and accurate predictions can be made once the ML model is trained. However, no comparison was conducted between the ML

approach's prediction results and the existing micromechanics analytical models. The researchers expect that data-driven ML approaches can be devised in the case of fibre-dominated failure modes.

Yao et al. [131] used the material properties of each constituent in UD FRP laminae, collected from a literature database to predict UD FRP properties using data mining. However, the ability of data mining by applying statistical tools in establishing the structure-properties relations was not as strong as an ML model can offer since the capability of data mining may be limited by the incompleteness of data and complex failure mechanisms of composites.

Those proposed ML predictive models reviewed above transfer a mechanical problem of damage into a non-linear regression problem in ML by finding the relationship between the input and output data, which shows great potential for solving some more complex mechanical problems of composites.

2.5.2.3. ML for predicting the fracture of composites

The study on the application of ML in predicting the fracture process of composite materials is still at its very early stage and hardly found in the literature. ML approaches have been used to predict the fracture process of brittle materials.

Moore et al. [132] used several ML algorithms to predict the location and timing of fracture coalescence in a 2D concrete sample under pure tensile loading conditions by using simulation data from the combined Finite-Discrete Element Method (FDEM). The simulation was often computationally prohibitive due to the difference in length scales between small fractures and bulk material sizes. The data for the ML prediction was obtained from 200 two-dimensional simulations of a rectangle structure of 2 metres by 3 metres. Figure 2-19(a) shows that 20 pre-set initial fractures of uniform length

(30cm) was randomly distributed in each rectangle structure. The target output was if the two fractures can coalesce, which resulted in a binary ML classification problem. Several input features were selected based on the geometry of the pre-set fractures, like the lengths of the two fractures, their orientations, …, etc. The output will be one is the two fractures coalescence. Otherwise, the output will be zero. If coalescences between every two pre-set fractures occur, the failure path of the material can be obtained. The prediction results from ANN, RF and DT were discussed. It showed that RFs and DTs can learn key patterns and trends in the training data set well and make accurate predictions in a very short time (5 orders of magnitude drop-in computational time) compared to the computational simulation.

Based on this study, Hunter et al. [133] presented a study that combined the ML and graph-theoretic approaches for predicting fracture evolution in concrete to prove the prediction performance. The ML models were used to learn the dominant trends and effects that can determine an overall material response. Two metrics were also chosen for comparison: the failure pathway and the failure time. The data from 150 simulations were trained into the ML algorithms. An additional 35 simulations were used for the validation of the methods. The performance of the predictive models was good. However, the current algorithm only considered pairwise interactions, neglecting the effects of 3 and higher-order crack interactions.

Schwarzer et al. [134] continued to study the fracture evolution in concrete using recurrent graph convolutional neural networks, and the prediction can be made more rapidly and accurately. The newest study from the research team adopted a new form of data augmentation to compensate for the relatively modest size of the training data set. The training of the predictive model was based not only on simulation results but also on incorrect predictions that were produced from the earlier training. In this way,

the network learnt to correct the mistakes itself. The significant advantage of a deep learning approach was the computational speed. The neural network generates resulted in seconds once trained instead of running a several-hour simulation. The predictions for the fracture size were using 5-fold cross-validation, which showed good agreement with the results of simulations. It was found that the deep learning model can generate predictions simultaneously for qualitatively distinct material properties, i.e., the time to material failure, efficiently and accurately.

Hsu et al. [135] adopt a convolutional Long-Short-Time-Memory (ConvLSTM)-based model to investigate dynamic crack propagation in brittle materials. The data for training and testing the ML model was achieved from the Molecular Dynamics (MD) simulations of fracture patterns in crystalline solids based on the data from molecular simulations. An initial crack with its length was pre-set in the microstructure of the material (see Figure 2-19(b)). Instead of running the time-consuming MD simulation, the goal was to use ML to predict the overall crack propagation pathways. The proposed ML model accurately predicted crack patterns and can provide a general framework for other fracture scenarios. It was stressed that the performance of the model can be improved by adding more data from MD simulation results with complicated geometric conditions.

In addition, Elapolu et al. [136] developed a machine learning model based on the convolutional neural network and bidirectional recurrent neural network to predict the fracture evolution in pre-cracked polycrystalline graphene under tensile loading (see Figure 2-19(c)). The data was based on Molecular Dynamics (MD) simulations and pre-processed images. The predicted crack growth by the networks showed a close agreement with the MD simulations. The proposed machine learning model predicted

crack paths in polycrystalline graphene sheets accurately and instantaneously, which can avoid the computational costs caused by the micromechanical simulations.

Among those studies of ML applications in fracture predictions, it was assumed that there were one or several pre-set initial cracks in the brittle material and that the material was homogenous (see Figure 2-19). These assumptions have significantly improved the accuracy of the machine learning predictions, as pre-embedded cracks conveniently avoided the difficulties in predicting initial cracking. Moreover, the assumption of homogeneity avoided considering the microstructures of individual constituents, such as the randomly distributed fibres in an FRP lamina. An accurate and more realistic prediction of crack initiation, propagation and failure of anisotropic medium using an ML approach remains a challenge that demands urgent attention.

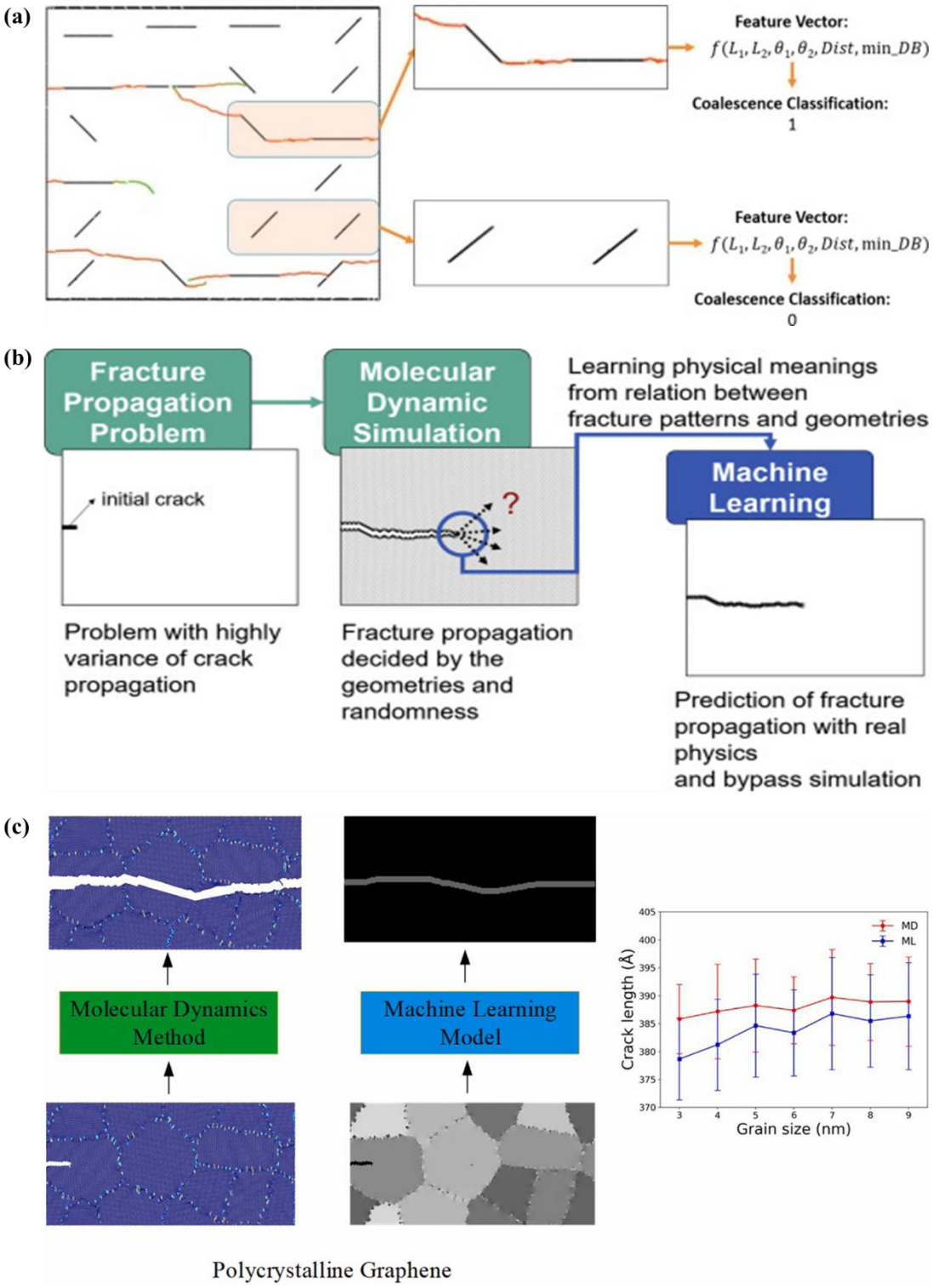

Figure 2-19: (a)Predictive modelling of dynamic fracture growth in brittle materials with machine learning [132]. (b)Using Deep Learning to Predict Fracture Patterns in Crystalline Solids [135]. (c) Studying crack propagation in polycrystalline graphene using machine learning algorithms [136].

Sepasdar et al. [137] recently presented an image-based deep learning framework to predict the nonlinear stress distribution and failure pattern in composite materials. The Mises stress contours at the early stage of damage initiation (ESoDI) and its failure pattern in 4500 microstructural representations of carbon fibre-reinforced polymer (CFRP) composites were simulated by the FE model. As shown in Figure 2-20, the deep learning framework consists of two fully-convolutional networks, Generator 1 and Generator 2, which were trained sequentially. Generator 1 used microstructural geometry as the input. Its target was the von Mises stress contours at ESoDI. Then Generator 2 used the output of Generator 1 as the input to predict the crack pattern. The criterion of the true accuracy of the deep learning approach was based on visually inspecting the predicted and target (FE simulated) crack patterns for the samples of the validation data set. The prediction results were separated into three categories, which were "good" (G), "partly good" (PG), and "bad" (B) predictions (see Figure 2-21). According to this criterion, it was shown that the proposed deep learning approach can predict the post-failure full-field stress distribution and its failure pattern with a high accuracy of 90%. It could achieve higher accuracy if more features are involved.

All these studies show that ML offers a broader scope for accurately and efficiently investigating the mechanical behaviour of composites based on the data from limited experimental tests or computationally intensive micromechanical models.

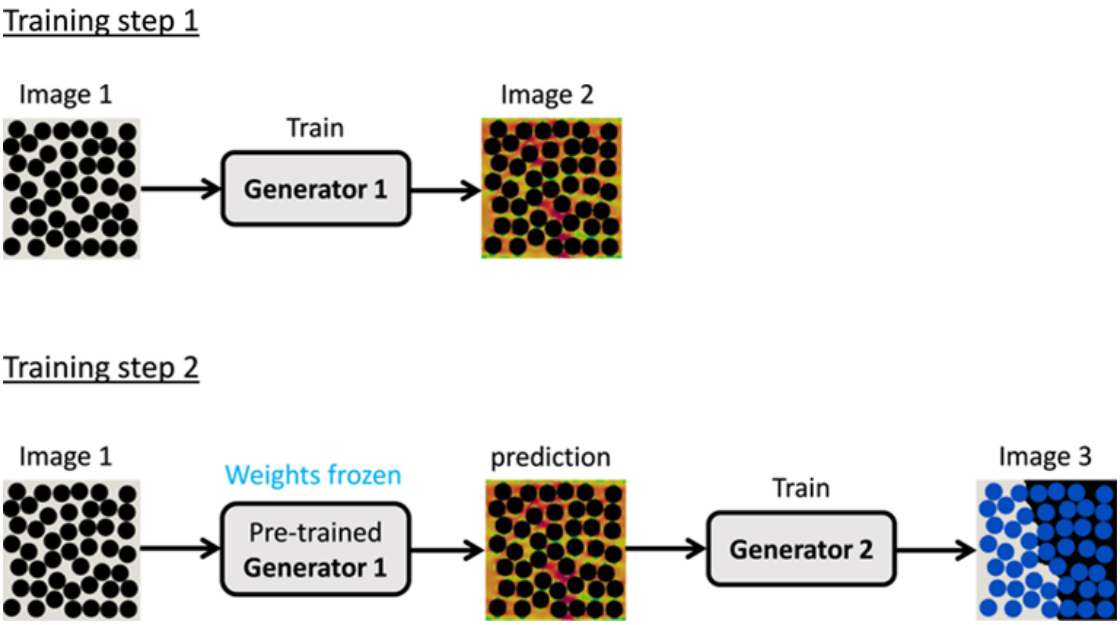

Figure 2-20: The sequential training approach utilized in the proposed deep learning framework for training Generator 1 and Generator 2 [137].

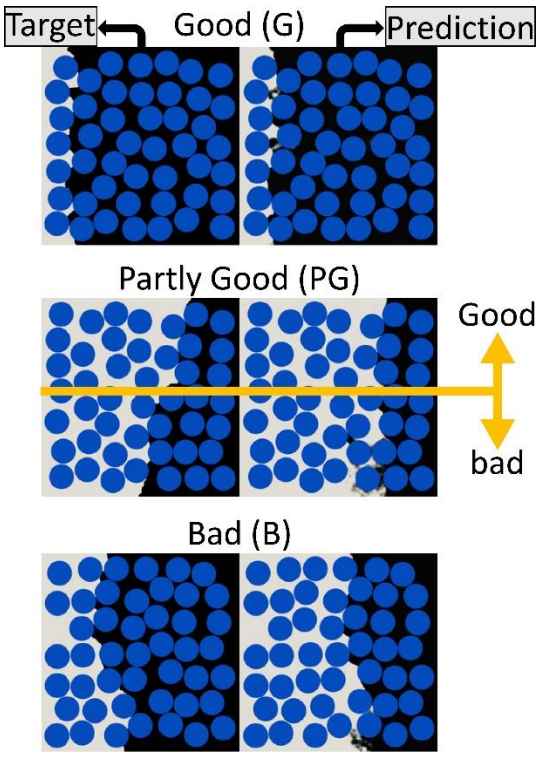

Figure 2-21: Illustration of good (G), partly good (PG), and bad (B) crack pattern predictions by the deep learning framework [137].

2.6 Summary

In this chapter, a brief introduction to composite materials, especially laminated FRP composites, is presented first. The study of the transverse mechanical properties (stiffness and strength) begins with micromechanical analytical models. However, the prediction obtained using these micromechanical analytical models is not very accurate as the analytical models have some assumptions and constraints. It accelerates the development of computational micromechanical models. The computational micromechanical analysis is usually obtained through a representative volume element (RVE). Then a number of studies using the finite element method (FEM) are presented on predicting the mechanical behaviours of the RVE of UD composites. The simulation results show satisfied agreement with those from the experimental tests, which can be used as an efficient computational tool for understanding the material characteristics. In addition to the FEM, the discrete element method (DEM) shows its extremely powerful ability to simulate the mechanical behaviour in composites, especially in tracking the crack initiation and propagation in the lamina and the delamination in laminates. However, computational modelling is always complicated as it is usually governed by physical laws consisting of different Machine learning (ML), which provides an efficient way to solve problems caused by computational difficulties and experimental complexity. The ML applications in the predictions for the mechanical properties and fractures in composites are reviewed. Some shortcomings in the studies stated in this chapter will be discussed and solved in the thesis.

Chapter 3

3 Studying the mechanical behaviour of unidirectional fibre-reinforced polymers: DEM simulation and deep learning prediction

To investigate the mechanical behaviour of a UD FRP composite lamina subjected to transverse loading, a two-dimensional (2D) plane strain computational micromechanics discrete element method (DEM) model is used to analyse a Representative volume element (RVE). Crack initiation and propagation in the RVEs containing randomly distributed fibres with different fibre volume fractions are simulated using the DEM model. A deep learning model is developed to predict macroscopic transverse properties of UD FRP composite laminae based on the data generated from the microscale RVE-based DEM model simulations.

3.1 2D RVE-based DEM model

3.1.1. RVE generation

In a UD FRP composite, the reinforcing fibres are aligned in their longitudinal direction and are normally randomly distributed in the matrix over the transverse cross-section. To study the transverse mechanical response in the UD FRP composite laminae, RVEs of the cross-section of UD FRP composite laminae with suitable size are needed. The dimension of the RVEs is set as $50\mu m \times 50\mu m$, and the diameter of the fibre is $3.3\mu m$. The fibre volume fractions of the RVEs are chosen to be 45%, 50% and 60%. It has been validated that the square RVEs based on the fibre volume fractions and

diameter are reliable in representing the macroscopic properties of UD composite laminae [28]. As shown in Figure 3-1(a), an RVE of the lamina with 50% fibre volume fraction, which contains 43 circular fibres of radius $R = 3.3\mu m$ randomly distributed in the matrix is generated. The material properties of fibre, matrix and fibre-matrix interface for the FRP composite lamina are shown in Table 3-1, which is the FRP composite lamina used throughout the thesis. There are several different numerical algorithms for generating randomly distributed fibres in the RVE of the cross-section of UD FRP composite laminae. Among them, the approach proposed in [23], which is based on the discrete element method (DEM) and experimental data of fibre diameter distribution, is employed to construct the RVE and achieve randomness and the required fibre volume ratio. The RVE is subjected to the periodic boundary condition, and the process of the RVE generation is implemented by the DEM software 'PFC2D' [58]. In order to ensure the fibre volume fraction of the RVE, one fibre will be added along the opposite boundary of the RVE when one fibre is about to be out of the boundary, shown in Figure 3-1(b) as the paired fibres. In the generated RVE of the lamina, fibres and matrix are coloured yellow and blue, respectively. They are all discretised with particles by the hexagonal packing arrangement, as shown in Figure 3-1(c)(d), which requires three types of bonds of contact. i.e., contact bond of two fibre particles, contact bond of two matrix particles and the contact bond between a fibre particle and a matrix particle.

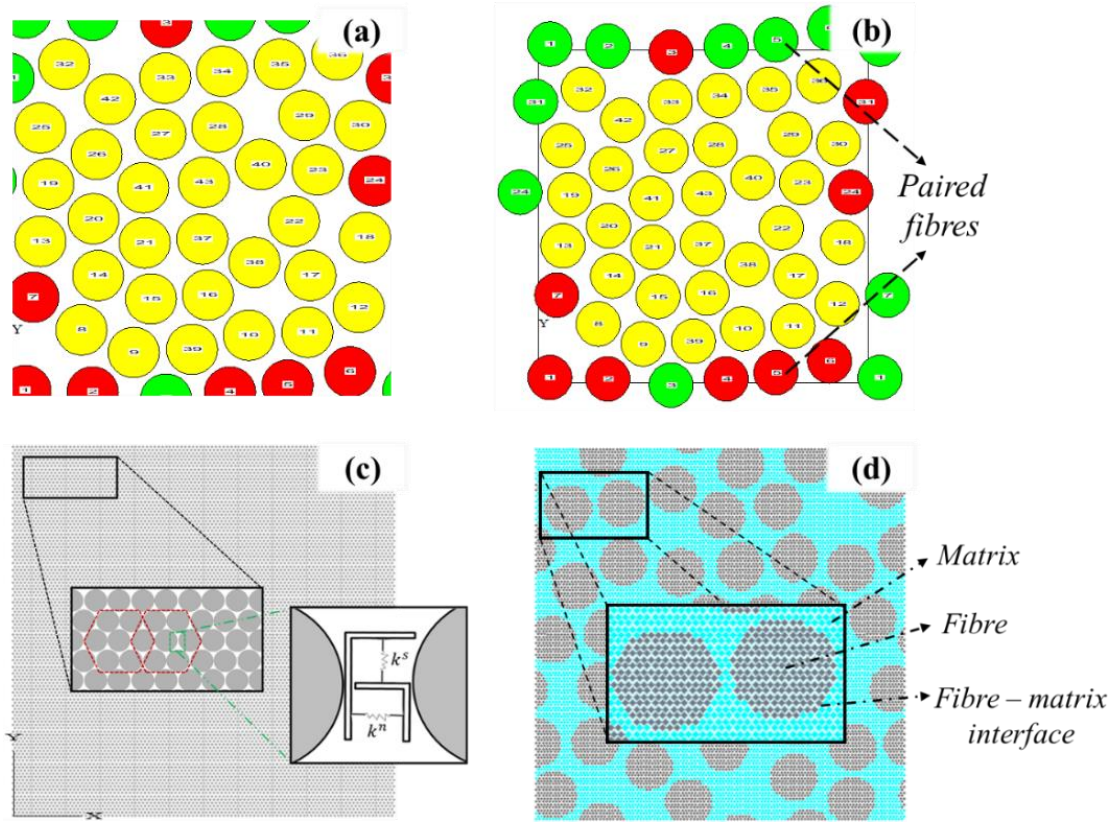

Figure 3-1: RVE of the cross-section of UD FRP composite laminae with randomly distributed fibres and discrete element discretisation. (a) Random fibre distribution in an RVE. (b) Paired fibres on the boundaries of an RVE. (c)(d) Discrete element discretisation using hexagonally packing arrangement.

Table 3-1: Material properties of fibre, matrix and interface [15].

Fibre	Transverse modulus, E_f (GPa)	40
	Poisson's ratio, v_f	0.25
Matrix	Modulus, E_m (GPa)	4
	Poisson's ratio, v_m	0.35
	Tensile strength, σ_{mt} (MPa)	60
Interface	Facture energy, G (J/m^2)	10

3.1.2. Contact models and the calibrations

In the DEM simulation, particles of fibres and matrix are bonded at contacts by parallel-bonds, and their behaviours are analysed by the parallel bond model. Particles of fibre and matrix interface are modelled by the soft-bond model. The relationships between the micro parameters (for instance, the contact stiffness and the bond strength), and the macro properties (for instance, the modulus and the strength) are established using virtual tensile tests. As the composite lamina is made of two constituents, i.e., fibre and matrix, with their own properties obtained from experimental tests, its corresponding calibration is carried out individually. The DEM model assumes that both the fibres and the matrix are isotropic. For the hexagonal packing arrangement (see Figure 3-2), the contact stiffness can be expressed explicitly as functions of the respective Young's modulus and the Poisson's ratio of fibres and matrix [138]. For a 2D homogeneous isotropic continuum, the contact stiffness ($\tilde{k}^n$: normal stiffness; $\tilde{k}^s$ shear stiffness) between particles can be calculated by the following expressions:

$$\tilde{k}_f^n = \frac{2E_{f/m}\lambda}{2\sqrt{3}(1+v_{f/m})}\left(1+\frac{2}{3(1-v_{f/m})}\right) \tag{3-1}$$

$$\tilde{k}_f^s = \frac{2|3v_{f/m}-1|E_{f/m}\lambda}{6\sqrt{3}(1-v_{f/m}^2)} \tag{3-2}$$

where $E_{f/m}$ is Young's modulus and $v_{f/m}$ is the Poisson's ratio of the fibre and matrix, respectively. Therefore, the contact stiffness used in the contact model can be determined.

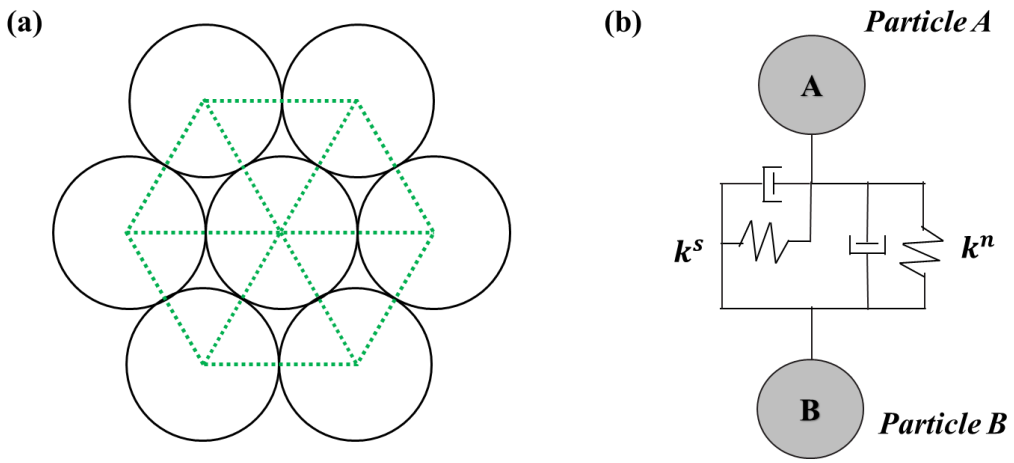

Figure 3-2: (a)Discrete elements with hexagonal packing. (b)Contact between two particles.

In addition, the relationship between the micro and macro strength parameters should be established. The micro strength is the contact bond tensile strength used in the DEM model. Calibration for the contact bond tensile strength against macro material tensile strength was done by virtual tensile tests [139]. The relationship between contact bond tensile strength (denoted σ_{micro}) and macro strength (denoted σ_{macro}) was linear for the hexagonal packing arrangement of the particles:

$$\sigma_{micro} = \beta \sigma_{macro} \tag{3-3}$$

where β is a constant factor. The tests were taken in the DEM model by testing the RVEs made of different numbers of particles to find the converged constant factor and the required minimum number of particles. It was found that the factor β = 1.7 can achieve the target macro strength when the number of particles in the RVE is more than 5530 [139]. The RVE used in this chapter is then discretised by approximately 13000 particles. And the micro-contact tensile strength of the matrix bond is therefore computed as 1.7 times the macro strength of the material, which is 105 MPa. In this study, it is assumed that there is no fibre damage under transverse tension. Thus, the micro-contact tensile strength of the fibre bond is set as a very large value. The interface

strength used in the soft-bond model is taken as the value of the cohesion yield stress calculated using the Mohr-Coulomb criterion [28, 140]. The cohesion stress and the internal friction angle is related to the tensile strength of the matrix by:

$$\sigma_{mt} = 2c\ \frac{cos\ (\alpha)}{1 + sin\ (\alpha)} \tag{3-4}$$

in which α is the angle of internal friction, c is the cohesion yield stress and σ_{mt} is the matrix tensile strength. The parameters for the Mohr-Coulomb criterion are the angle of internal friction $\alpha = 15^{\circ}$ and the matrix tensile strength $\sigma_{mt} = 60\ MPa$ (given in Table 3-1). Therefore, the corresponding cohesion is 39.1 MPa, which gives the fixed normal interface strength of 39.1 MPa. The micro strength parameters used in the contact model are set.

Last, the parameters used in the soft-bond model should be calibrated. The parameters are the softening factor and the softening tensile strength factor, respectively. The softening factor cannot be zero. Otherwise, the softening behaviour will be prohibited. Figure 3-3(a) shows the case that the tensile stress of the soft bond increases at a rate until the peak stress and decreases at the same rate in the softening process. In this case, the softening factor is one. If this factor is larger than one, the tensile stress will decrease slower in the softening process. After doing the virtual tensile tests in the DEM model, the softening factor is calibrated as 150. Figure 3-3(b) shows this case. It can be seen that the tensile stress declines very slowly after it reaches the peak stress. For controlling the ending of the tensile soften, softening ends until the tensile stress is less than the product of the softening tensile strength factor and the peak contact strength. According to this definition, the softening tensile strength factor is set to zero, and then the softening ends when tensile stress reaches zero (see Figure 3-3(a)(b)).

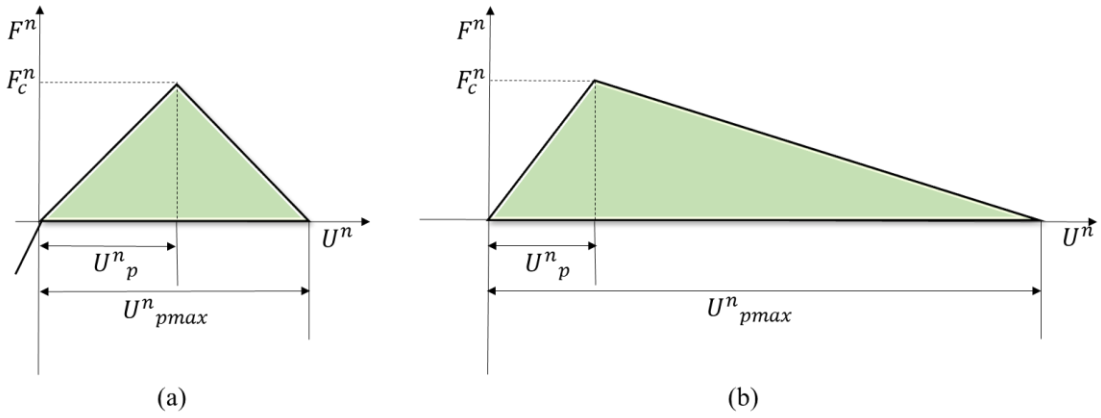

Figure 3-3: Force-displacement laws of the soft-bond model when (a) the softening factor is one, and the softening tensile strength factor is zero. (b) the softening factor is larger than one, and the softening tensile strength factor is zero.

3.2 Simulation results of the mechanical response of the laminae

3.2.1. DEM Model validation

To study the macroscopic transverse mechanical behaviour of the UD FRP composite lamina, a constant tensile velocity of 5 mm/s is applied simultaneously on the particles located at both the left and right boundaries of the RVE. This is different to the FEM analysis [15, 28, 30] in which periodic boundary conditions are used to ensure the compatibility of strain and stress at marco level. In addition, the fibres are assumed to be linearly elastic, and there is no fibre damage during loading.

For the purpose of model validation, DEM simulations are first carried out for two commonly used UD FRP laminae, i.e., AS4/3501-6 epoxy and E-glass/MY750 epoxy [141]. Using the material properties given in [141], RVEs of $50\mu m \times 50\mu m$ containing randomly distributed fibres of 60% volume fraction are constructed for the two UD FRP laminae. Due to the randomness of DEM model for generating RVEs, for each type of laminae, 8 RVEs with constant fibre volume fractions of 60.7% and 59.6% are generated and then simulated, respectively. The DEM approach for the RVE

generation can accurately achieve the fibre volume fractions of the two laminae (60%). A total of 16 DEM simulated stress-strain curves are shown in Figure 3-4, from which the transverse Young's modulus and the transverse tensile strength of the two types of laminae are evaluated by taking the respective average, as shown in Table 3-2. The experimental results from [141] are used for validation (see Table 3-2). It can be seen that the predictions based on the DEM model agree well with the experimental tests.

Table 3-2: Transverse modulus and transverse tensile strengths obtained by DEM model and experimental test for two UD FRP laminae.

	AS4/3501-6 epoxy		E-glass/MY750 epoxy	
	DEM	Experiment [141]	DEM	Experiment [141]
Fibre volume fraction	60.7%	60%	59.6%	60%
Transverse modulus (GPa)	10.1	11	15.8	16.2
Transverse tensile strength (MPa)	50	48	44	40

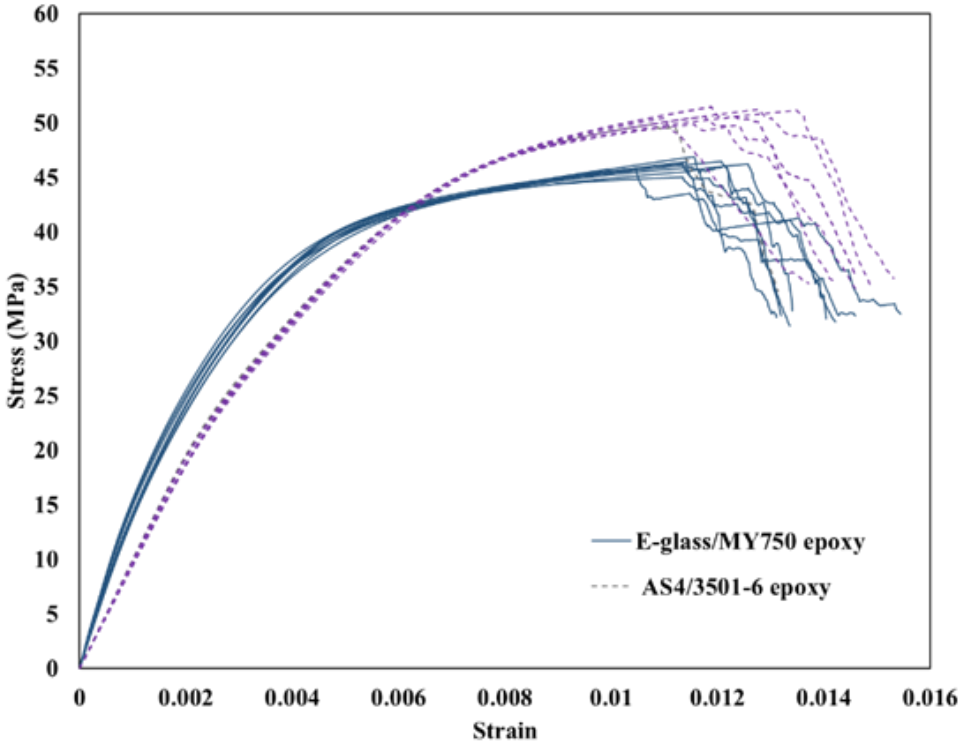

Figure 3-4: DEM simulated stress-strain curves of AS4/3501-6 epoxy lamina and E-glass/MY750 epoxy.

On the other hand, three RVEs of the UD FRP lamina with the properties in Table 3-1 are also simulated by DEM model. The dimension of the RVE is $50\mu m \times 50\mu m$ that contain about 44 randomly distributed fibres of radius R = 3.3μm. The stress-strain curves of the three RVEs are shown in Figure 3-5. It can be seen that the mean transverse tensile strength of RVEs is approximately 58 MPa, which is a bit smaller than the macro matrix strength of 60 MPa. The tensile strength of the lamina achieved by DEM simulation shows a good agreement with the result from the FEM [15]. Therefore, it can also be concluded that the DEM model can provide accurate and reliable simulation results.

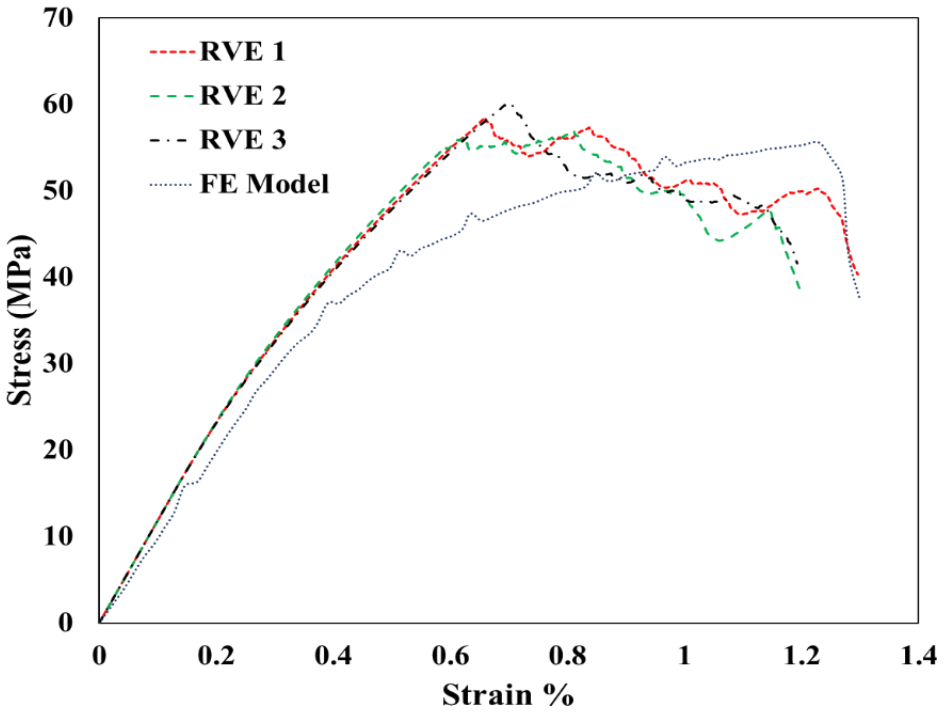

Figure 3-5: Stress-strain curves of the three RVEs compared with FEM result [15].

3.2.2. Simulated crack initiation and propagation in the RVE

The damage states at different strains can be captured in the DEM simulations. The crack initiation and propagation in the RVE of the UD FRP composite under transverse tension are presented in Figure 3-6. The RVE contains randomly distributed fibres with a 45% volume fraction. As shown in Figure 3-6(a), the cracks start at the strain of 0.558% (point A in Figure 3-6(e)) and occur in the centre right of the RVE between two relatively closed fibres. Then some more short cracks are created among some pairs of fibres with very small distances. Deformation increases as the load is applied, while the cracks propagate through the matrix, resulting in the final crack at failure (point D in Figure 3-6(e)).

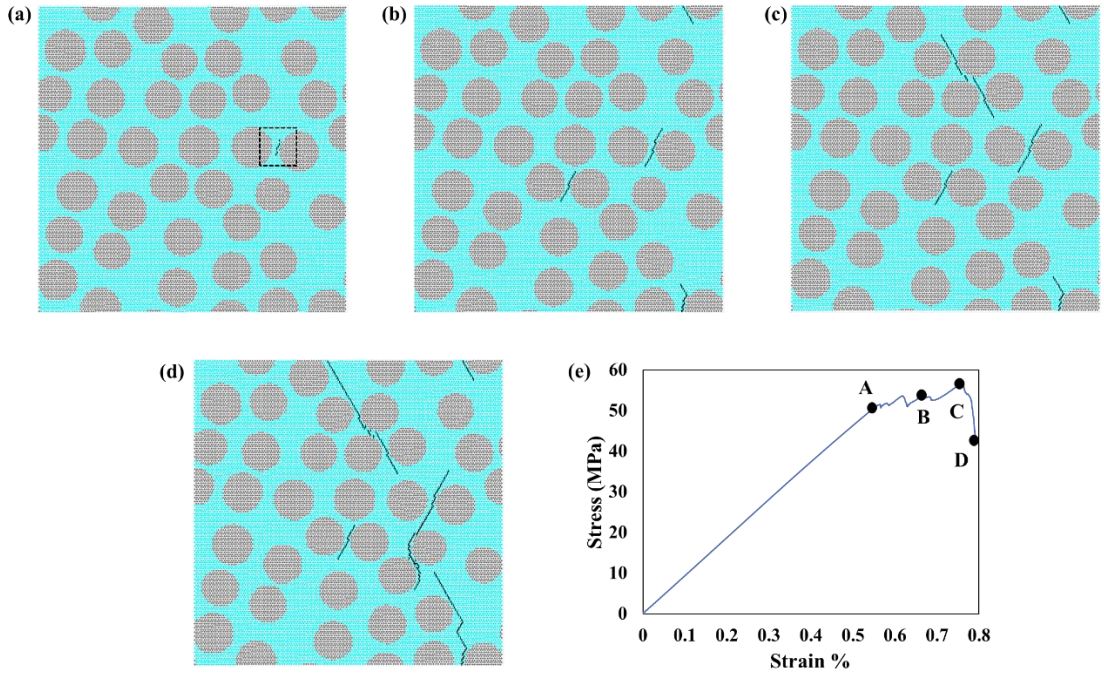

Figure 3-6: The mechanical behaviour of an RVE with $V_f = 45\%$ under transverse tension. (a-d)Cracks at the strains of 0.558%, 0.621%, 0.76% and 0.791%. (e)Stress-strain curve.

The mechanical behaviour of an RVE with $V_f = 60\%$ under transverse tension is presented in Figure 3-7. The crack also initiates from the places with fibres with very closed inner distances at the strain of 0.401%. Then several cracks occur and grow in the matrix until the stress reaches the peak stress. After that, the stress decreases, and the cracks coalesce, forming the crack path at the failure. The strength of the RVE containing 60% randomly distributed fibres is 62.84MPa (point C in Figure 3-7(e)), which is larger than that of the RVE containing 45% fibres (56.17MPa at point C in Figure 3-6(e)). It is indicated that the RVE with a larger fibre volume fraction is stronger. When it comes to the strain, the RVE with a larger ratio of fibres has a smaller strain until the failure (see the two points D in Figure 3-6(e) and Figure 3-7(e)).

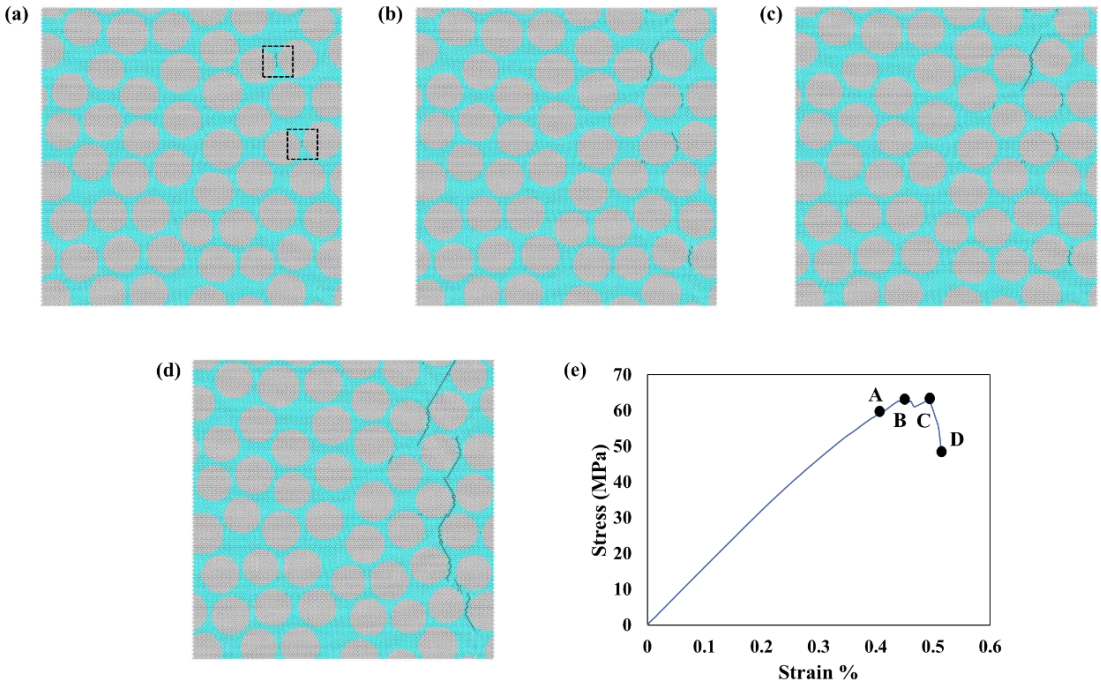

Figure 3-7: The mechanical behaviour of an RVE with $V_f = 60\%$ under transverse tension. (a-d)Cracks at the strains of 0.413%, 0.451%, 0.494% and 0.515%. (e)Stress-strain curve.

3.3 DNN predictive model for macroscopic transverse properties

Based on the accurate and reliable results obtained from the DEM model, a deep learning model, the deep neural network (DNN) regression model, is developed to predict the macroscopic transverse properties of a UD FRP lamina and efficiently.

3.3.1. Design of Experiments (DoE) sampling and data generation

To maximise the performance of a data-driven predictive model, an appropriate and high-quality data set that can represent the overall properties of a specific problem is required. This sub-section mainly studies the mechanical properties of UD FRP composite laminae affected by various fibre volume fractions and radii. In other words,

the microstructures of the composite are varied by changing these two variables, which results in the distinct fibre distribution of each microstructure. In this study, the fibre volume fractions and fibre radii are set in the ranges $40\% - 60\%$ and $3\ \mu m - 5\ \mu m$ as listed in Table 3-3, respectively, which are proved to cover the commonly used UD FRP composite laminae [141, 142].

Table 3-3: Two variables in DoE and their lower and upper bounds.

Parameters (DoE)	Lower Bound	Upper Bound
Fibre volume fraction, V_f	40%	60%
Fibre radius, R_f (μm)	3	5

To describe the slight variation of information under their corresponding conditions, the Design of Experiments (DoE) is commonly used to reflect the variation. The sampling technique, Latin Hypercube sampling (LHS), can be implemented to generate averagely distributed data points in the problem domain. It is a stratification-based sampling method. As shown in Figure 3-8, if five sets of samples are to be drawn in the domains, each of the domains will be divided into five parts, and one set of the sample will be randomly drawn in the domains.

Latin Hypercube sampling (LHS) is employed to determine the different sets of the two independent variables (fibre volume fraction and fibre radius) given their corresponding boundaries (see Table 3-3). 200 sets of samples are selected by means of the standard LHS. The algorithm of the standard LHS is coded using the commercial software MATLAB.

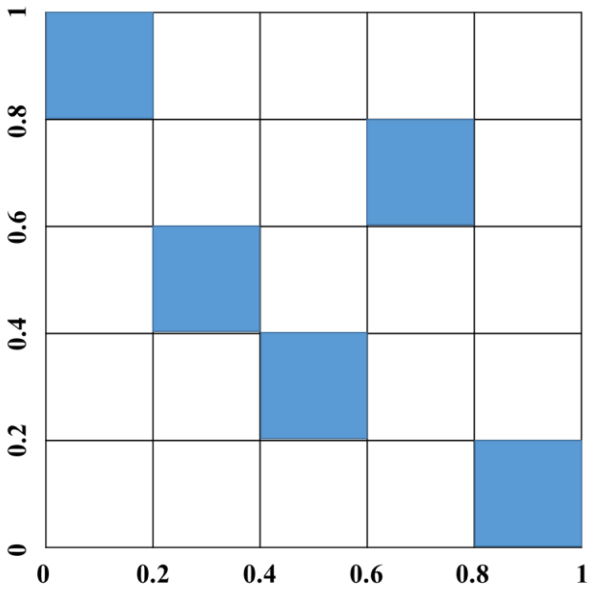

Figure 3-8: An example of using Latin Hypercube sampling (LHS) in the domains of [0, 1] and [0, 1].

For a chosen combination of the volume fraction and fibre radius, 10 RVEs with different fibre distributions are generated. A total of 2000 RVEs are then simulated using the 2D DEM model described in the previous sections. The transverse tensile strength Y_T is defined as the maximum stress in a loading process. The Young's modulus E_T is the ratio of stress to strain in the elastic deformation stage. The transverse tensile strength and Young's modulus are extracted from the DEM simulation output file. The extraction of transverse tensile strength and calculation of Young's modulus are coded and implemented in Python.

To minimize the variations of mechanical properties caused by different random fibre distributions, the average values for the two mechanical properties from every 8 out of 10 samples that have the same fibre volume fraction and fibre radius (by removing the maximum and minimum values in every 10 results) are calculated. The average tensile strength and average Young's modulus over every 10 RVEs that have the same volume fraction and fibre radius, but different fibre distributions are plotted in

Figure 3-9, where the variances of the respective average are also shown. It can be seen that the variance of the tensile strength is relatively larger than that of Young's modulus, which suggests that fibre distribution may have a greater influence on the tensile strength than Young's modulus of the composite. The 200 sets of fibre volume fraction and fibre radius selected by the DoE and their predicted average strength and Young's modulus from the DEM simulations are used then as the input data and output data to be trained by deep learning.

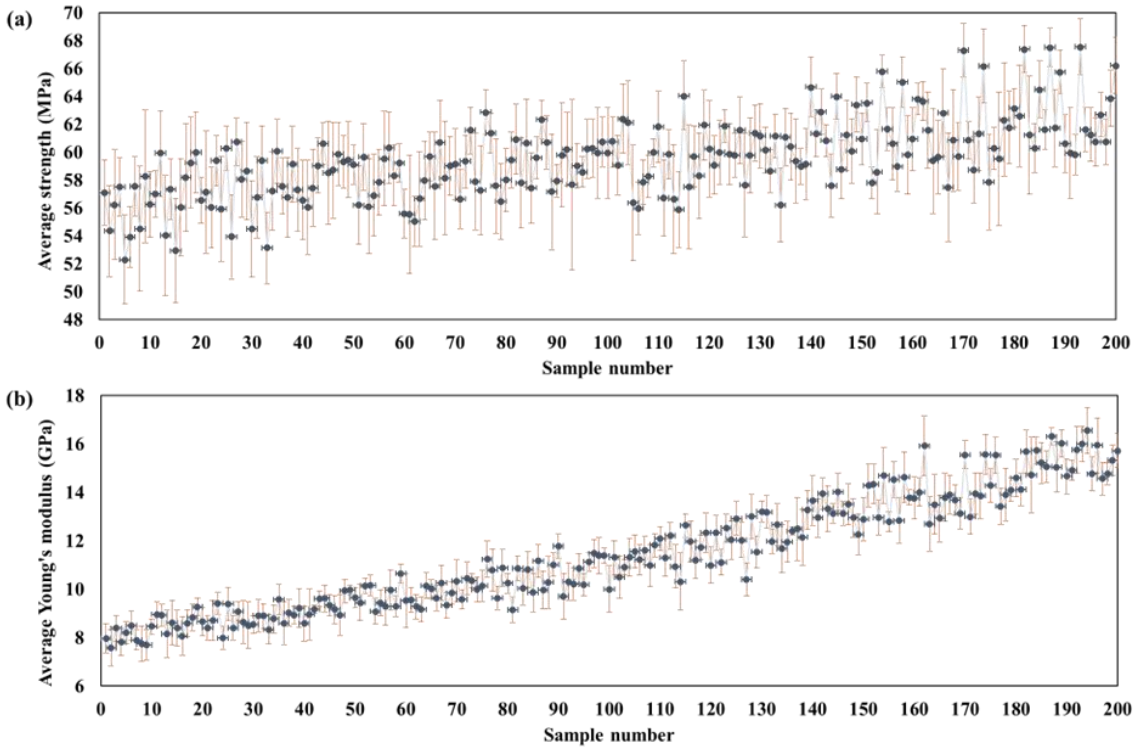

Figure 3-9: Variance plot for (a)the average tensile strength and (b)the average Young's modulus.

3.3.2. Data pre-processing

Before determining the structure of the DNN predictive model, data pre-processing is carried out. It is one of the essential steps in developing data-driven models, as the quality of the data of representative features directly determines the performance of a

machine learning model. Data pre-processing includes data set partition and data normalization.

To improve the model performance, three different groups of data processed by a 3-fold cross-validation and implemented in Python, are used for training and testing the predictive model. In each group of the data, 80% of data points in the data set (160 data points) are used in the training process, and the rest 20% of data points (40 data points) are used in the testing process.

The input features and target output vary in magnitude, which affects the efficiency and accuracy of machine learning predictions. Thus, it is crucial to apply a data normalization method to convert the magnitudes of data to a same scale. Two common methods, namely min-max normalization and Z-score normalization, bring different features into the same scale and will be used in this analysis to compare their performances in the predictive model. The normalization processes are coded, respectively, using the MinMaxScaler function and the StandardScaler function in the scikit-learn module of Python. In the process of data normalization, scaling of the input features and the target outputs in the training set is done independently. The same scaling is also applied to the testing set.

3.3.3. Configuration of the DNN predictive model for the macroscopic transverse properties

A DNN model with a back-propagation learning algorithm is used to predict two macroscopic mechanical properties (the transverse tensile strength Y_T and Young's modulus E_T), which allows forward signal transmission and error back propagation simultaneously during the training process. The activation function used from the input

layer to the first hidden layer and between any two hidden layers is the rectified linear activation function (ReLU):

$$f(x) = \begin{cases} 0, & if\ x \leq 0 \\ x, & if\ x > 0 \end{cases} \tag{3-5}$$

This activation function enables more efficient gradient descent and backpropagation. It can also reduce the overall computational cost of the neural network.

The Sigmoid function is used between the last hidden layer and the output layer:

$$f(x) = \frac{1}{1 + e^{-x}} \tag{3-6}$$

This function is monotonically continuous in the output interval, thus, it is best used in the output layer.

In addition, to ensure that the DNN model can have sufficient accuracy, a set of trials using the models with different numbers of hidden layers and neurons are made. It is found that the predictions by using DNN models containing less than four layers with less than 80 neurons in each layer are 'underfitting', which means the DNN models do not learn well in the training process. It is also found that the predictions by using the DNN models containing more than four layers with more than 80 neurons in each layer are 'overfitting', suggesting that the DNN models learn very well in the training process due to the powerful nonlinear mapping capabilities, while may not give accurate predictions in the testing process. Therefore, as shown in Figure 3-10, the DNN regression model with back-propagation, consisting of four hidden layers with the same neuron number of 80 in each layer, has the best nonlinear mapping capabilities in this case. The generated DNN predictive model is implemented by using Keras functions of the TensorFlow package in Python [143, 144].

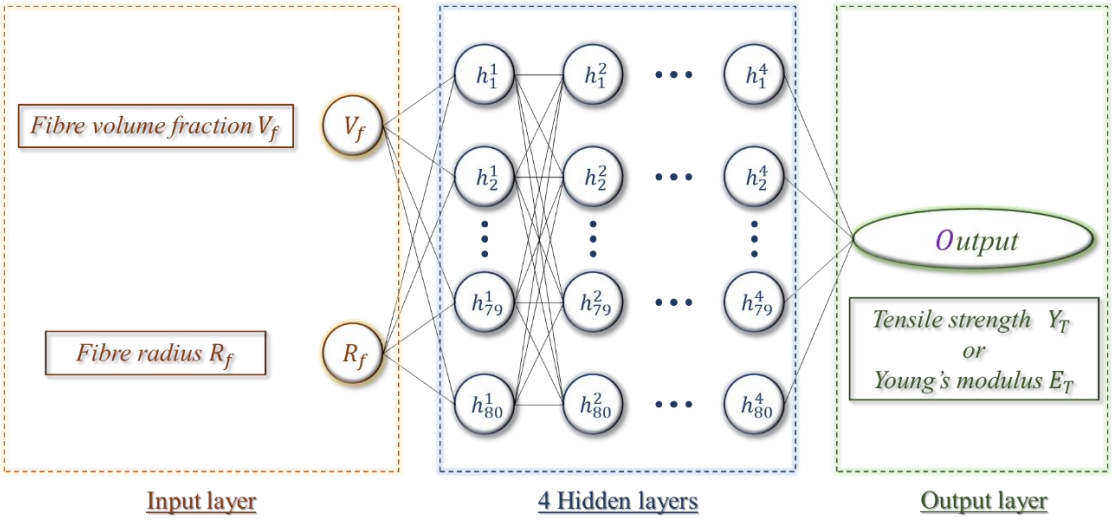

Figure 3-10: A multi-layer DNN model for the predictions of transverse mechanical properties.

3.3.4. Results of the DNN model for the transverse tensile strength

Figure 3-11 and Figure 3-12 show the transverse tensile strength of the UD FRPs obtained from the DEM simulations and the DNN predictive model and their comparisons using the Min-max normalization and Z-score, respectively normalization methods to process the input and output data. The training results of the DNN model on three cross-validation groups of data are shown in Figure 3-11(a-c) and Figure 3-12(a-c), which show satisfactory comparisons. These are scatter plots for a better visual indication of the correlation between the DNN training results and DEM simulations. In the training process, all the points from the DEM and DNN predictions are scattered around the diagonal line (indicating 100% agreement). The results on three different groups of data in the testing process of the DNN model using two data normalization methods are presented in Figure 3-11(d-f) and Figure 3-12(d-f), respectively. Similar conclusions can be made based on the comparisons. The DNN predictive model is sufficiently accurate in predicting the transverse tensile strength of the UD FRP with a

range of fibre volume fractions and fibre radii. Though Figure 3-11(d-f) and Figure 3-12(d-f) show a slightly more scattered pattern, all the points are still within a reasonably close range of the diagonal.

To assess the accuracy and effectiveness of the predictive model, the performance indicators are used for both the training and testing processes. The comparisons of the performance indicator (R^2) of the DNN model in predicting tensile strength of the UD FRP in both the training and testing processes are presented in the figures (see Figure 3-11 and Figure 3-12), respectively, for the Min-max and the Z-score normalizations. For the R^2 indicator, a value closer to 1 suggests a better prediction. It is shows that for both training and testing, Min-max normalization performs better than the Z-score normalization as larger values of R^2 are obtained from using the Min-max normalization.

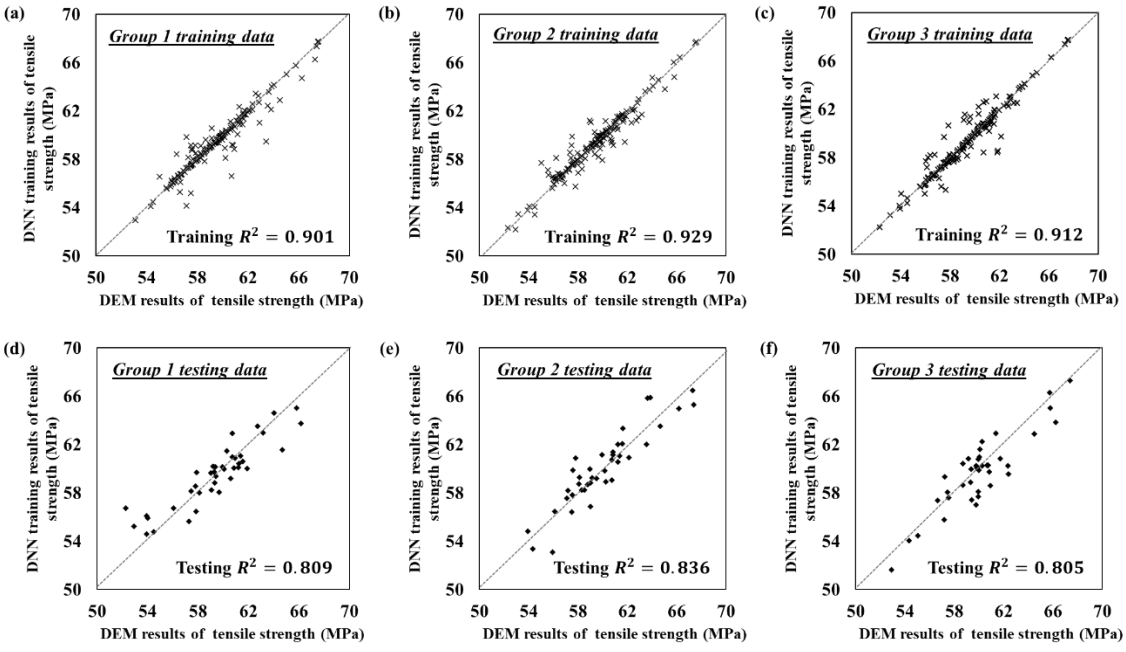

Figure 3-11: Comparison of the training results and prediction results for the transverse tensile strength using 3-fold cross-validation under Min-max normalization. (a-c) Training results of Group 1, Group 2 and Group 3. (d-f) Testing results of Group 1, Group 2 and Group 3.

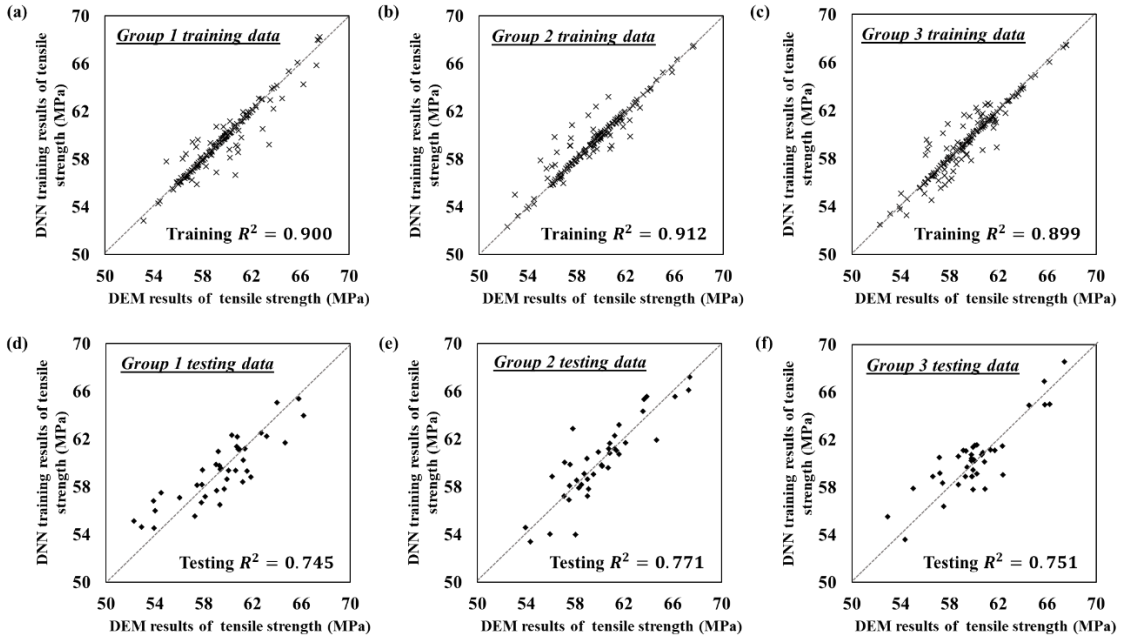

Figure 3-12: Comparison of the training results and prediction results for the transverse tensile strength using 3-fold cross-validation under Z-score normalization. (a-c) Training results of Group 1, Group 2 and Group 3. (d-f) Testing results of Group 1, Group 2 and Group 3.

To better show the results, Figure 3-13 and Figure 3-14 are the DEM simulation results, and the DNN predicted results of the transverse tensile strength based on the group 1 data processed by the two normalization methods. And the comparisons of the performance indicators in the DNN model for the prediction of the transverse tensile strength based on group 1 data are also presented in Table 3-4. Two more performance indicators are used, namely, MSE and MAE.

Figure 3-13(a) and Figure 3-14(a) are the training results for the 128 sets of data and the validation results of the last 32 sets of data against the DEM simulations. It is seen that the DNN training results are very close to the DEM simulation results. Figure 3-13(b) and Figure 3-14(b) are scatter plots between the DNN results and the DEM simulations in the training process, which shows that the training accuracy is quite good. The high accuracy of the training process can also be concluded from the values of the

performance indicators in Table 3-4(a). As both MSE and MAE are close to zero and R^2 values reach 0.9. The results of the testing process of the DNN model using the two data normalization methods are presented in Figure 3-13(c-d) and Figure 3-14(c-d), respectively. Moreover, Table 3-4(b) shows that all three indicators for the testing process suggest better performance from using group 1 data processed by the Min-max normalization than from the one processed by the Z-score normalization. Because both MSE and MAE obtained using Min-max normalization are much closer to zero. And the corresponding R^2value is 0.8094 which is higher than the one obtained using the Z-score normalization (0.7448).

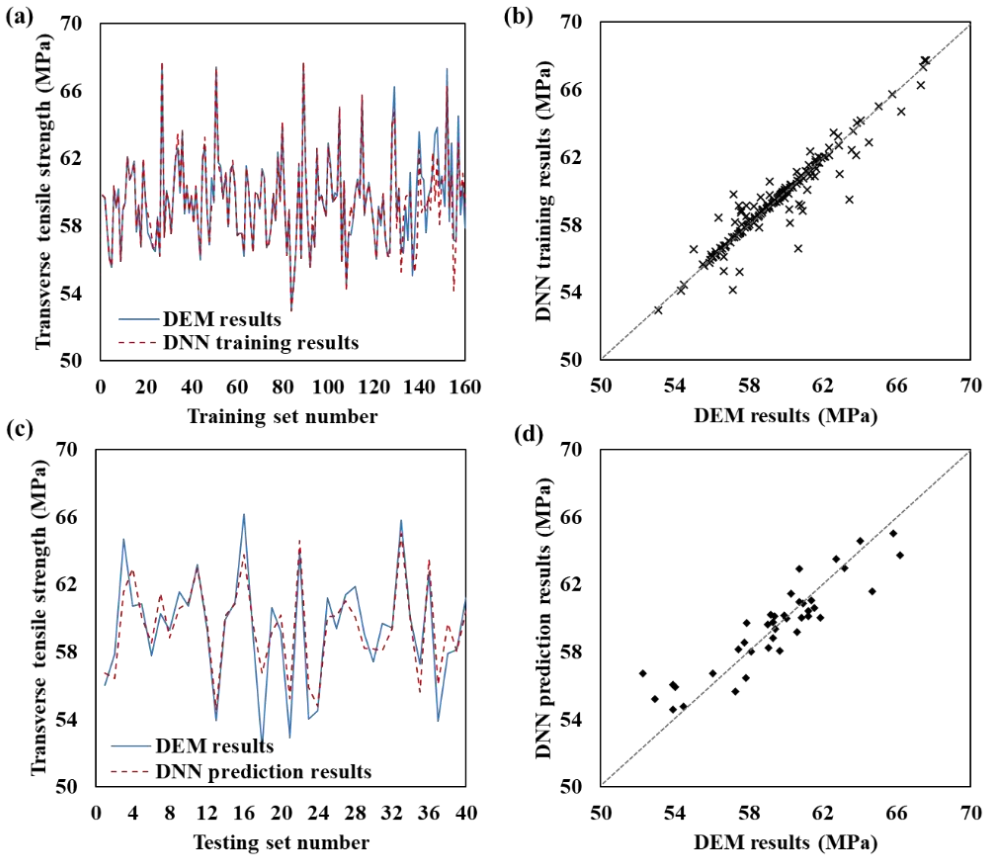

Figure 3-13: Comparison of the training results and prediction results for the transverse tensile strength based on group 1 data under Min-max normalization.

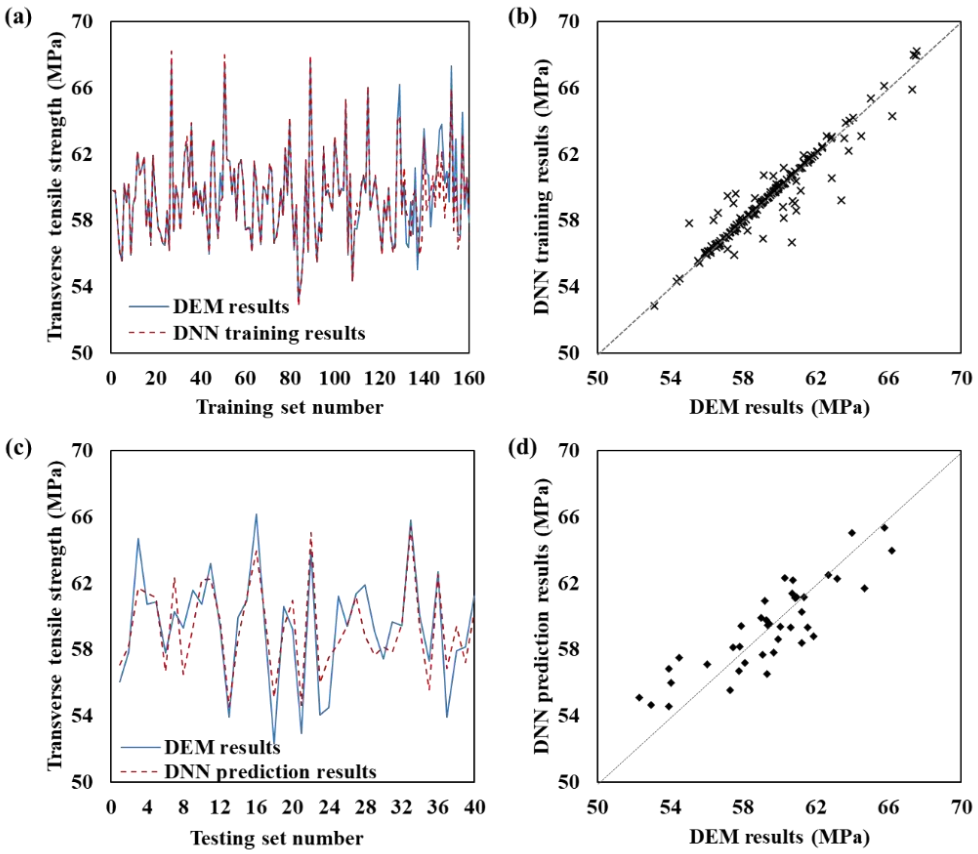

Figure 3-14: Comparison of the training results and prediction results for the transverse tensile strength based on group 1 data under Z-score normalization.

Table 3-4: Comparisons of the performance indicators in the DNN model for the prediction of the transverse tensile strength based on group 1 data. (a)Training process. (b)Testing process.

Methods	Training MSE	Training MAE	Training R^2
Min-max normalization	2.977e-3	2.748e-2	0.9014
Z-score normalization	9. 065e-2	1.442e-1	0.9000

(a)

Methods	Testing MSE	Testing MAE	Testing R^2
Min-max normalization	8.730e-3	7.166e-2	0.8094
Z-score normalization	3.508e-1	4.906e-1	0.7448

(b)

3.3.5. Results of the DNN model for Young's modulus

Similar to the discussion for the prediction results of the transverse tensile strength, the results of training and prediction of the developed DNN model on the three cross-validation groups of data for the transverse Young's modulus are analysed and shown in Figure 3-15 and Figure 3-16, respectively. As shown in Figure 3-15(a-c) and Figure 3-16(a-c), the training results of the three different groups using the Min-max normalization and the Z-score normalization are both very close to the DEM model results. The comparisons demonstrate that the accuracy of the training process is very high. The transverse Young's modulus predicted in the testing process of the DNN model is shown in Figure 3-15(d-f) and Figure 3-16(d-f), respectively, for the two normalization methods and compared with also the DEM results. It can be seen that in general, the testing results are accurately predicted by the developed DNN model because they are all very close to the diagonal line. In more detail, the performance indicator R^2 of the predictions are all very close to 1. It can be concluded that the DNN model works efficiently and accurately in predicting the transverse Young's modulus of UD FRP composite laminae.

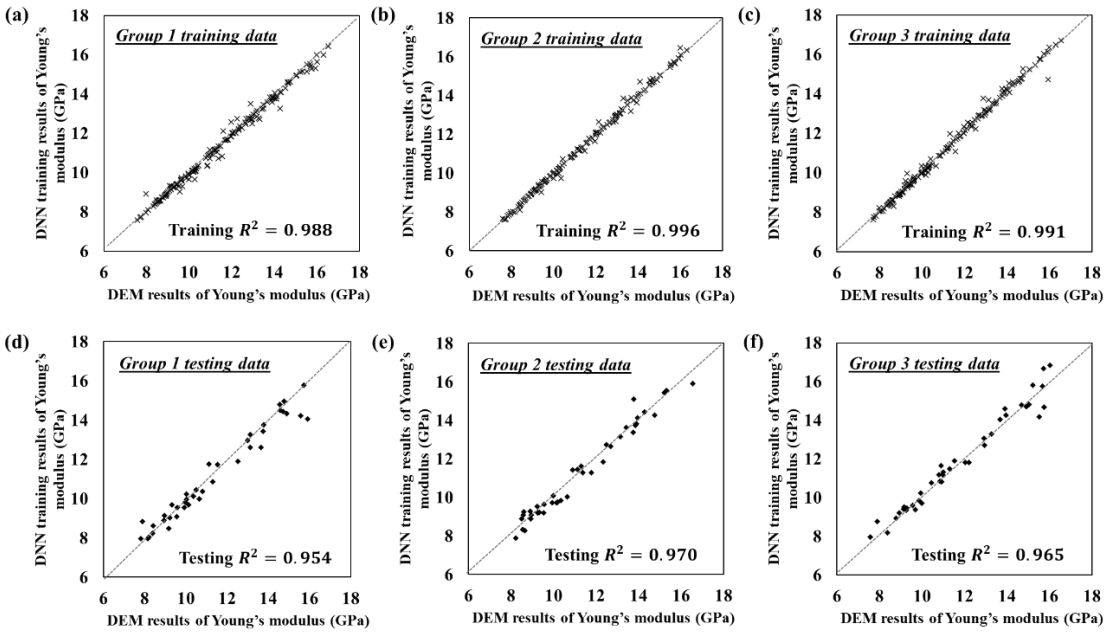

Figure 3-15: Comparison of the training results and prediction results for the transverse Young's modulus using 3-fold cross-validation under Min-max normalization. (a-c) Training results of Group 1, Group 2 and Group 3. (d-f) Testing results of Group 1, Group 2 and Group 3.

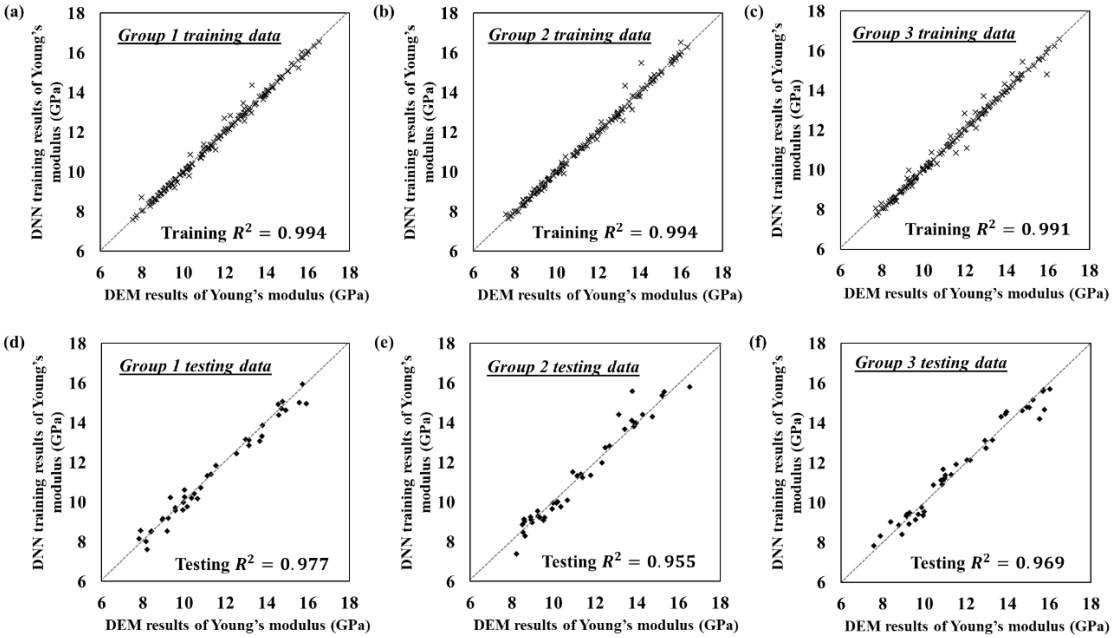

Figure 3-16: Comparison of the training results and prediction results for the transverse Young's modulus using 3-fold cross-validation under Z-score normalization. (a-c) Training results of Group 1, Group 2 and Group 3. (d-f) Testing results of Group 1, Group 2 and Group 3.

Figure 3-17 and Figure 3-18 show more detailed results for the transverse Young's modulus based on group 1 data. As shown in Figure 3-17(a) and Figure 3-18(a), the training and the validation results obtained from the training process using the Min-max normalization and the Z-score normalization are very close to the DEM model results, which are illustrated by the direct comparisons shown in Figure 3-17(b) and Figure 3-18(b) between the two sets of results. The comparisons demonstrate that the accuracy of the training process is very high. Also, the performance indicators of the training process are shown in Table 3-5(a), where the MSE MAE of the training are very close to zero and the R^2 values (0.9540 and 0.9773) are very close to 1. The transverse Young's modulus predicted in the testing process of the DNN model is displayed in Figure 3-17(c-d) and Figure 3-18(c-d), respectively, for the two normalization methods and compared with also the DEM results. Combined with the results of performance indicators of the testing process (see Table 3-5(b)), it is seen that the accuracy of the testing process is very high. It is indicated that the DNN predictive model can be used as an alternative to the DEM model to predict Young's modulus.

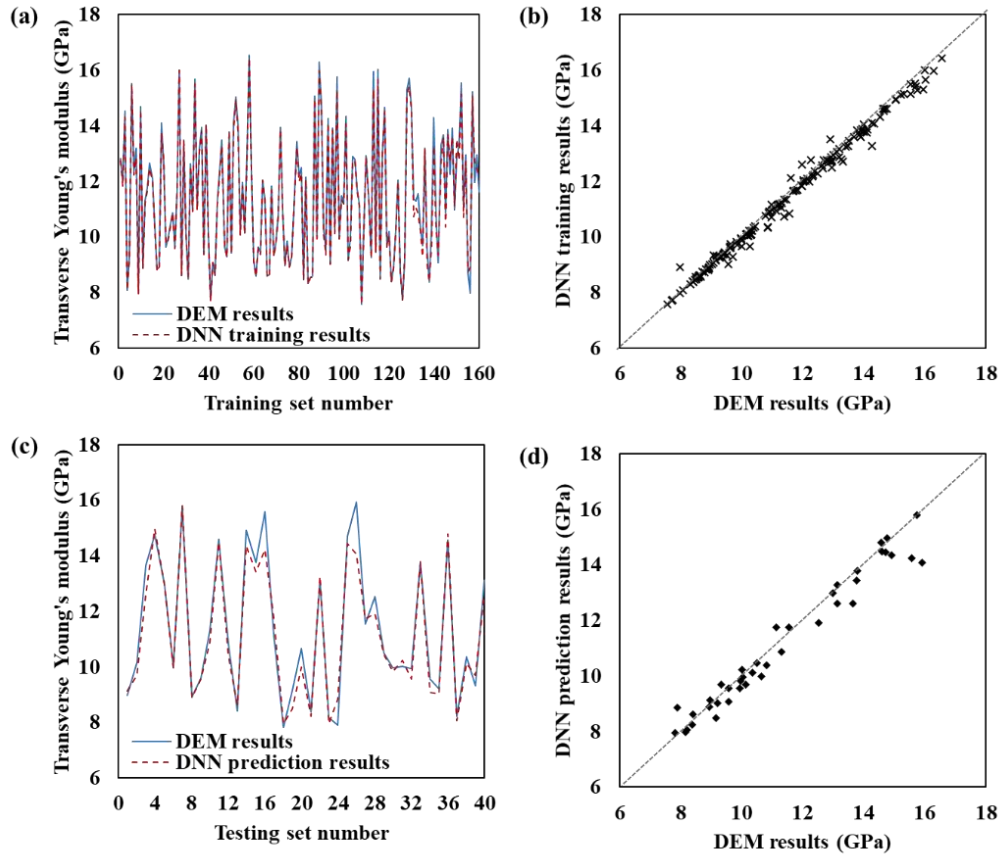

Figure 3-17: Comparison of the training results and prediction results for the transverse Young's modulus based on group 1 data under Min-max normalization.

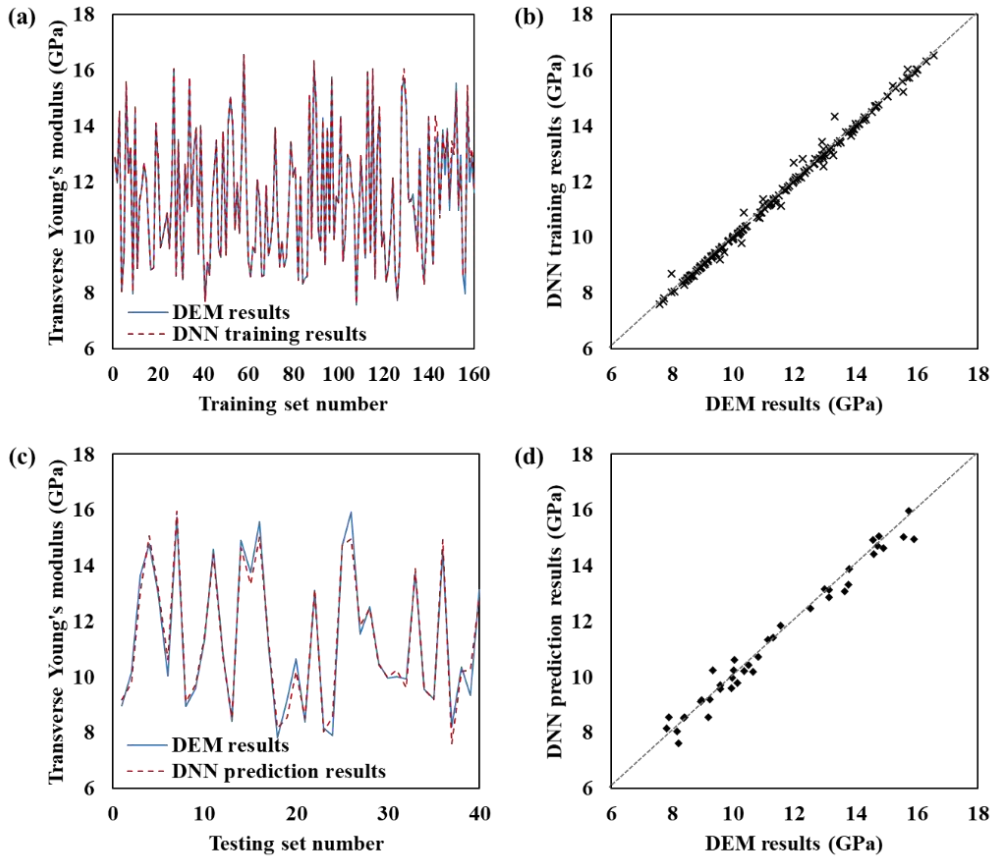

Figure 3-18: Comparison of the training results and prediction results for the transverse Young's modulus based on the group 1 data under Z-score normalization.

Table 3-5: Comparisons of the performance indicators in the DNN model for the prediction of the tensile Young's modulus based on group 1 data. (a)Training process. (b)Testing process.

Methods	Training MSE	Training MAE	Training R^2
Min-max normalization	7.415e-4	1.737e-2	0.9885
Z-score normalization	5.680e-3	3.621e2	0.9941

(a)

Methods	Testing MSE	Testing MAE	Testing R^2
Min-max normalization	3.512e-3	4.177e-2	0.9540
Z-score normalization	2.589e-2	1.237e-1	0.9773

(b)

3.3.6. The validation of DNN predicted Young's modulus

To further verify the DNN predictive model, the transverse Young's modulus predicted by DEM and DNN are also compared with two existing analytical micromechanics models, i.e., the Slab model and the Halpin-Tsai model, the details of which are summarized in Table 3-6. In Table 3-6, E_T is the transverse Young's modulus; E_f and E_m are the transverse Young's modulus of the fibre and matrix, respectively; V_f and V_m are the respective volume fractions of fibre and matrix. The ratio, a/b, is the cross-sectional aspect ratio of the reinforcement. Figure 3-19 presents the transverse Young's modulus calculated by the two analytical models, the DEM simulations and the DNN predictions based on 40 RVE samples over the whole range ($40\% - 60\%$) of fibre volume fractions considered in this study. It can be seen from Figure 3-19 that the Slab model gives the lowest value of Young's modulus. The DNN predictions show a similar form of non-linearity as the DEM model. Compared to the Slab model, the Halpin-Tsai model is more comparable to the DEM and DNN predictions. In general, the DEM and DNN predictions are lower than the predictions from the Halpin-Tsai model when the volume fraction is below 48% and higher when the volume fraction is over 48%. Apart from the various assumptions that were introduced to derive the analytical, numerical and machine learning models, factors that attribute to the discrepancies between the DNN and the analytical models include the impact of the randomly distributed fibres and their diameters that were not considered in the analytical models but have been properly modelled in the DEM model and, subsequently, reflected in the DNN model.

Table 3-6: Two analytical micromechanics models for transverse Young's modulus.

Model	Transverse Young's modulus
Slab model	$\frac{E_T}{E_m} = \frac{E_f}{V_f E_m + V_m E_f}$
Halpin-Tsai Equations	$\frac{E_T}{E_m} = \frac{1+\xi\eta V_f}{1-\eta V_f}$, where $\eta = \frac{\frac{E_f}{E_m}-1}{\frac{E_f}{E_m}+\xi}$ and $\xi = 2(a/b)$

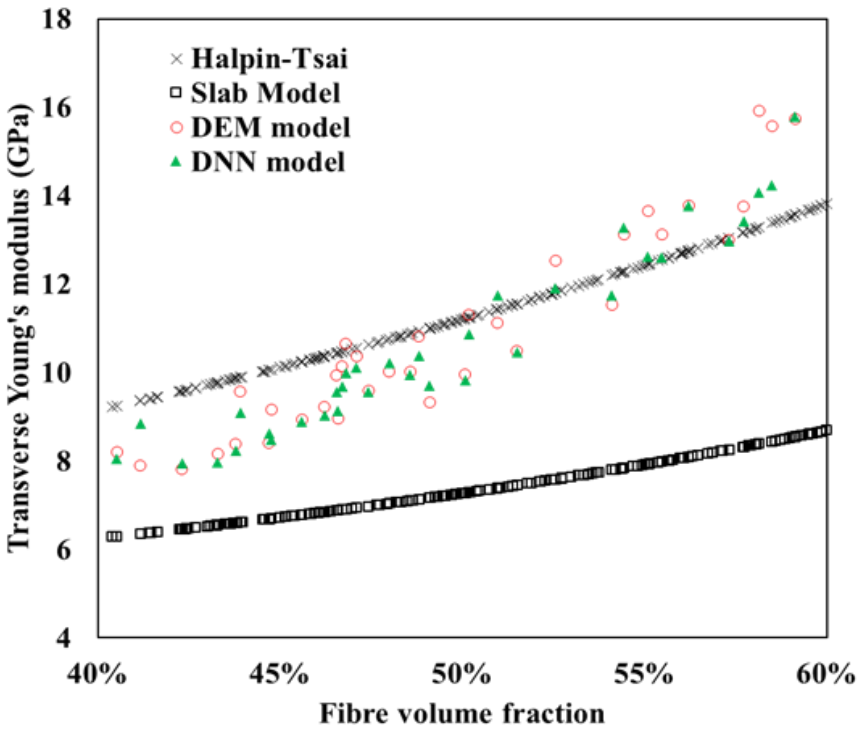

Figure 3-19: Comparison of the transverse Young's modulus determined by two analytical models, the RVE-based DEM model and the DNN predictive model.

3.4 Summary

In this chapter, firstly, an RVE-based DEM model is developed for studying the mechanical behaviours of UD FRP laminae subject to transverse tension. The transverse mechanical properties of the UD FRP laminae predicted by the developed DEM model show good agreement with the results of the experimental tests. The DEM simulated stress-strain responses of RVEs agree well with that of the FEM analyse. The RVEs based on the different settings of fibre volume fractions are analysed. It is found that the strength of the UD FRP lamina becomes larger with the increase of fibre volume fractions. However, the deformation until reaching the failure point becomes smaller. In addition, it is shown that the crack usually occurs in the matrix where the distance between the two fibres is very small. Then the crack propagates through the matrix until the failure. It can be concluded that the DEM model shows its advance in tracking crack initiation and propagation.

Then, based on a large amount of RVE-based DEM model simulations, a multi-layer DNN model with back-propagation is constructed for predicting two transverse mechanical properties (tensile strength and Young's modulus) of an FRP composite lamina at the macroscopic level with consideration of two features related to the fibre distribution. The DNN model shows good accuracies for predicting the two categories of mechanical properties when three different groups of data under two different types of normalizations are trained. Moreover, the verification of the DNN model for Young's modulus shows that the DNN model is superior to two existing analytical models, as the impact of the randomly distributed fibres and their diameters can be considered in the DNN model. Therefore, it can be concluded that the DNN model has robust abilities in predicting both the transverse tensile strength and Young's modulus of the UD FRP composite lamina accurately.

Chapter 4

4 Predictions of microscopic cracks of unidirectional fibre-reinforced polymer composites using machine learning

The fracture process in composite materials has been studied for a long time. Computational micromechanical methods have been taken to investigate the fracture prediction for composites subjected to different loadings, however, it usually takes a long time to achieve the crack initiation and propagation as well as the final failure as modelling micro-scale fracture mechanics is time-consuming. The machine learning prediction for the macroscopic mechanical properties of UD FRP laminae based on the data from the DEM model shows its great potential. In this chapter, the data extracted by DEM model simulations are also used for machine learning models to predict the microscopic cracks of UD FRP composites.

4.1 ML predictive model for the microscopic cracks

The first try for predicting the microscopic cracks in the RVE of the UD FRP lamina using ML models aims to find the complexity of the problem. In other words, it is necessary to understand the relationship between the input and the target output in the prediction problem.

4.1.1. Data generation and pre-processing

The developed 2D RVE-based DEM model in Chapter 3 is used for simulating fracture processes in RVEs of FRP composite laminae. The scale of the RVE is smaller

than that being used in the DEM simulation mentioned in Chapter 3. There are two reasons for reducing the scale of the RVE. The first reason is that running enough simulations of the original scale of RVEs takes longer. The second reason is that using a relatively small size of the data at an early stage to investigate crack prediction via ML models allows the model to be continually revised. Thus, the dimension of the square RVE is set as $10\mu m \times 10\mu m$. The radius of the randomly distributed fibre is $0.815\mu m$ and the volume fraction V_f is 45%. A number of 500 DEM model simulations are first generated. During the DEM simulations, crack paths of all the 500 RVE samples are recorded when the stress is about 70% of their tensile strength.

In the DEM simulation, the RVE is discretised with particles. A contact bond between two particles breaks, and then a crack occurs. For the convenience of the discussion, the particles at the cracking contact bond are called cracking particles. To predict the crack path in the RVE, the ML model is used to predict whether a particle is cracking. It is a binary classification problem with an output of one or zero. Figure 4-1 presents the ML process using data from the DEM simulation. In this classification problem, if there is a crack in the bond between two particles, the particles will be labelled by one. Otherwise, the particles will be labelled by zero. In a supervised classification machine learning, the features are the inputs to the ML model, and the output is a label mapped by the feature vector. The features are essential for training the ML model, which will directly affect the ML prediction. The more specific and valuable information in the given features, the feedback of better accuracy and lower loss will be returned. However, the features related to the properties of the material, for instance, the stress or strain rates in any time steps during the simulation and the condition of transverse tension loading, etc, should not be considered.

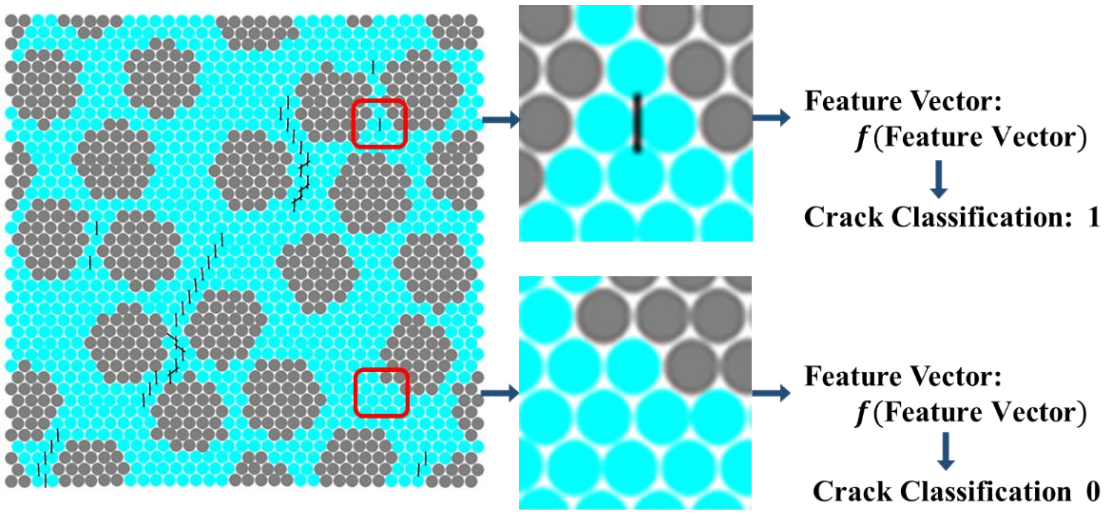

Figure 4-1: Diagram for machine learning process using data from the DEM simulation.

Figure 4-2 shows the selection of the features. A single hexagonal-packed particle in the RVE is considered a data. It is found that the crack path is highly dependent in the fibre distribution. Therefore, the features of each data sample reflect two aspects. One is the position of the particle in the RVE. The other one is the distance and direction of the particle to the randomly distributed fibre in the RVE. Taking a matrix particle as an example (see Figure 4-2), its position is represented by the $x-$ and $y-$ coordinate, (denoted pos_x and pos_y). The distances between the particle to the four boundaries are also considered for better reflecting the position of the particle in the RVE. The distance and direction related to the fibre are marked in Figure 4-2 and denoted by toF_1 and a_1.

Based on the scale and the fibre volume fraction of the generated RVE, there are at least 27 randomly distributed fibres in one RVE. The features we considered are the positions of $x-$ and $y-$ coordinate directions of matrix particles (denoted pos_x and pos_y), the distance between the centre of matrix particle to the left vertical boundary (denoted $dist_{x1}$), the distance between the centre of the matrix particle to the right vertical boundary (denoted $dist_{x2}$), the distance between the centre of the matrix

particle to the lower horizontal boundary (denoted $dist_{y1}$), the distance between the centre of the matrix particle to the upper horizontal boundary (denoted $dist_{y2}$), the distance between the centre of the matrix particle to the centre of the first closed fibre (denoted toF_1) to the distance between the centre of the matrix particle to the centre of the 27th closed fibre (denoted toF_{27}), the angle of the matrix particle to the centre of the first closed fibre (denoted a_1) to the angle of matrix particle to centre of 27th closed fibre (denoted a_{27}). The distance and angle are calculated as:

$$toF_i = \sqrt{(pos\_x - pos\_x_{f_i})^2 + (pos\_y - pos\_y_{f_i})^2} \tag{4-1}$$

$$a_i = arcsin\,(\frac{pos\_y_{f_i}}{toF_i}) \tag{4-2}$$

where $pos\_x_{f_i}$ and $pos\_y_{f_i}$ are the $x-$ and $y-$ coordinates of the centre of fibre i ($i = 1, 2, \ldots, 27$). The number of features of each data point is 60.

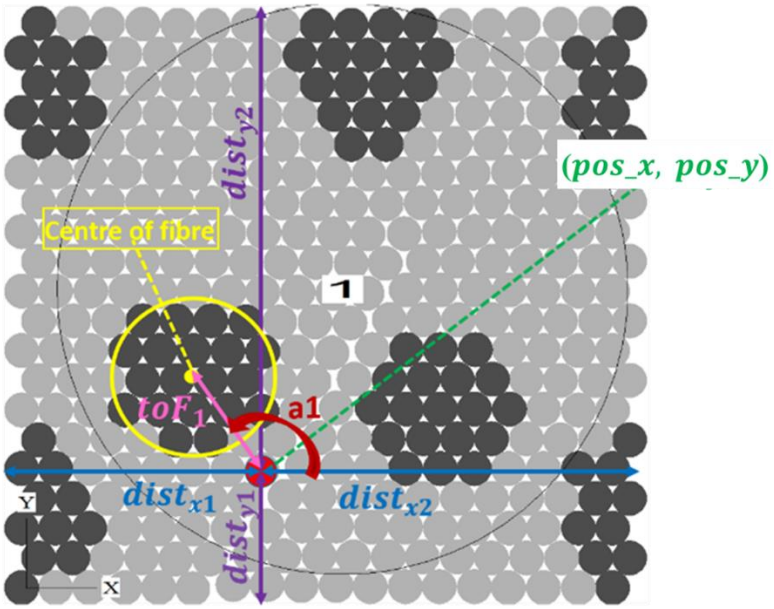

Figure 4-2: Feature extraction from an RVE.

After selecting the input features, the next step is data pre-processing. The cracks occur at some places in the RVE when applying a load. As shown in Figure 4-1, it can be found that the number of particles which is not cracking is overwhelmingly larger

than the number of cracking particles, which causes the problem of data imbalance. There are many methods [145] to solve the data imbalance problem. One commonly-used method is called undersampling. It allows for reducing the number of classes containing overwhelming data. The function of 'undersampling' is performed in Python with its command. In this way, in the training and testing process of the ML model, there will be a fixed amount of data in each RVE, making sure the information from each RVE is learned well and on average by the ML model.

The features vary in magnitude. Thus, the features need to be converted to the same scale using a data normalization method. Min-max normalization is used for rescaling all the data of features.

4.1.2. Development of the ML models

Two different machine learning models, the Gaussian Naïve Bayes classifier and Artificial Neural Networks (ANNs), are employed to predict the crack path. For the Gaussian Naïve Bayes classifier, Python codes can be written for the formulas of the calculation of the conditional probability:

$$\boldsymbol{p}(C_m|x_1, x_2, \dots, x_{60}) = \frac{\boldsymbol{p}(C_m)\, \boldsymbol{p}(x_1, x_2, \dots, x_{60}|C_m)}{\boldsymbol{p}(x_1, x_2, \dots, x_{60})} \tag{4-3}$$

where the vector $\boldsymbol{x} = (x_1, x_2, \dots, x_{60})$ representing the 60 features described in the last sub-section, and C_m for each of the two possible classes C_1 and C_2, i.e., crack or not crack.

The derivation process for the above formula is as follows:

- $\boldsymbol{p}(C_m)$ is calculated as:

$$\boldsymbol{p}(C_m) = \frac{N_{C_m}}{N} \tag{4-4}$$

where N is the total number of samples in the data set, and N_{C_m} is the number of the samples with class C_m. In our prediction problem, N is the total number of particles in the data set, N_{C_1} is the number of particles at the cracking contact bonds, and N_{C_2} is the number of particles at the non-cracking contact bonds.

- The features we considered are all continuous data. The probabilities for the input features for each class is calculated as:

$$\boldsymbol{p}(x_i|C_m) = \frac{1}{\sqrt{2\pi\sigma_{x_i|C_m}^2}} e^{-\frac{(a-\mu_{x_i|C_m})^2}{2\sigma_{x_i|C_m}^2}} \tag{4-5}$$

where a, $\mu_{x_i|C_m}$, and σ_{x_i} are the value, the mean, and the standard variance of the feature x_i for a given class C_m, respectively. The mean and the standard variance are obtained by:

$$\mu_{x_i|C_m} = \frac{1}{N_{C_m}} \sum x_i \tag{4-6}$$

$$\sigma_{x_i} = \sqrt{\frac{1}{N_{C_m}} \sum (x_i - \mu_{x_i|C_m})^2} \tag{4-7}$$

where $\sum x_i$ is the sum of values of the input feature x_i for a given class C_m. Then, we have

$$\boldsymbol{p}(x_1, x_2, \dots, x_{60}|C_m) = \boldsymbol{p}(C_m) \prod \boldsymbol{p}(x_i|C_m) \tag{4-8}$$

- $\boldsymbol{p}(x_1, x_2, \dots, x_{60})$ is a constant, therefore, we have

$$\boldsymbol{p}(C_m|x_1, x_2, \dots, x_{60}) \propto \boldsymbol{p}(C_m)\, \boldsymbol{p}(x_1, x_2, \dots, x_{60}|C_m) \tag{4-9}$$

- Finally, the conditional probability $\boldsymbol{p}(C_m|x_1, x_2, \dots, x_{60})$ is given by

$$\boldsymbol{p}(C_m|x_1, x_2, \dots, x_{60}) = \boldsymbol{p}(C_m) \prod \boldsymbol{p}(x_i|C_m) \tag{4-10}$$

In a binary classification problem, the output will be one if the conditional probability is larger than 0.5. Otherwise, the output will be zero.

A feedforward neural network is the second ML model used for the crack path prediction. It is a unidirectional network that only allows the signals to be transmitted in a forward direction. As shown in Figure 4-3, a feedforward network containing two hidden layers with the same neuron number of 300 in each layer is constructed. The activation function used from the input layer to the first hidden layer and between every two hidden layers is 'ReLU'. The activation function used between the last hidden layer and the output is 'Sigmoid'. Both ML models are coded and implemented in Python.

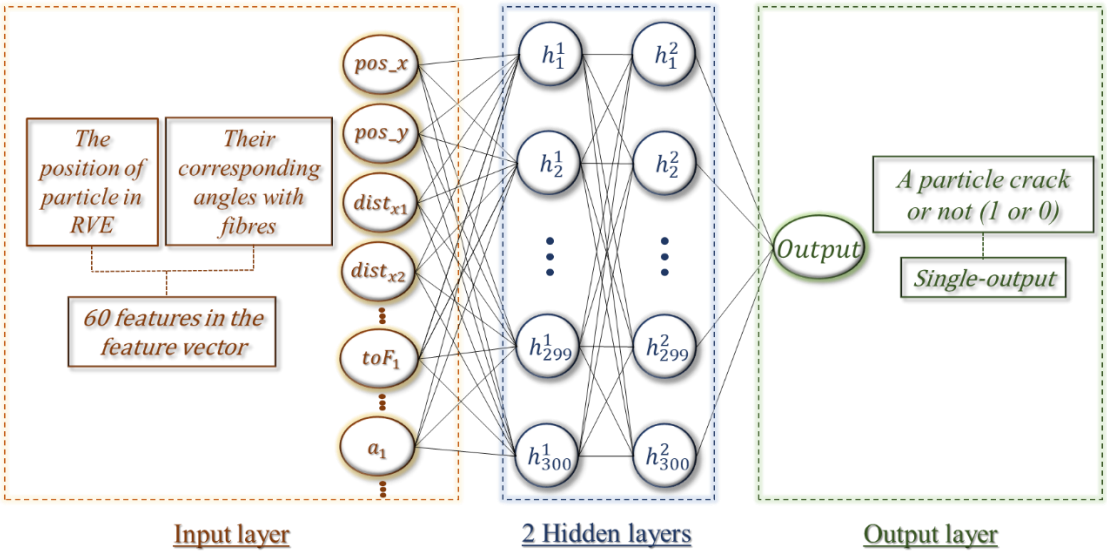

Figure 4-3: A two-layer feedforward ANN model for predicting the crack path.

4.1.3. Results of the Gaussian Naïve Bayes classifier

Gaussian Naïve Bayes classifier is trained on the 80% data points (extracted from 400 simulations) in the dataset to learn the information that leads to particle crack. Then the rest 20% of the data points (extracted from 100 simulations) are tested into the ML

algorithm to validate the accuracy and efficiency of the prediction. A 3-fold cross-validation is employed for investigating the performance of the model.

In the DEM simulation, a crack occurs between two adjacent particles. As shown in Figure 4-4, the DEM simulated cracking contact bonds are the contact bonds that are located between two black particles. The correctly predicted cracking contact bonds by the ML are the contact bonds between particles with a black outer ring and orange interior, while the wrongly predicted cracking contact bonds are the contact bonds between orange particles.

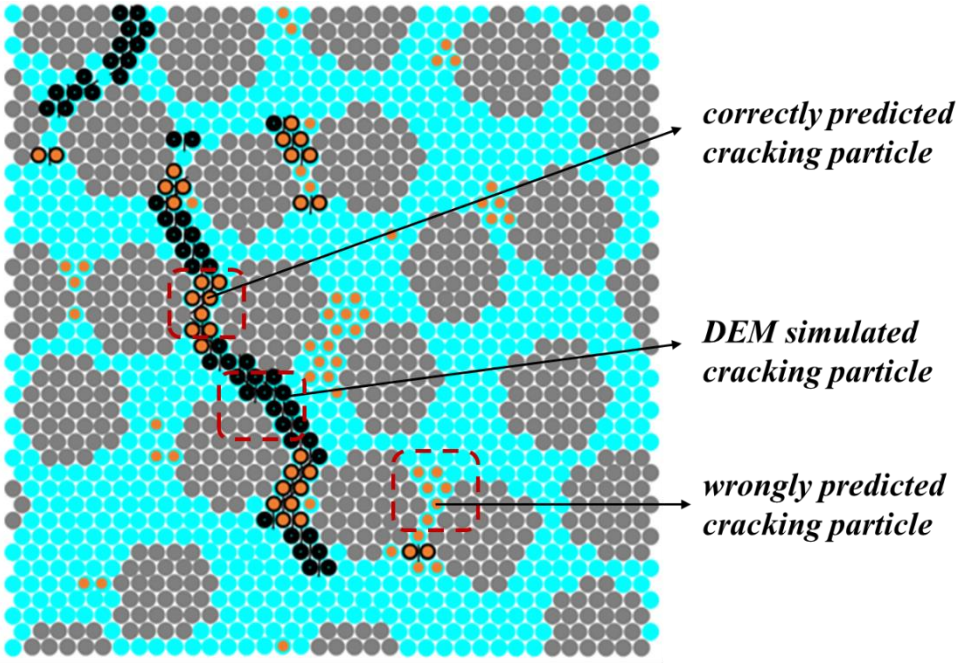

Figure 4-4: Denotation of the DEM simulation results and machine learning predicted results.

Figure 4-5 is an example of the results by Gaussian Naïve Bayes classifier. In one iteration of the 3-fold cross-validation, the data extracted from the RVE shown in Figure 4-5 belongs to the training set. To get the accuracy of the training process, put the data of this RVE into the trained Gaussian Naïve Bayes classifier. The result is presented in Figure 4-5(a). All the cracking particles can be captured after the training process. There are no black particles in the RVE, i.e., all the black particles are coloured by the orange

interior. Though, some orange particles (wrongly predicted particles) are scattered over the RVE. The accuracy of the training process is good.

The data of this RVE can belong to the testing set in the next iteration during the 3-fold cross-validation. In this iteration, the data of this RVE is the unseen data for testing the ML model. The testing result (see Figure 4-5(b)) indicates that the testing performance is not good. Many cracking particles (black particles) are not predicted, and some non-cracking particles (orange particles) are predicted to be cracking. These wrongly predicted particles (orange particles) cluster in several locations in the RVE. According to the results, it can be concluded that the problem of overfitting occurs.

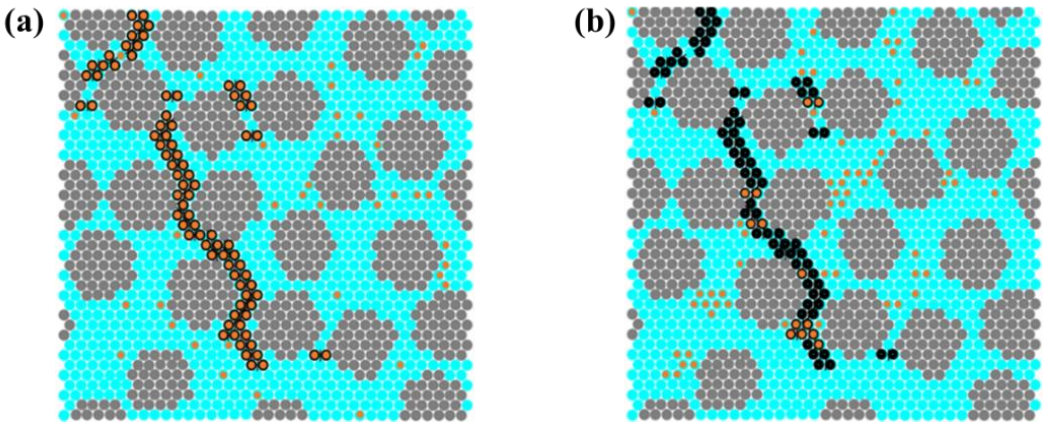

Figure 4-5: (a)Training result and (b)testing result by Gaussian Naïve Bayes classifier.

4.1.4. Results of the ANN model

Similar to the discussion of the results of the Gaussian Naïve Bayes classifier, the performance of the training process of the ANN model is first analysed. From the results obtained from the previous model, it can be seen that the quality of data plays an important role in the ML model. Therefore, the effect of different amounts of training data on the training process of the ANN model is first studied by using different amounts

of data obtained by undersampling. Three different amounts of data in the training set are selected, which are 17.5% training data, 26 % training data, and 40 % training data.

After training the 17.5% data containing the data of the RVE below (see Figure 4-6(a)), it is seen that almost all the cracking particles are predicted, however, there are some wrongly predicted cracking particles (see the orange particles in Figure 4-6(a)). Then 26% of training data is used in the training process, and the result is plotted in Figure 4-6(b). Only two cracking particles are not predicted. As shown in Figure 4-6(a)(b), the number of wrongly predicted cracking particles decreases as the amount of training data increases. Then, the amount of training data is enlarged to 40%. The result in Figure 4-6(c) shows that only one cracking particle is not predicted. Moreover, the number of wrongly predicted cracking particles is significantly decreased compared to the results by training smaller amounts of data. It can be concluded that the accuracy of the training process increases by enlarging the number of training data during the undersampling process.

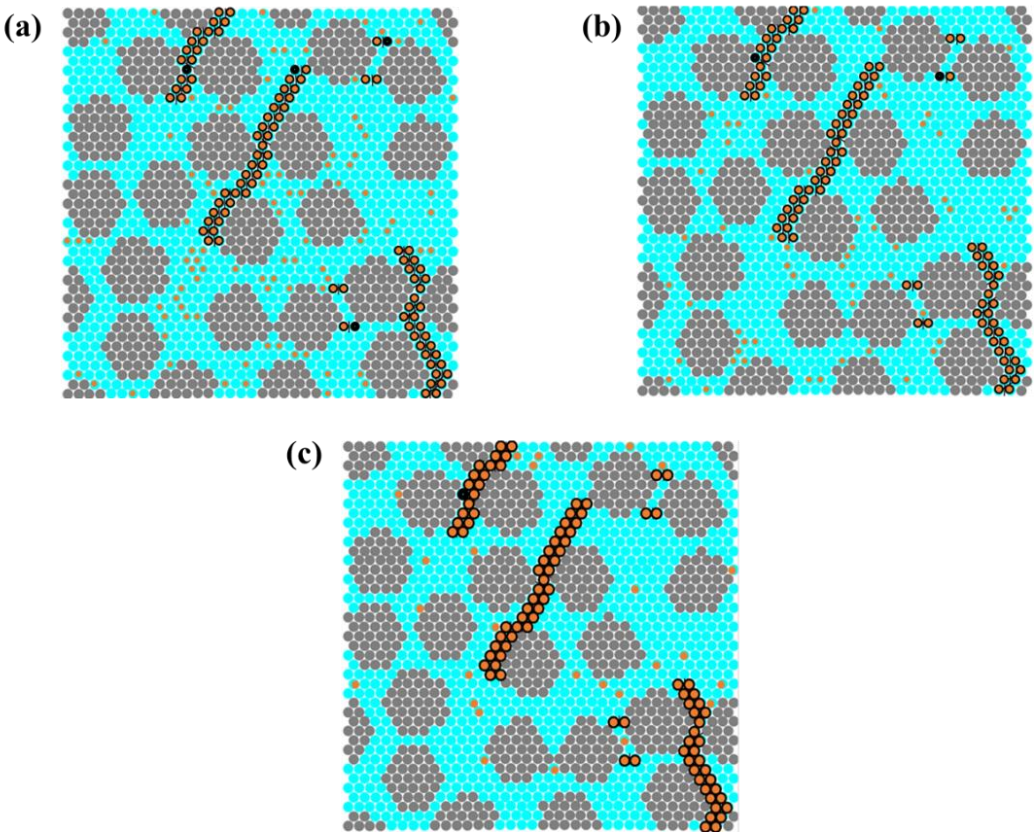

Figure 4-6: ANN training results from using different amounts of data. (a) 17.5% training data. (b) 26 % training data. (c) 40 % training data.

As a result, 40% of training data is chosen for the ANN training and testing. Figure 4-7 shows the training and testing results by the ANN model using 40% of training data. The training result is quite good, with fully predicted cracking particles and an acceptable number of wrongly predicted ones. The testing results of this RVE from the two different iterations (see Figure 4-7(b)(d)) are not good. It is seen that many cracking particles (black particles) are not predicted by the ANN model. Only 18 and 23 cracking particles are predicted correctly by the ANN model in the two iterations, respectively. The results are accompanied by some incorrectly predicted cracking particles (orange particles) with scattered distribution in the matrix of the RVE. In the DEM simulation, the cracks propagate and connect in the matrix until failure, however, the crack propagation is not learned well from the training data. Combining the results shown in

Figure 4-6 and Figure 4-7, the training accuracy is quite good, but testing accuracy is still not good. It means the network can learn the information from our training data well, while the networks may not make accurate predictions for unseen data.

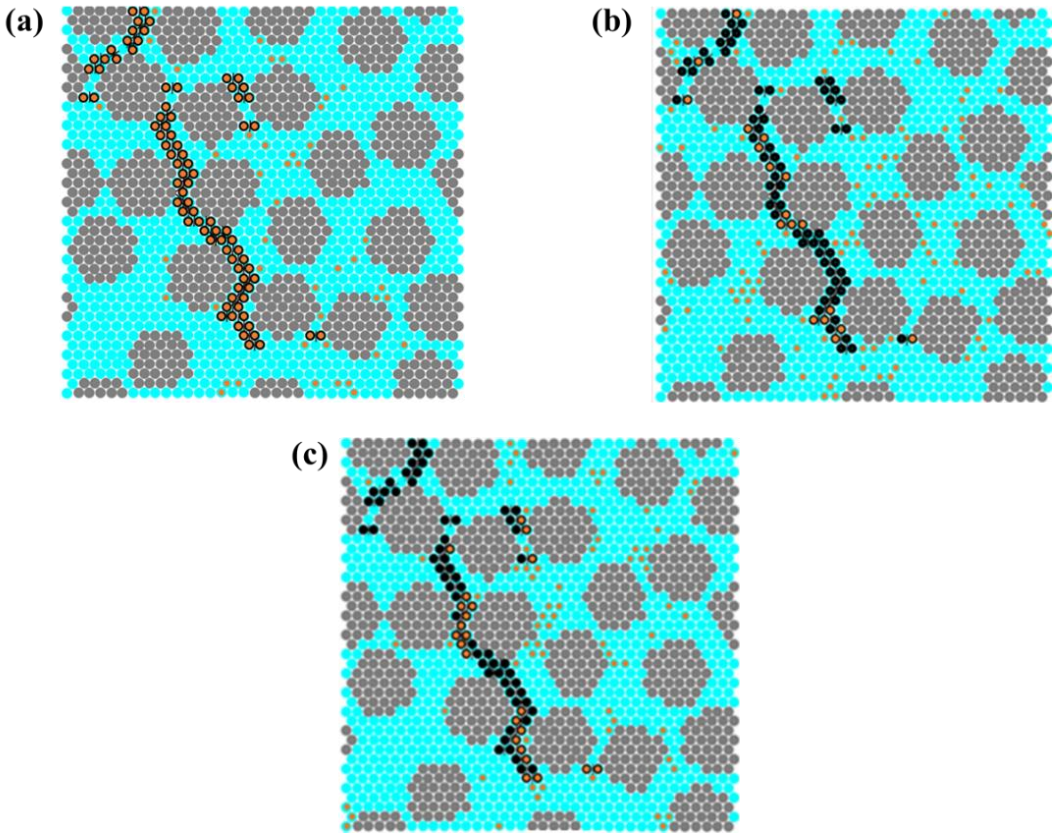

Figure 4-7: (a)Training result and (b)-(c)testing results by the two-layer feedforward ANN model

Dropout is one of the commonly used methods to avoid this problem in the ANN model. It is a regularization method that drops out the nodes of hidden layers in a network [146]. As a result, as shown in Figure 4-8, the structure of the ANN after dropout becomes simpler than that of the original ANN.

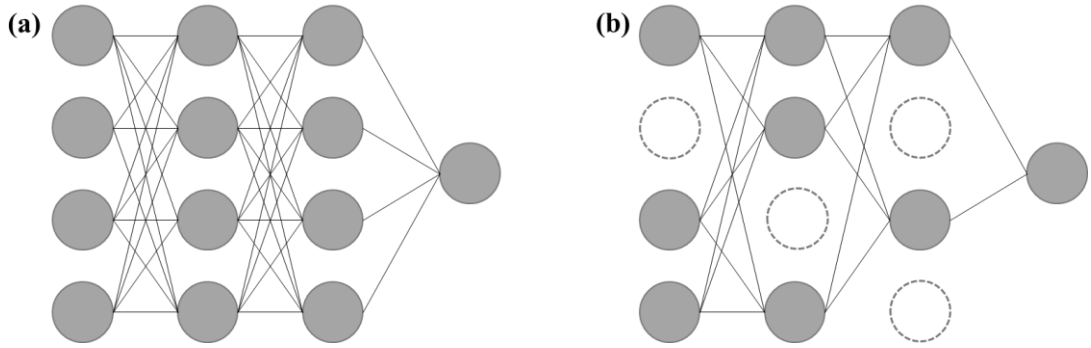

Figure 4-8: (a)Standard Neural Network. (b) Network after Dropout.

Figure 4-9(b) is the ANN prediction result based on the data of 500 DEM simulations after dropout, which shows more cracking particles are predicted correctly by ANN without dropout (see Figure 4-9(a)). Though there are still some wrongly predicted crack particles, the ANN prediction result of the crack path based on the data of 500 DEM simulations with dropout shows improved accuracy compared to those without dropout or based on the same group of data.

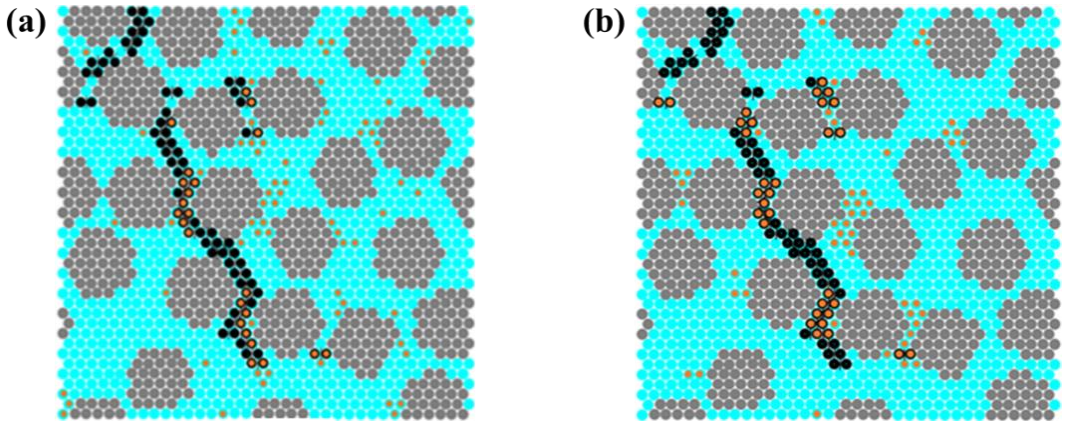

Figure 4-9: (a)Testing result by ANN. (b)Testing result by ANN after dropout.

4.2 An improved predictive model for microscopic cracks

The accuracy of the Gaussian Naïve Bayes classifier and Artificial Neural Networks (ANNs) for predicting whether a crack occurs between two particles is not very good

due to the overfitting problem caused by its complexity and the class imbalance. A new perspective on the problem of predicting cracks is needed. Therefore, an improved DNN predictive model with a new feature selection and structure adjustment based on a larger group of data is developed.

4.2.1. Data generation and pre-processing

The size of the data pool is very important in the ML model. In the improved predictive model for predicting the microscopic cracks, the data set contains 1600 2D RVE samples of $50\ \mu m \times 50\ \mu m$ with a constant fibre volume fraction of 45% and fibre radius of $3.3\ \mu m$. These 1600 RVEs are first simulated using the DEM model. The improved predictive model is to predict the occurrence of cracking. It is a classification problem. Figure 4-10(a) is an RVE with DEM simulated crack path. The RVE is divided into (7×7) subareas. The idea is if there is at least one crack in a subarea of the RVE, the subarea will be classified as having an output of 1. Otherwise, the subarea will be classified as having an output of 0.

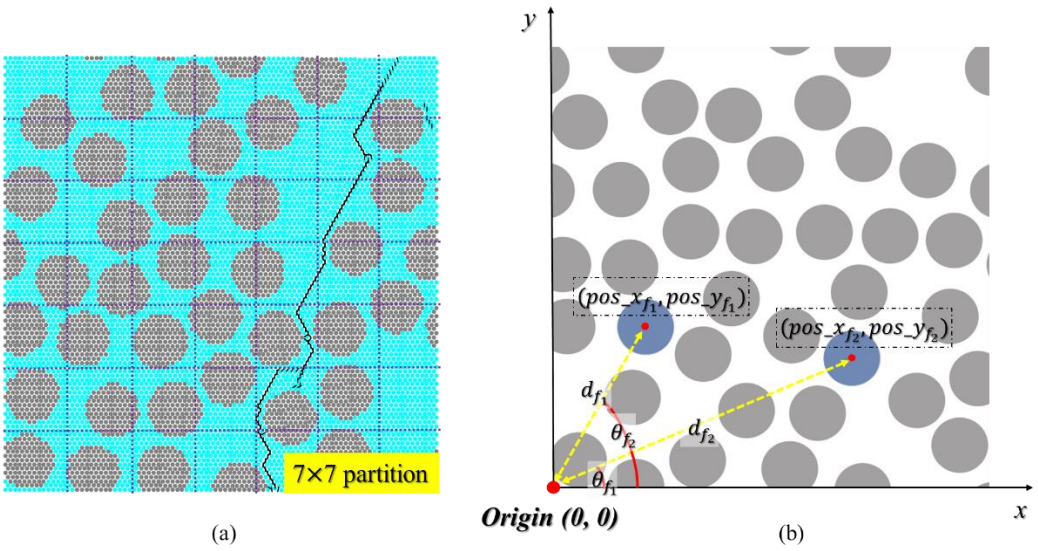

Figure 4-10: Data pre-processing based on the generated RVE. (a) RVE partition. (b). Feature selections

After that, a selection of input features is carried out. The input features for crack prediction contain important geometrical information, i.e., the spatial distribution of fibres in the RVE, which is critical to the potential crack initiation and propagation. The origin or a geometric reference point of the RVE is firstly chosen (see the bottom-left corner in Figure 4-10(b)), such that all the considered features can be related to the origin to define the geometry of the RVE uniquely. Given the positions of the randomly distributed fibres, for instance, $(pos\_x_{f_1},\ pos\_y_{f_1})$ and $(pos\_x_{f_2},\ pos\_y_{f_2})$. As shown in Figure 4-10(b), two types of features, namely the distance to the origin (denoted d_{f_1}) and the corresponding angle with the $x-$ axis (denoted θ_{f_i}), are used to represent the relative spatial positions of the randomly distributed fibres in the RVE. And the distances from each fibre to the origin are set in order of the nearest to the farthest. The distances and angles are computed as follows:

$$d_{f_i} = \sqrt{(pos\_x_{f_i} - 0)^2 + (pos\_y_{f_i} - 0)^2} \tag{4-11}$$

$$\theta_{f_i} = arcsin\ (\frac{pos\_y_{f_i}}{d_{f_i}}) \tag{4-12}$$

where $pos\_x_{f_i}$ and $pos\_y_{f_i}$ are the $x-$ and $y-$ coordinates of the centre of fibre i. It is worth stressing that there are at most 53 randomly distributed fibres in the generated RVEs with a fibre volume fraction of 45% and a fibre radius of 3.3 μm. If the number of fibres is less than 53 due to the random fibre distribution, it will be assumed that fibres are replenished to the corner opposite the origin. In this way, the distances of fibres to the origin are the length of the diagonal of the RVE plus the radius of the fibre, and its corresponding angle is 45°. Therefore, the numbers of the input data in each generated RVE are the same for the predictive model.

Tests using different divisions are then performed, from which a reasonably accurate prediction can be achieved. As shown in Figure 4-11 and Figure 4-12, the DNN

predictions of cracks in RVEs under three different segmentation sizes are compared. The short black lines in Figure 4-11(a)-(c) and Figure 4-12(a)-(c) are the DEM simulated cracks. The yellow areas in Figure 4-11(a)-(c) and Figure 4-12(a)-(c) are the cracked subareas predicted by the DNN. The tables in Figure 4-11(d)-(f) and Figure 4-12(d)-(f) are also the DNN predicted results represented by the '0' and '1' labels. The red '0' or '1' means wrongly predicted results by the DNN model, and the black '0' or '1' represents the correct results predicted by the DNN model. All the RVEs used for the prediction of the crack patterns are with a dimension of $50\ \mu m \times 50\ \mu m$ with a constant fibre volume fraction of 45% and a fibre radius of 3.3 μm. For the RVEs with 25 subareas (5 × 5), as shown in Figure 4-11(a) and Figure 4-12(a), all the cracked areas (the yellow areas) in the two RVEs are predicted correctly by the trained DNN model. However, there are at most three fibres per subarea, which results in a relatively rough prediction of the cracked areas. On the other hand, as shown in Figure 4-11(c) and Figure 4-12(c), the accuracy of the crack prediction for the RVE with 100 subareas (10 × 10) is less satisfactory. Due to the sizes of the subarea and fibre, some of the subareas in RVEs with 100 subareas (10 × 10) are covered by incomplete fibres (see Figure 4-11(c) and Figure 4-12(c)). However, there is no damage in fibres. It can be concluded that a finer division does not improve the effectiveness and accuracy of the prediction. Considering achieving a reasonably accurate prediction without demanding excessive computational cost, (7 × 7) subareas (see Figure 4-10(a)) are used in the DNN prediction. Therefore, in the classification model, 53 pairs of 2-dimensional feature vectors are identified as the 53 2D input features in the input layer and the output layer there are 49 outputs in a vector, which are either 1 or 0.

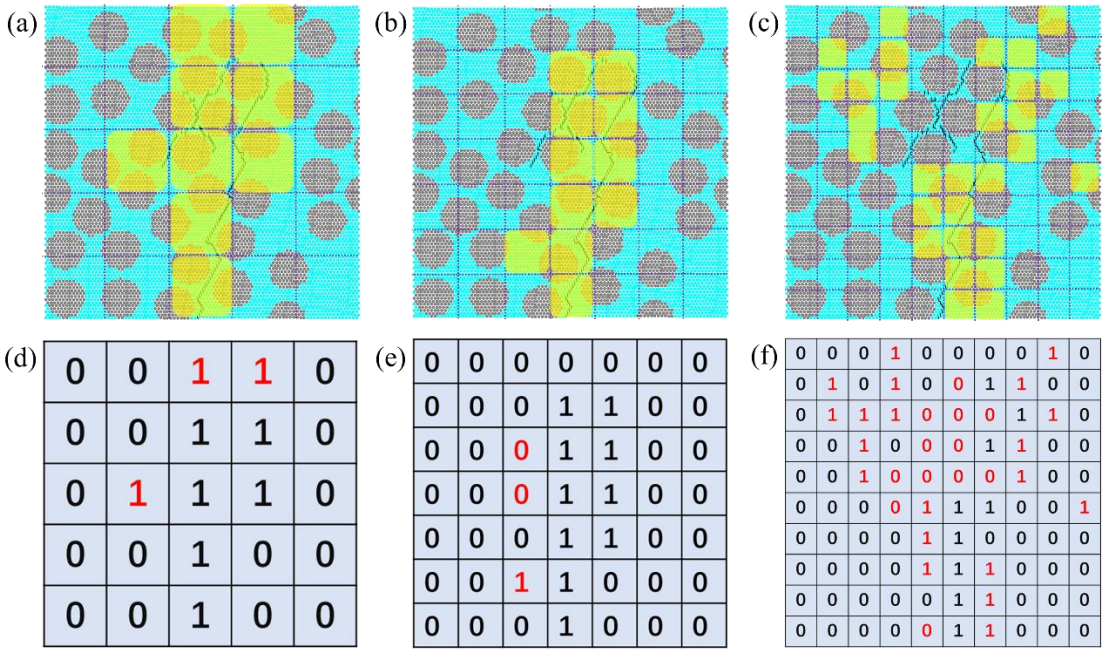

Figure 4-11: Comparison of DNN predictions of cracks in the first RVE with different segmentation sizes. (a)(d)RVE with 25 subareas (5 × 5). (b)(e)RVE with 49 subareas (7 × 7). (c)(f)RVE with 100 subareas (10 × 10).

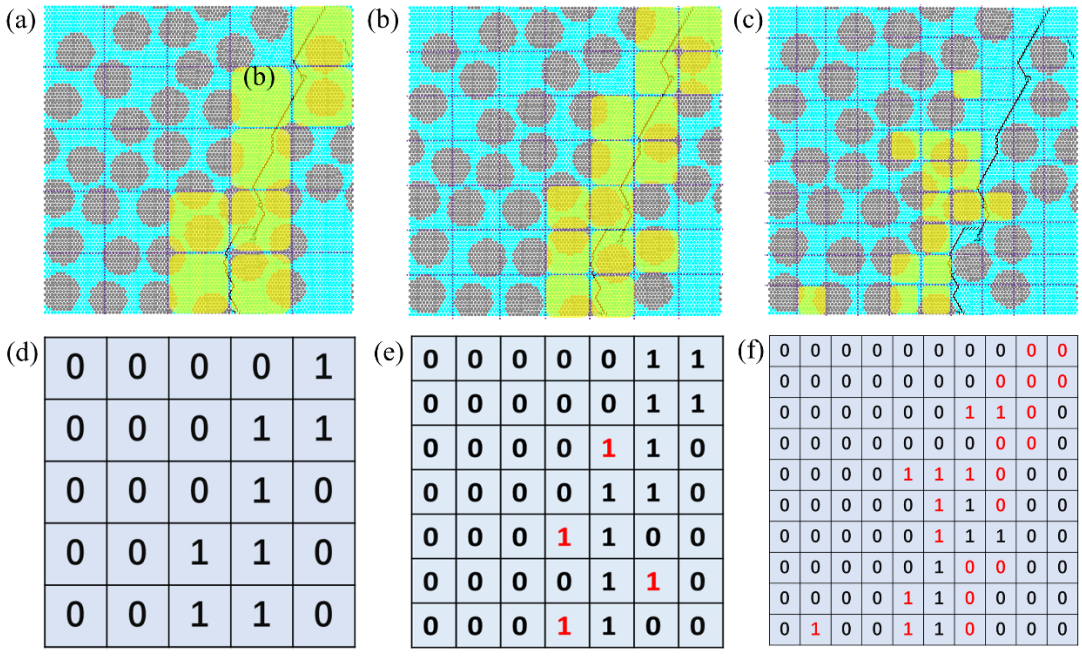

Figure 4-12: Comparison of DNN predictions of cracks in the second RVE with different segmentation sizes. (a)(d)RVE with 25 subareas (5 × 5). (b)(e)RVE with 49 subareas (7 × 7). (c)(f)RVE with 100 subareas (10 × 10).

After selecting the features, data pre-processing is carried out. 80% of the data (extracted from 1280 DEM model simulations) are used as training data for the DNN predictive model. The rest 20% (extracted from 320 simulations) are used as testing data. Additionally, to ensure that all the features are of the same scale, Min-max normalization is used to rescale the features in the training and testing sets independently.

4.2.2. Configuration of the DNN predictive model for crack path

In the previous ML model, a feedforward two-layer network is constructed for predicting the cracking particles in the RVE. It is found that the performance of the network is not very good. More hidden layers, as well as more neurons in the network, are considered. A DNN classification model with back-propagation is constructed (see Figure 4-13). The 53 pairs of 2D feature vectors discussed in the last sub-section are in the input layer and are to be trained to predict cracking as multi-outputs in the output layer. The network shown in Figure 4-13 is found to have a better performance after doing a set of trials using the models with different numbers of hidden layers and different numbers of neurons. In the DNN model, the number of hidden layer is four. In each layer, there are 530 neurons. The activation function used from the input layer to the first hidden layer and between every two hidden layers is ‘ReLU’. The activation function used between the last hidden layer and the output is ‘Sigmoid’. The generated DNN classification model is implemented by using Keras functions in the TensorFlow package through Python [143, 144].

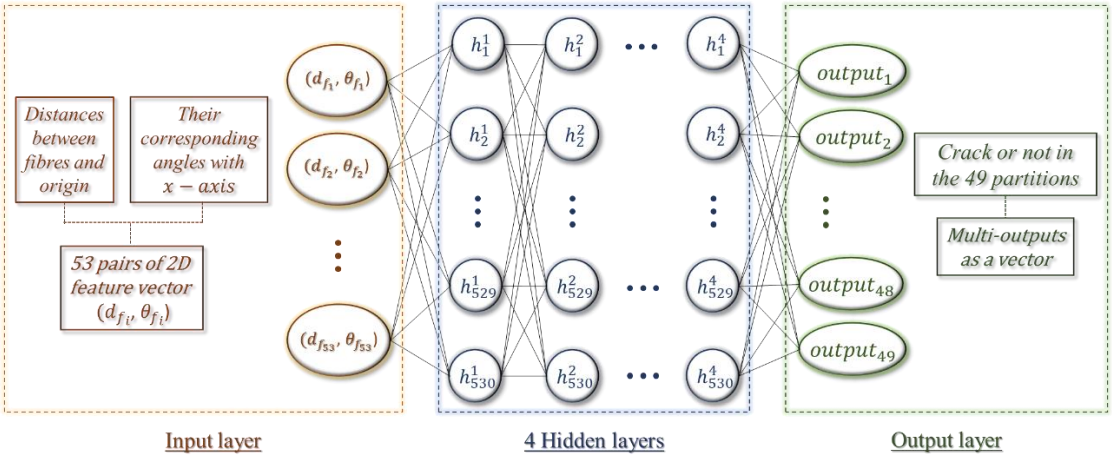

Figure 4-13: A multi-layer DNN model for the predictions of crack path

4.2.3. Results of the improved predictive model for predicting cracks

To demonstrate the accuracy of the DNN model, we divide the composite material into a number of subareas and study the likelihood of crack occurrence within each of the subareas. Both the validated DEM model and the trained DNN model are used to predict the occurrence of cracks in 1600 samples with the same material composition but randomly distributed fibres. For each of the subareas, the number of times it is predicted to crack by both models is counted respectively. The respective total occurrence of cracking of each subarea is divided then by the total number of the samples to give the predicted probability of cracking of each of the subareas (locations) of the material for both models. The crack probabilities at each subarea obtained from the DEM model (denoted $\boldsymbol{Prob}_{DEM\_crack_i}$) and DNN predictions (denoted $\boldsymbol{Prob}_{DNN\_crack_i}$) are therefore obtained by the following expressions:

$$\boldsymbol{Prob}_{DEM\_crack_i} = \frac{the\ number\ of\ times\ the\ subarea\ i\ has\ an\ output\ of\ 1\ by\ DEM}{1280} \quad (4\text{-}13)$$

$$\boldsymbol{Prob}_{DNN\_crack_i} = \frac{the\ number\ of\ times\ the\ subarea\ i\ has\ an\ output\ of\ 1\ by\ DNN}{320} \quad (4\text{-}14)$$

where $i\ (= 1, 2, \ldots, 49)$ denotes number of the subarea.

Figure 4-14 compares the above-defined crack probabilities from the DEM results and the DNN predictions. The probabilities of cracking at different locations (subareas) obtained from the DNN predictions are close to those from the DEM model.

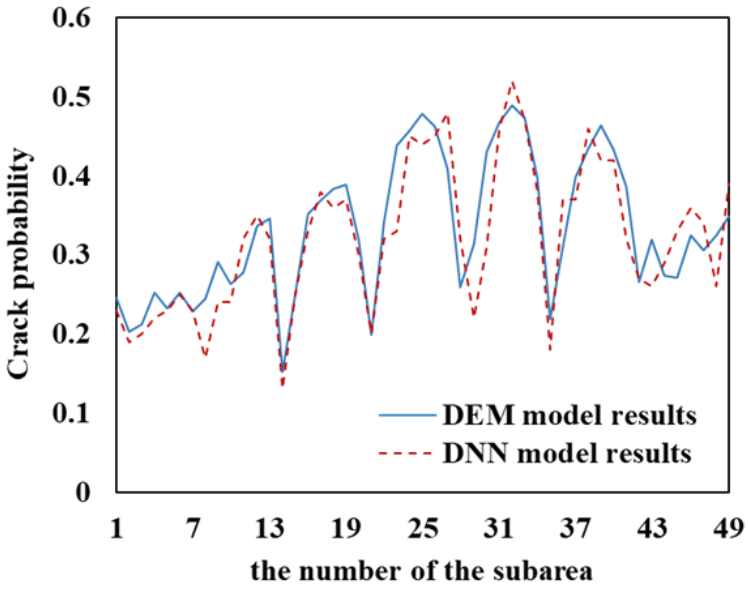

Figure 4-14: The crack probabilities based on DEM model results and DNN prediction results.

In addition, the density of cracking of the 1600 RVE-based DEM simulations is calculated and compared with the density of cracking obtained from the DNN predictions. The density of cracking is computed as the total number of cracked subareas of the RVE samples divided by the total number of subareas of the RVE samples, which describes the extent of cracking coverage in each RVE sample. The densities of cracking based on the 1600 DEM and DNN simulations are, respectively, 0.3325 and 0.3288, which shows a very high consistency between the two results. It can

be concluded that the trained DNN model can satisfactorily predict the locations of cracking and the overall crack density of the material.

Based on the ‘0’ and ‘1’ classifications, three representative DNN prediction results of cracking are shown in Figure 4-15, Figure 4-16 and Figure 4-17, respectively. Figure 4-15(a) shows an RVE generated by DEM with random fibre distribution. The cracks, marked by A and B, are the initial cracks predicted by the DEM, both of which are located at the centre of the RVE. The damage in the RVE starts at the stress of 56 MPa and these initial cracks show an early stage of failure (at the stress of 61 MPa). It can be seen that the initial cracks appear at the locations where fibres are close to each other. This confirms that the locations of initial cracks are closely related to the overall and local properties of fibre distributions of the RVE. To be specific, it is usually deemed that these areas contain a high fibre and matrix stiffness ratio, which results in significant stress concentration [9]. As the tensile loading velocity of 5 mm/s is continuously applied, the initial cracks grow inside the RVE. Figure 4-15(b) shows the DEM simulation result of crack growth within the RVE when the stress is about 70% of the tensile strength. Figure 4-15(b), crack propagation in the matrix starts to appear. There are four short cracks in the matrix at the upper middle part of the RVE and one long crack through the matrix between five pairs of relatively close fibres, which cause the final failure of the RVE. The yellow areas in Figure 4-15(c) are the cracked subareas predicted by the DNN, which are compared with the DEM simulations in Figure 4-15(d). It can be found that almost all the cracked areas are predicted correctly by the trained DNN model. There are 3 mispredicted crack areas, as shown more clearly by the DNN outputs classifications in Figure 4-15(e-f). The two red ‘0’ represent that these two cracked subareas are not correctly predicted by the DNN. The red ‘1’ area has cracked in the DNN prediction, while has not according to the DEM simulation.

In Figure 4-16(a), the damage in the RVE starts at the stress of 38 MPa from the simulation and the initial cracks are generated at the stress of 42.5 MPa. Similar to the initial cracks of the RVE in Figure 4-15(a), the initial cracks of the second RVE also occur at the region where the inter-fibre distance is small. However, unlike the way of the long crack propagation in the RVE in Figure 4-15(b), the cracks in Figure 4-16(b) extend upward through the region where the fibres are located relatively sparsely. In Figure 4-16(c), the cracks predicted by the DNN model show a similar pattern. The comparison in Figure 4-16(d) demonstrates that the DNN has satisfactorily predicted crack propagation. Again, the output classifications of the DNN model are shown in Figure 4-16(e-f). Four areas are wrongly predicted as cracked. However, these four subareas are all close to the correctly predicted crack areas, which is reasonable because the DNN model considers the probability of the crack in the vicinity of an existing crack to be high.

Figure 4-17(a) shows the third RVE with several isolated cracks at the early stage of failure (at the stress of 56.5 MPa) from the DEM simulation. Compared to the crack paths of the first two RVEs, the damage of the third one consists of several short and medium-length cracks, as shown in Figure 4-17(b). The short cracks occur between two adjacent fibres first and then propagate in the matrix. Then, some of the initial cracks connect with each other. From Figure 4-17(c-f), it can be observed that the accuracy of the crack prediction by the DNN is less satisfactory compared to that of the first and second RVEs. The purpose of selecting this RVE is to demonstrate a typical error of the DNN prediction. However, as shown in Figure 4-17(d), most of the cracks on the right-hand side of the RVE are predicted correctly, which cause the ultimate failure of the RVE according to the DEM simulation. In addition, the subarea having one short crack, labelled by C in Figure 4-17(d), is not predicted as a crack area by the DNN. Instead,

three subareas, labelled by X in Figure 4-17(d), with a relatively dense fibre distribution are identified as cracked. Crack C is short and does not eventually propagate or merge with a longer one leading to the ultimate failure (see Figure 4-17(b) and (d)). Thus, it appears that when the current DNN model is used to predict short and isolated cracks, it may not have the same accuracy as it is used to predict growing cracks, as shown in the previous two RVEs. Nevertheless, it can be concluded that the DNN model can successfully predict most of the cracks and the major crack evolution with full consideration of fibre random distribution.

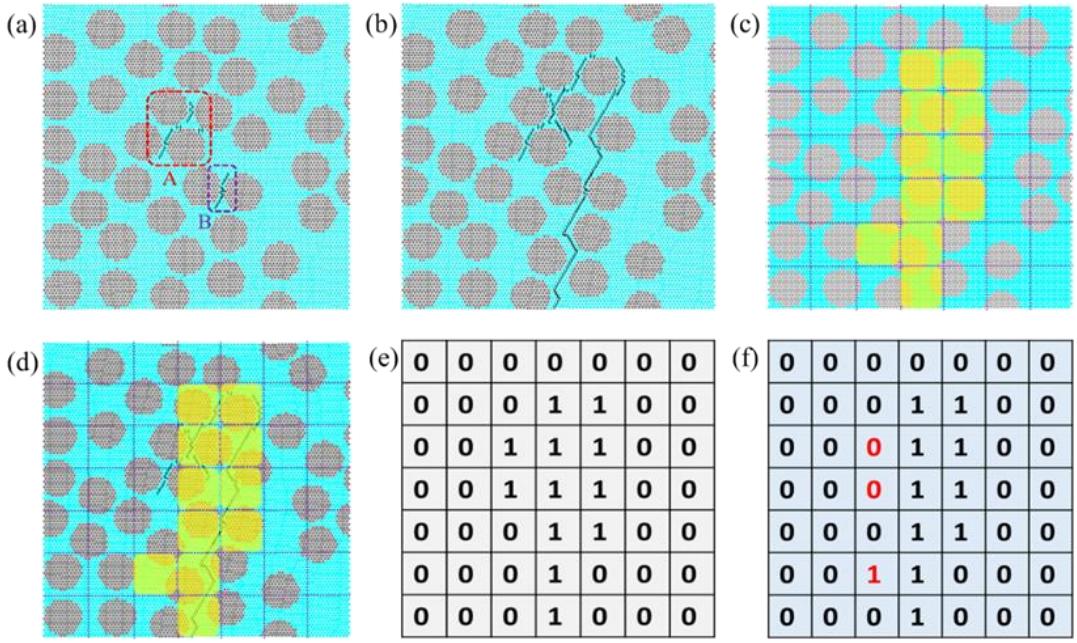

Figure 4-15: (a) Initial cracks in the first RVE simulated by DEM model. (b) DEM simulated crack path. (c) DNN prediction of crack path. (d) Result combined with DEM simulated cracks and DNN predicted crack subareas. (e) Table of results of the DEM simulation. (f) Table of results of the DNN prediction.

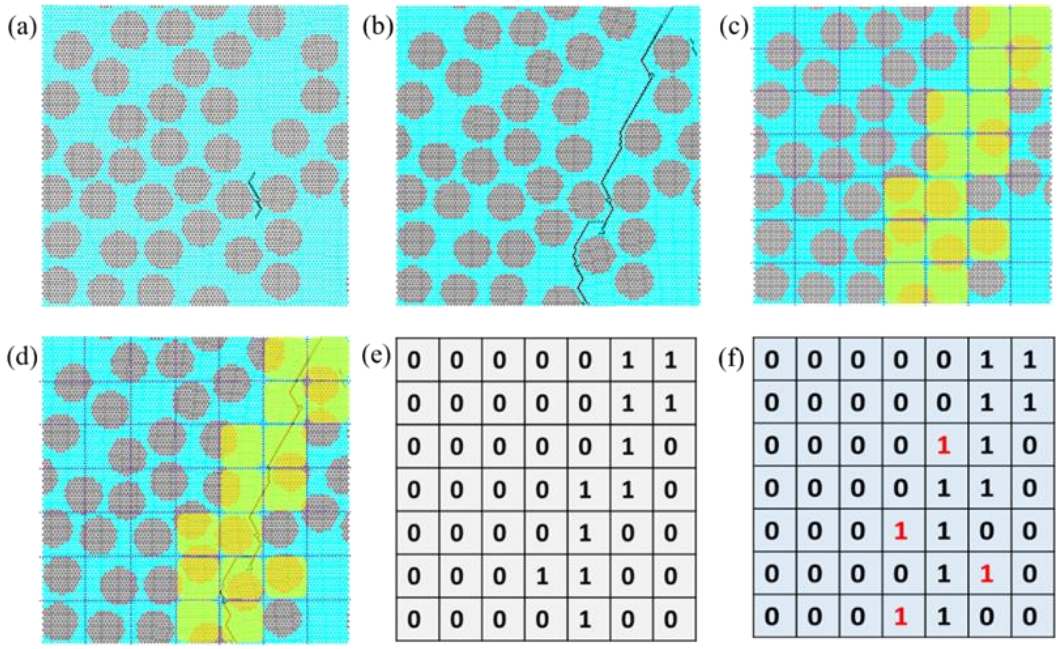

Figure 4-16: (a) Initial cracks in the first RVE simulated by DEM model. (b) DEM simulated crack path. (c) DNN prediction of crack path. (d) Result combined with DEM simulated cracks and DNN predicted crack subareas. (e) Table of results of the DEM simulation. (f) Table of results of the DNN prediction.

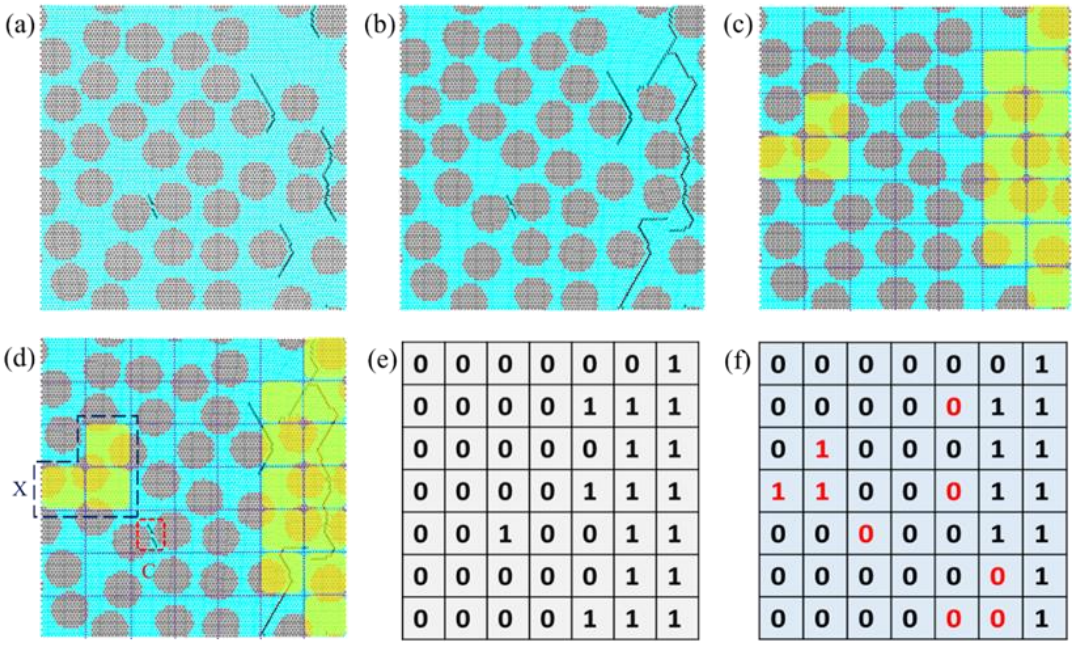

Figure 4-17: (a) Initial cracks in the first RVE simulated by DEM model. (b) DEM simulated crack path. (c) DNN prediction of crack path. (d) Result combined with DEM simulated cracks and DNN predicted crack subareas. (e) Table of results of the DEM simulation. (f) Table of results of the DNN prediction.

4.3 DNN predictive models for the initial cracks

In order to obtain the position of initial cracks more efficiently, lastly, in the chapter, two DNN models are developed for predicting the crack initiation in the UD FRP lamina. The models will train a set of suitable and representative features obtained from the DEM simulations and then predict the first and second cracks in the RVE subject to the loading of transverse tension in order.

4.3.1. Development of the DNN for the first crack

4.3.1.1. Data generation and pre-processing

The data set for predicting the first crack contains 500 RVE samples of UD FRP lamina with dimension $40\ \mu m\ \times\ 40\ \mu m$ consisting of 35% randomly distributed fibres with a uniform fibre radius of 3μm (see Figure 4-18). As shown in Figure 4-18, these RVEs with random fibre distribution are not generated based on the periodic condition. Based on the above setting of the RVE, the number of fibres is fixed as 20. It can make the number of features for each data point consistent.

It is known that the contact bond will break if the contact force exceeds the contact strength in the DEM simulation. Thus, the idea of the deep learning model for predicting the initial crack is to regress the contact force of each contact in the RVE at the time step just before the first crack occurs so that the fracture of the contact bond can be determined from the regressed contact forces. As it is impossible to calculate the contact force at the exact time of cracking, the contact bond force at the time step immediately before the initial cracking is taken approximately as the critical force of cracking. In this way, the contact bond with the highest contact force is regarded as the initial crack in the RVE.

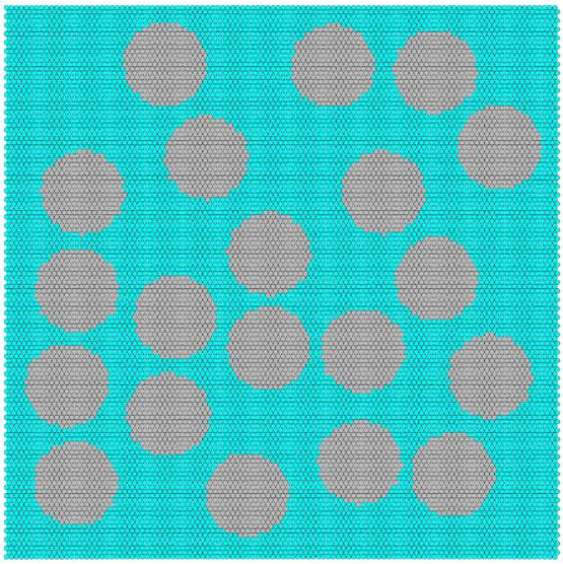

Figure 4-18: RVE generated for predicting the crack initiation.

There are around 41000 contact bonds in each RVE sample, including fibre-fibre contacts, matrix-matrix contacts, and fibre-matrix interface contacts. The contact force of each contact bond at the time just before the initial crack of all the 500 RVE samples can be recorded by the DEM software 'PFC 2D'. Extracting all matrix-matrix contacts is done first, as it is assumed that there is no damage in the fibre and fibre-matrix interface during the DEM simulation. Then based on the hexagonally packed particles in the RVE and the transverse tension in the perpendicular direction applied on the lamina, the initial crack occurs only in the 0-degree contact bond. The DEM simulation data includes each RVE sample consisting of the positions of approximately 8500 matrix-matrix contact bonds with 0 degree. In the regression model, every contact bond is regarded as a data point. As a result, the deep learning model will train and test 4250000 data which are the 42500000 (8500×500) matrix-matrix contact bonds of the 500 RVEs.

The features for the regression problem are the positions of the matrix contact bonds (denoted (pos_y_c, pos_y_c)), the distances between each contact bond to the 20 fibres

(denoted d_{cf_i}) and their corresponding angles (denoted θ_{cf_i}), which are computed by Python codes as follows:

$$d_{cf_i} = \sqrt{(pos\_x_c - pos\_x_{f_i})^2 + (pos\_y_c - pos\_y_{f_i})^2} \quad (i = 1, 2, \ldots, 20) \tag{4-15}$$

$$\theta_{cf_i} = arcsin\left(\frac{pos\_y_{f_i}}{d_{cf_i}}\right) \tag{4-16}$$

where pos_x_c , pos_y_c and $pos\_x_{f_i}$, $pos\_y_{f_i}$ are the $x-$ and $y-$ coordinates of the centre of matrix-matrix contact bond with 0 degree and fibre *i*. Taking a contact bond of the matrix as a data point, the position of the contact bond of the matrix gives the most direct information on the distribution of the contact bond of the matrix. The distance and the corresponding angle between the matrix bond and each of the fibres represent the spatial position of the matrix bond relative to the randomly distributed fibre in the RVE. The distances from the matrix bond to the 20 fibres are set in order of the nearest to the farthest, which can obtain the distribution of fibres around this matrix bond. In this prediction problem, the number of fibres in each RVE is identical to 20, which makes the number of features for each data point the same as 21. Therefore, for one contact bond in the RVE, there are 21 pairs of 2D feature vectors, including the positions of the matrix contact bond, 20 pairs of distance and the angle to the fibre.

For the data set partition, 80% of the data (extracted from 400 DEM model simulations) are used as training data for the DNN predictive model. The rest 20% of the data (extracted from 100 simulations) are used as testing data. Finally, to ensure that all the features are of the same scale, Min-max normalization is used to rescale the features in the training and testing sets independently.

4.3.1.2. Configuration of the DNN model for the initial crack

After the data pre-processing, the DNN regression model with back-propagation is constructed, as shown in Figure 4-19. In the input layer, there are 21 pairs of 2D features including the position of the contact bond of the matrix, the distances between the matrix contact bond to the fibre and its corresponding angle. The contact force of the contact bond is the single output in the output layer. There are four hidden layers in the DNN model with the same neuron number of 420 in each layer. The activation function used from the input layer to the first hidden layer and between every two hidden layers is 'ReLU'. The activation function used between the last hidden layer and the output is 'Sigmoid'. The generated DNN classification model is also implemented using Keras functions in the TensorFlow package through Python.

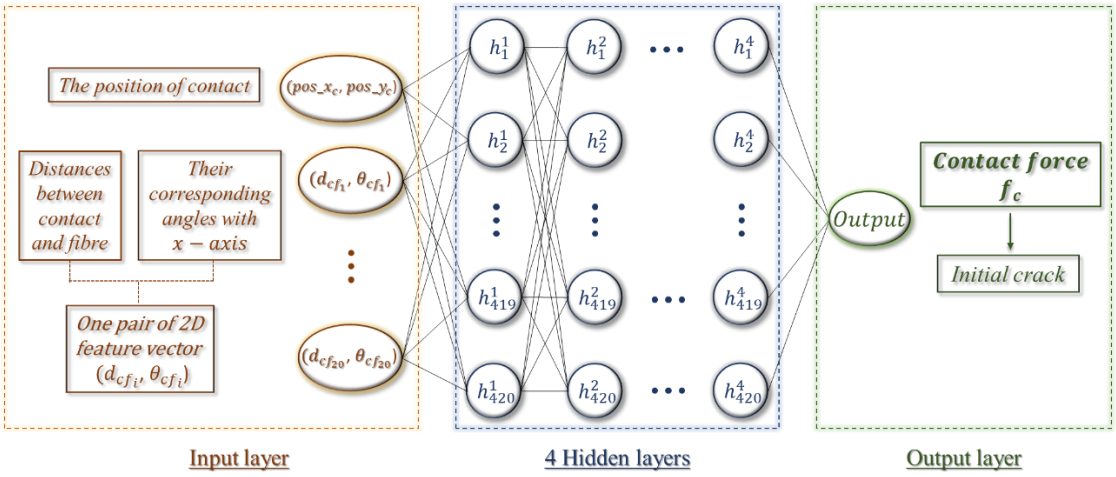

Figure 4-19: A multi-layer DNN model for the prediction of contact force.

4.3.2. Results of the DNN model for the initial crack

The DNN model for predicting the initial crack in RVEs trains the amount of data extracted from 400 DEM simulations and tests the data from 100 DEM simulations. There are two levels of evaluation criterions for the analysis of the prediction

performance. The accuracy of the model for predicting the initial crack is shown in Table 4-1. The first criterion is, if the predicted initial crack (by DNN) is close to the one determined by the DEM model within a distance smaller or equal to the diameter of the ball (*3.64e-4mm*), the predicted crack will be regarded as an accurate result. According to this criterion, the initial cracks in the 65 RVE samples can be predicted successfully, thus, the accuracy is 65% (65/100). It means that the DNN model can find out the highest contact force of the contact bond among 8500 contact bonds successfully.

Two examples of this criterion are shown in Figure 4-20. Figure 4-20(a) compares the DNN and DEM results of the contact forces. The black triangle at the bottom-left in Figure 4-20(a) is the predicted highest contact force, which is -32.73N. The DEM simulated contact force of this contact bond is also the highest and is -36.75N. The position of this contact bond in the RVE is plotted as the black triangle in Figure 4-20(b), which shows that the DNN predicted initial crack is at exactly the same position as that of the DEM simulated initial crack. It is found that the initial crack occurs in the place between two very closed fibres. The input features trained into the DNN model are designed to tell the model that an initial crack often occurs in the matrix where the fibres are very close to each other. The DNN model can predict this initial crack accurately, which reflects that the DNN model captures the relation between input features and the output well. The second example of this scenario is shown in Figure 4-20(c-d). The black triangle represents the highest contact force of the contact bond simulated by the DEM model, as shown in Figure 4-20(c), which is --36.56N. The DNN model predicts the contact force of this contact bond to be the second highest one, with a value of -32.67N. The position of this DEM simulated cracking bond is plotted as the black triangle in Figure 4-20(d). The red triangle plotted in Figure 4-20(c) is the highest contact force of the contact bond predicted by the DNN model, which is -33.71N. The

position of this contact bond is marked as a red triangle shown in Figure 4-20(d), right around the DEM simulated initial crack.

The DNN prediction can be treated as acceptable if the initial crack simulated by the DEM model is among the first five cracks predicted by the DNN model ordered by their contact forces. This is the second criterion. Based on the 2nd criterion, the initial cracks in the 92 RVEs can be successfully predicted, thus, the accuracy of the DNN prediction increases to 92 %. Figure 4-21 shows two examples of this criterion. For instance (Figure 4-21(a-b)), the initial crack predicted by the DEM model is plotted by a black triangle in the RVE. The position (marked as a red triangle) with the third-highest contact force from the DNN prediction is right next to the DEM simulated one. Thus, by the 2nd criterion, it is acceptable as it is among the first five possible cracks. Figure 4-21(c-d) shows another example of the second criterion. The initial crack predicted by the DEM model is marked as the black triangle in Figure 4-21(d), which is the position with the third-highest contact force predicted by DNN. The first crack predicted by the DNN model is plotted as a red triangle in the RVE (see Figure 4-21(d)). In this example, the DNN model regards the initial crack bond as an initial crack bond with the third highest risk.

Table 4-1: DNN prediction results for the initial crack.

Criterion	Result	Accuracy
Criterion 1: The DNN predicted crack is around the DEM simulated initial crack.	65	65%
Criterion 2: The contact bond around the DEM simulated initial crack is in the list of DNN-predicted cracks with the top five highest risks.	92	92%

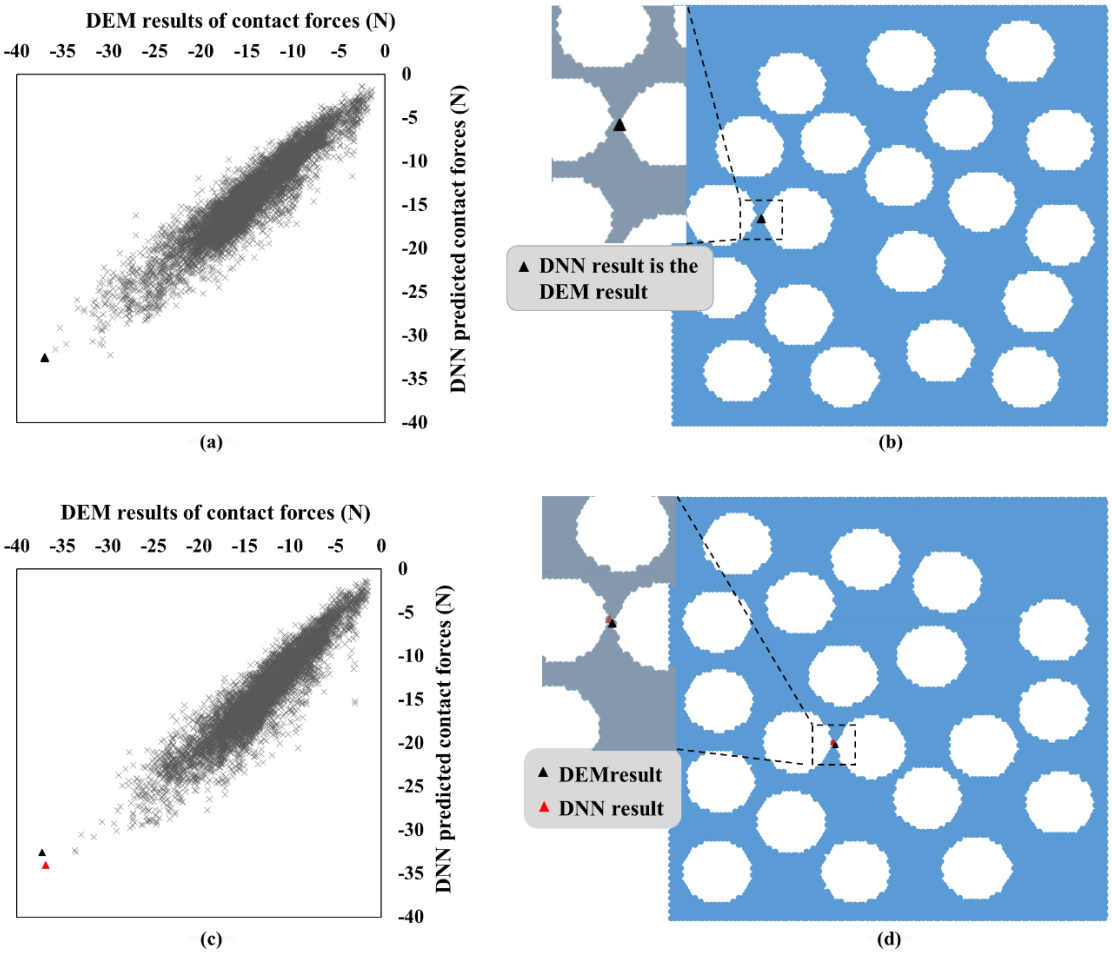

Figure 4-20: Two examples of Criterion 1. (a)(c) DNN regression results of contact forces. (b)(d) The initial crack in the RVE.

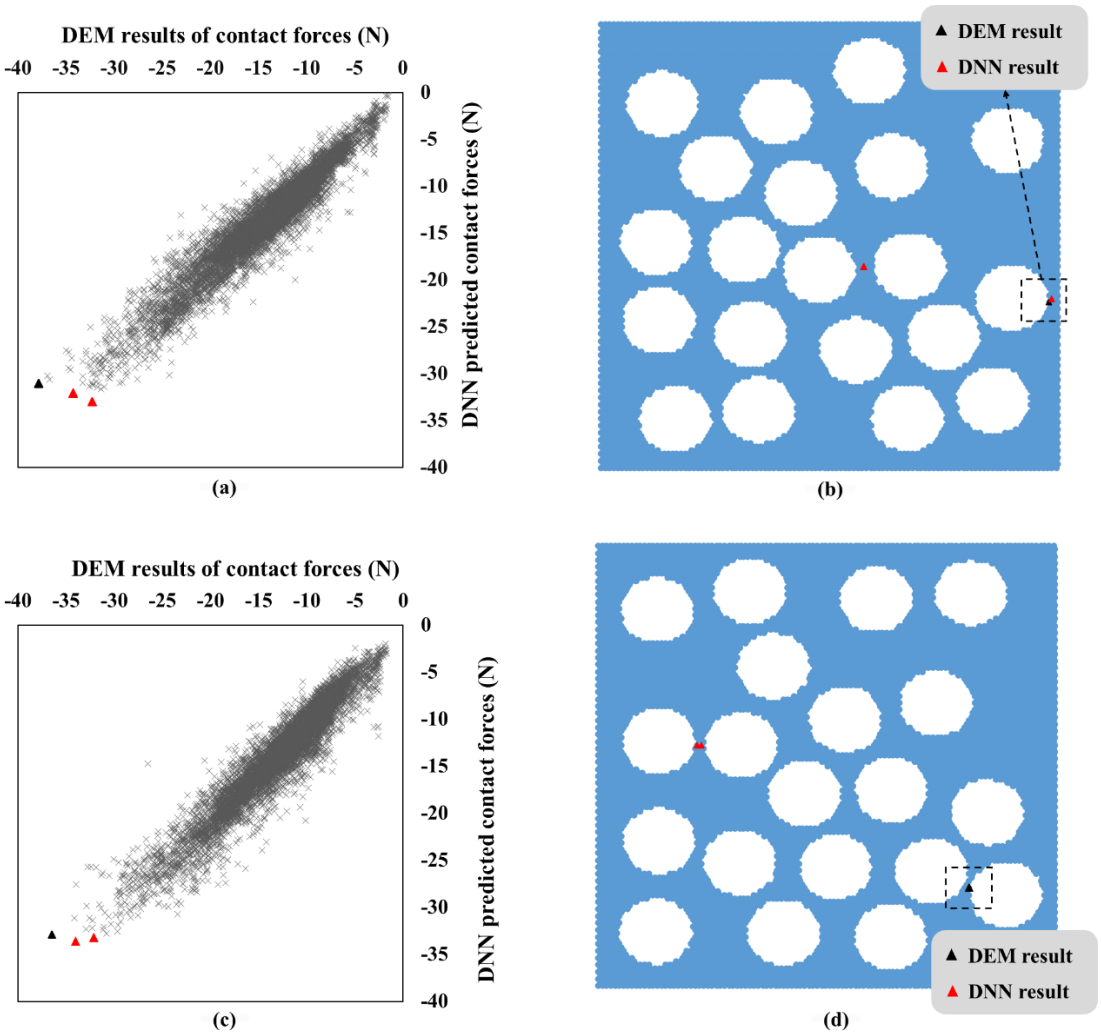

Figure 4-21: Two examples of Criterion 2. (a)(c) DNN regression results of contact forces. (b)(d) The initial crack in the RVE.

4.3.3. Development of the DNN for the second crack

4.3.3.1. Data generation and feature selection

After predicting the initial crack in the RVE, the next step is to predict the second crack based on the prediction results of the initial crack. The data of DEM simulations used in the predictive model for the second crack does not need to be regenerated. However, more features are added to the predictive model. The new considered features are related to the initial crack. If a bond breaks, its contact force becomes zero. In the

DEM simulation, the contact force of the bond next to the broken bond will be affected. Thus, the information about the initial crack will play an essential role in predicting the second crack. As shown in Figure 4-22, the distance from the initial crack to the matrix contact bond and its corresponding angle is added to reflect the information of the initial crack.

Therefore, the features of each matrix bond include the positions of matrix contact bonds (denoted ($pos\_x_c,\ pos\_y_c$)), the distances between each contact bond to the 20 fibres (denoted d_{cf_i}) and their corresponding angles (denoted θ_{cf_i}), the distances between each contact bond to the initial crack (denoted d_{cCra_1}) and its corresponding angles (denoted θ_{cCra_1}). These are calculated as:

$$d_{cf_i} = \sqrt{(pos\_x_c - pos\_x_{f_i})^2 + (pos\_x_c - pos\_y_{f_i})^2} \quad (i = 1, 2, \ldots, 20) \tag{4-17}$$

$$\theta_{cf_i} = arcsin\left(\frac{pos\_y_{f_i}}{d_{cf_i}}\right) \tag{4-18}$$

$$d_{cCra_1} = \sqrt{(pos\_x_c - pos\_x_{Cra_1})^2 + (pos\_y_c - pos\_y_{Cra_1})^2} \tag{4-19}$$

$$\theta_{cCra_1} = arcsin\left(\frac{pos\_y_{Cra_1}}{d_{cCra_1}}\right) \tag{4-20}$$

where pos_x_c, pos_y_c, $pos\_x_{f_i}$, $pos\_y_{f_i}$, (where i = 1, 2, …, 20) and $pos\_x_{Cra_1}$, $pos\_y_{Cra_1}$ are the $x-$ and $y-$ coordinates of the centres of the matrix-matrix contact bond with 0 degree, fibre *i* and the initial crack. As mentioned above, there are 22 pairs of 2D input features in the predictive model.

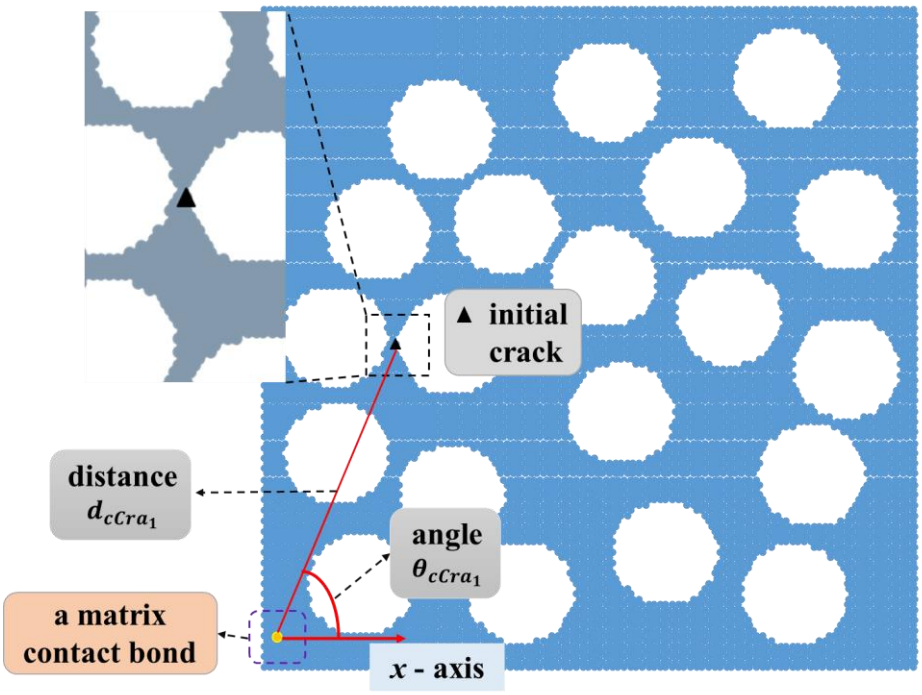

Figure 4-22: New features related to the initial crack.

4.3.3.2. The division of the training set and testing set

As a follow-up to the initial crack prediction, the training data used in the training process of the predictive model for the initial crack (80% of the data: 400 simulations) are also used as training data in the DNN predictive model for the second crack. The positions of initial cracks in the 400 RVEs are extracted in advance to calculate the features related to the initial crack.

The testing process is slightly more complicated. In the prediction for the initial crack, 20% of the data (extracted from 100 simulations) are used as testing. Two evaluation criterions are considered for the prediction analysis of the initial crack. One is that the DNN predicted crack is around the DEM simulated initial crack. The result is that 65 of the initial cracks in RVEs are accurately predicted. The other one is that the contact bond around the DEM simulated initial crack is in the list of DNN-predicted

cracks with the top five highest risks. According to this criterion, the initial cracks in 92 RVEs (including the 65 based on the first criterion) are predicted correctly. The rest wrongly predicted 8 RVEs in the 100 RVEs will not be used as the testing data for predicting the second crack.

Having the prediction results of initial cracks in the 92 RVEs, the detailed steps for computing the features in the testing set are as follows:

- Finding the top five largest contact forces of contact bonds in the predicted results
- Finding the contact bonds corresponding to these five forces and determining their positions
- Calculating the distances d_{cCra_1} between each contact bond to the predicted contact bonds and its corresponding angles θ_{cCra_1}

All these steps are implemented in Python. As a result, there are five sets of 22 pairs of 2D input features in each of these 92 RVEs. The 92 RVEs will be tested five times to look for their second cracks correctly. In addition, all the data, including the training data and the five different sets of testing data, are normalized using Min-max normalization.

4.3.3.3. Configuration of the DNN model for the second crack

The configuration of the DNN regression model for predicting the second crack is quite similar to the one used for the first crack. The difference is in the input layer, i.e., there are 22 pairs of 2D features, including the position of the contact bond of the matrix, the distances between the matrix contact bond to the fibre and its corresponding angle, and the distances between each contact bond to the initial crack and its corresponding

angles. The contact force of the contact bond is the single output in the output layer. There are four hidden layers in the DNN model with the same neuron number of 660 in each layer. The activation functions in the DNN model for predicting the second crack are the same as those of the first crack.

4.3.4. Results of the DNN model for the second crack

The DNN model for predicting the second crack in RVEs with random fibre distribution trains the amount of data extracted from 400 DEM simulations. The model then tests the data from 92 of 100 DEM simulations five times with five different sets of input features. The predictive model aims to determine the second crack once a position of the initial crack is given. The evaluation criterion in this model is whether the DNN-predicted crack is around the DEM simulated second crack. According to this criterion, the second cracks in 65 RVEs are predicted successfully by the DNN model. Thus, the accuracy is $92\% * 65\% \approx 60\%$.

Four examples are shown for the discussion of prediction results of the second crack. These four RVEs of the examples were used for analysing the prediction results of the initial crack in Section 4.3.2. Recall the two evaluation criterions for analysis of the prediction performance, these four examples fall into two categories. The first two examples present that the DNN predicted initial crack is around the DEM simulated initial crack. Then the second cracks in these two RVEs are predicted using the features related to the predicted initial crack. The rest two examples present that the contact bond around the DEM simulated initial crack is in the lists of DNN-predicted cracks with the third highest risk. Thus, the second cracks in these two RVEs are predicted using the features related to the predicted initial crack with the third-highest contact force.

The examples in Figure 4-23 and Figure 4-24 are in the first category. Figure 4-23(a) shows the comparison of the DNN and DEM results of the contact forces. The black triangle in Figure 4-23(a) is the highest contact force obtained by the DEM, which is -34.41N. The position of this contact bond in the RVE is plotted as the black triangle (position *M*) in Figure 4-23(b). The red triangle in Figure 4-23(a) is the DNN predicted highest contact force, which is -34.41N. The position of this contact bond in the RVE is plotted as the red triangle (position *M*) in Figure 4-23(b). It is seen that the DNN predicted second crack is right next to the DEM simulated the second crack. In addition, the yellow triangle at position *M* in Figure 4-23(b) is the initial crack. It is seen that the second crack spreads around the initial crack, which reflects that the information on the initial crack is very important for the DNN model to predict the position of the second crack. The DNN model can predict this second crack successfully, which shows that the DNN model can learn the relation between the input features and the output well. Figure 4-23(c) is the DEM simulated crack path of the RVE under a load of transverse tension at failure. It is also found that the DNN predicted second crack is in the whole crack path, as shown in Figure 4-23(c).

The second example is presented in Figure 4-24. The black triangle at the bottom-left in Figure 4-24(a) is the predicted highest contact force, which is -36.12N. The DEM simulated contact force of this contact bond is also the highest and is -34.03N. The position of this contact bond in the RVE is plotted as the black triangle (at position *N*) in Figure 4-24(b), which shows that the DNN predicted second crack is at exactly the same position as that of the DEM simulated initial crack. This second crack is next to the initial crack (see the yellow triangle at position *N*). In Figure 4-24(c), the cracks will propagate from the position of the first several cracks up and down for forming the crack path at the failure.

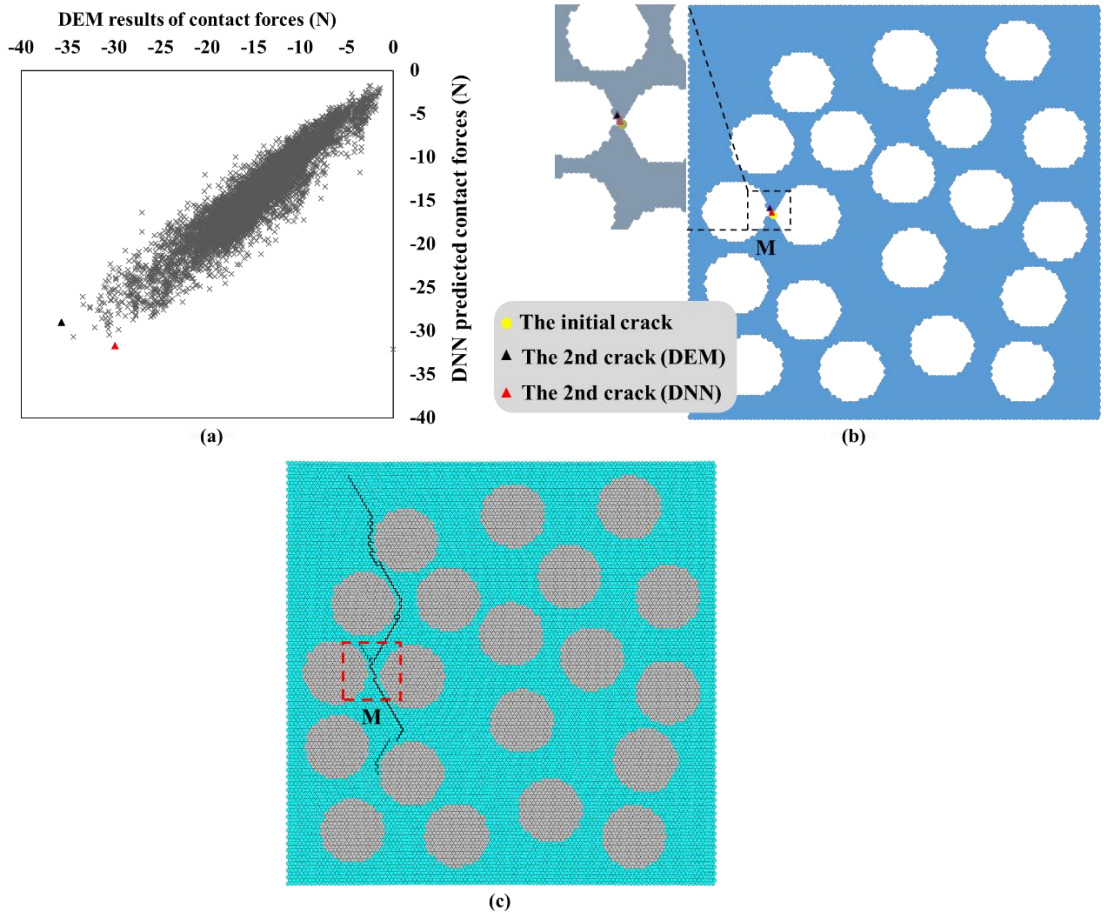

Figure 4-23: (a) DNN regression results of contact forces. (b) The second crack in the RVE. (c) The DEM simulated crack path.

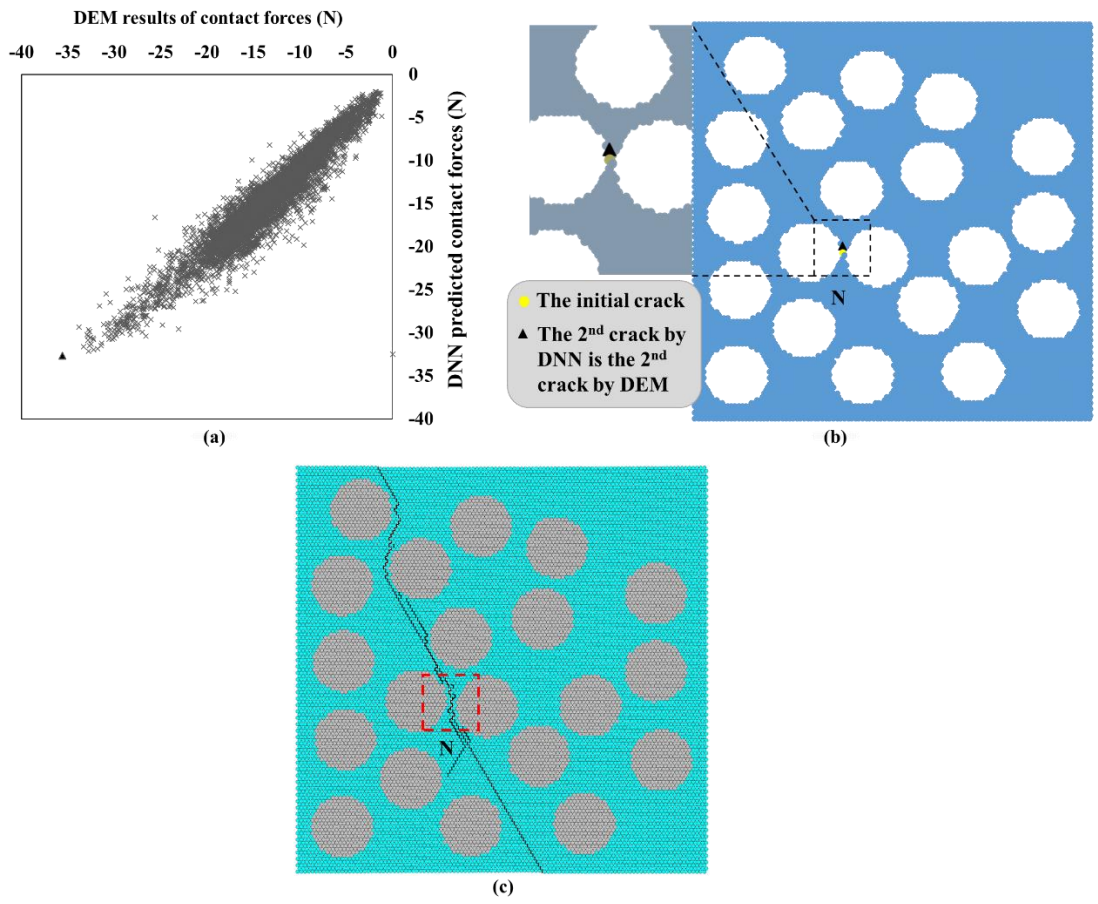

Figure 4-24: (a) DNN regression results of contact forces. (b) The second crack in the RVE. (c) The DEM simulated crack path.

The examples in Figure 4-25 and Figure 4-26 are in the second category. The DNN predicted initial cracks are plotted as the yellow triangle in Figure 4-25(b) and Figure 4-26(b). These two initial cracks are in the list of DNN predicted cracks with the third highest risk. The black triangle in Figure 4-25(a) represents the highest contact force of the contact bond simulated by the DEM model. This contact bond is marked as a black triangle at position *X* in Figure 4-25(a). The red triangle in Figure 4-25(a) represents the highest contact force predicted by the DNN model. The contact bond with this contact force is plotted as the red triangle at position *X* in Figure 4-25(b), which is very close to the DEM simulated second crack. In addition, these three cracks at position *X* are adjacent to each other and are all on the crack path (see Figure 4-25(c)).

The second example in this category is shown in Figure 4-26. The DNN predicted second crack is marked as the red triangle (at position *Y*) in Figure 4-26(b), of which the contact force is shown as the red triangle in Figure 4-26(a). The DNN predicted second crack (red triangle at position *Y* in Figure 4-26(b)) is right around the DEM simulated one (black triangle at position *Y* in Figure 4-26(b)). It is found that the DNN predicted initial, and second cracks are in the whole crack path (see position *Y* in Figure 4-26(c)). It can be concluded that the proposed DNN predictive model can accurately and effectively predict the positions of the first two cracks.

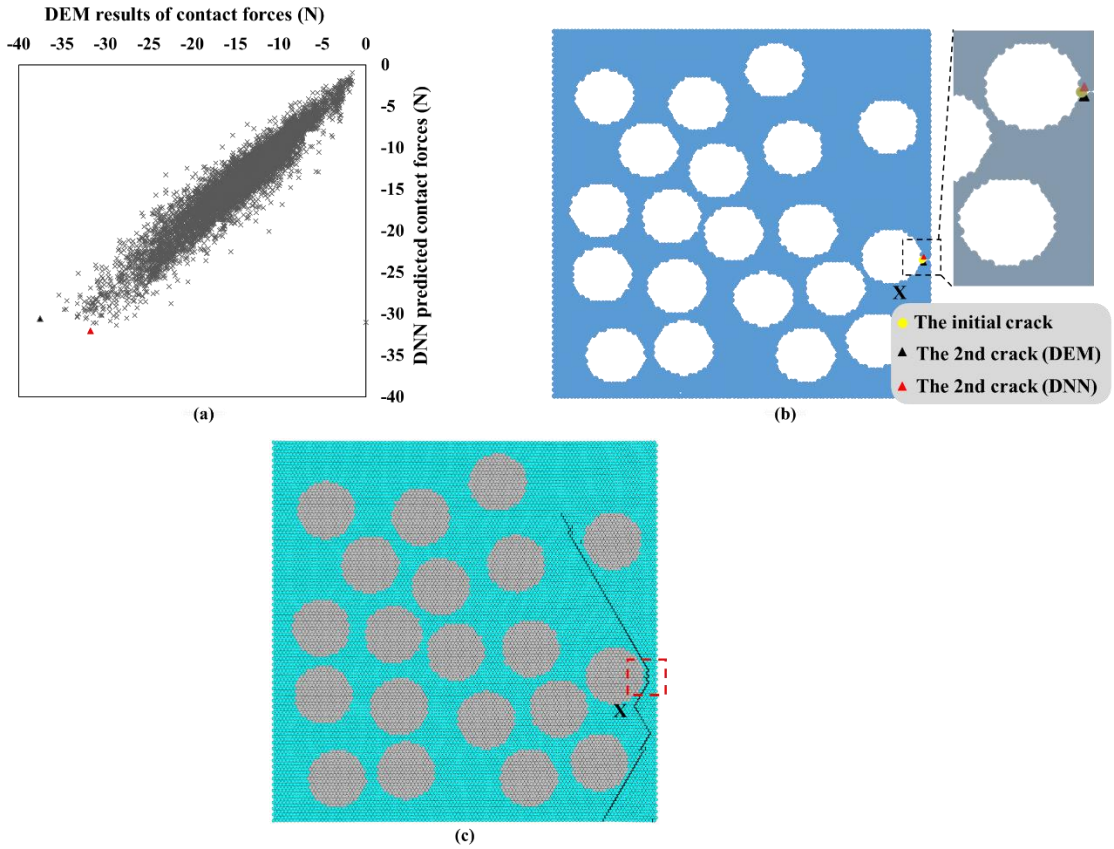

Figure 4-25: (a) DNN regression results of contact forces. (b) The second crack in the RVE. (c) The DEM simulated crack path.

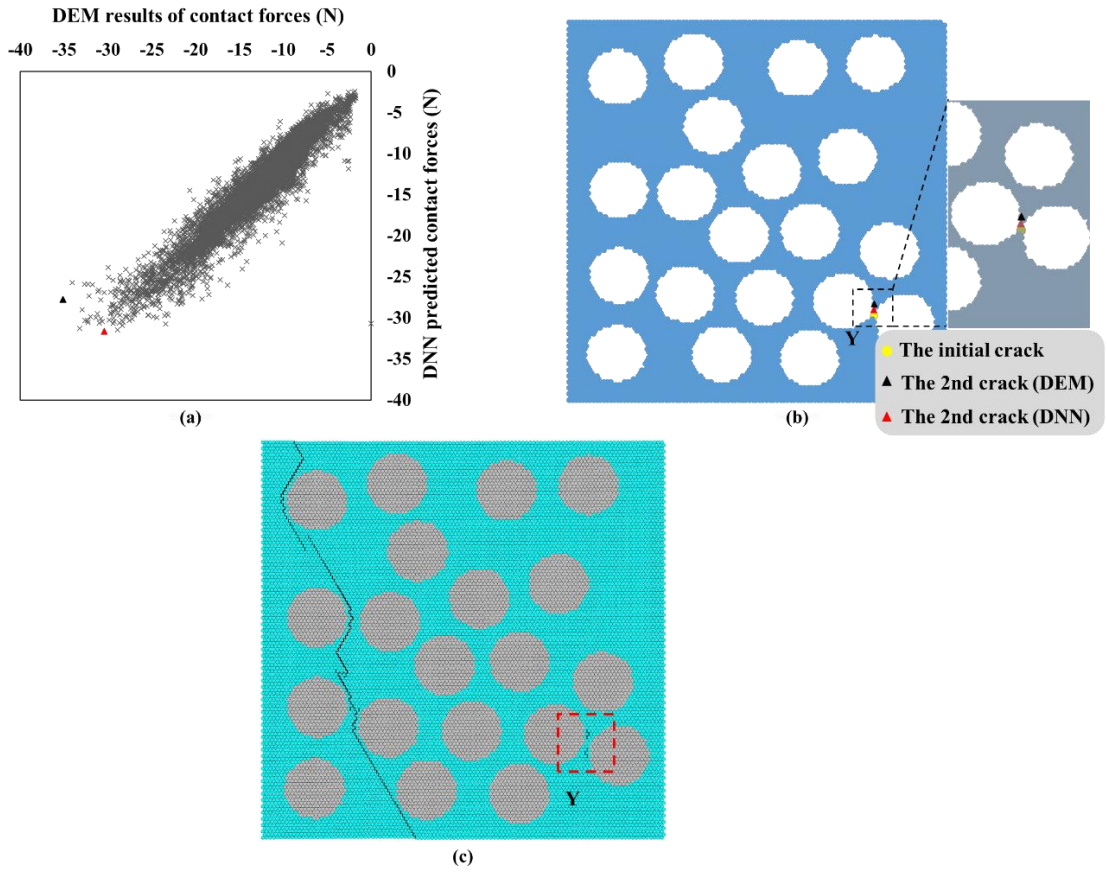

Figure 4-26: (a) DNN regression results of contact forces. (b) The second crack in the RVE. (c) The DEM simulated crack path.

4.4 Summary

The DEM model shows its significant advance in providing accurate and reliable simulation results that can be used in data-driven predictive models. Thus, two relatively simple and easily used ML models, the Gaussian Naïve Bayes classifier and Artificial Neural Networks (ANNs) are first developed for predicting the crack path of the UD FRP lamina. A set of 500 reduced-size RVE samples is selected and simulated by the DEM model. The training accuracy Gaussian Naïve Bayes classifier is good, however, the prediction results by the trained Gaussian Naïve Bayes classifier show not very satisfactory accuracy. This is usually caused by the problem of overfitting. Then,

a 3-fold cross-validation is employed in the developed feedforward ANN. Three different ratios of training data (17.5%, 26%, and 40 %) are selected using undersampling and trained into the network. It can be found that the accuracy of the training process increases by enlarging the number of training data during the undersampling process**.** But the testing result is still not very satisfactory. Dropout is then used in the network to improve the performance, which gives a better prediction result than the original network.

Then a multi-layer DNN model with back-propagation is developed based on the results of 1600 DEM simulations for the predictions of the crack areas of an FRP composite lamina. After training the DNN model, most of the initial cracks and the overall trends of cracking paths can be predicted successfully. It can also be concluded that the DNN model is capable of predicting both occurrences of local cracks areas and cracking density of the RVE sample with full consideration of random fibre distribution.

The DNN prediction for the crack initiation in the UD FRP lamina is also conducted in this chapter. For the prediction of the first crack, the input features are determined by the fibre distribution for reflecting the randomness of fibres in each RVE. The output is the contact force of the contact bond. The contact bond with the largest regressed contact force is regarded as the DNN-predicted initial crack. Two criterions are considered for analysing the prediction performance. Based on criterion I, the accuracies are 65%. Based on criterion 2, the accuracy is 92%. Then, a DNN regression model that learns a different set of features is built to predict the second crack. New features related to the position of the initial crack in the RVEs are added. The criterion for evaluating the prediction performance is whether the DNN predicted crack is around the DEM simulated second crack. According to this criterion, the second cracks in 65 RVEs are predicted successfully by the DNN model, of which the accuracy is 92% ∗

$65\% \approx 60\%$. The prediction accuracy is not very high, which indicates that the problem of predicting the second crack is a bit complex based on the current input features.

Chapter 5

5 Effects of defects on the transverse mechanical response of unidirectional fibre-reinforced polymers: DEM simulation and deep learning prediction

This chapter presents a 2D RVE-based DEM model for analysing the effects of defects on the transverse mechanical response of unidirectional (UD) fibre-reinforced polymer (FRP) laminae. The crack initiation and propagation in defective RVEs with different fibre distributions are analysed and compared. For further exploring the relation between initial cracks and the distribution of defects, deep learning models are developed for a fast determination of crack initiation and instantaneous critical load of the RVEs based on a data set generated by DEM simulations.

5.1 Configuration of the DEM model for the defective UD FRP laminae

5.1.1. RVE generation

Defects formation in FRP would occur due to negligence during the manufacturing process of FRP [147], and it can strongly affect the mechanical properties of FRP [44, 46, 148]. Defects may be arbitrarily shaped, which causes a relatively expensive cost for the generation of defects. Experimental results [149] showed that the defects in FRP composites were elongated and distributed along the fibre direction, which enables defects to be generated in 2D samples. Figure 5-1(a) is the cross-section of a UD FRP

lamina. It is shown that defects within the matrix and along the fibre-matrix interface usually exist. The defects in both the matrix and the fibre-matrix interfaces are therefore considered in this study.

The defective UD FRP composite laminae with three different types of fibre distributions are analysed, which are the random fibre distribution and two different patterns of periodic fibre distributions. Firstly, the generation of RVEs of defective UD FRP laminae is carried out. The first two types of distributions of fibres in RVEs of defective UD FRP laminae are two periodic fibre distributions, which are the laminae with the rectangular arrangement of fibres (type I) and the hexagonal arrangement fibres (type II), respectively. A $60\,\mu m \times 60\,\mu m$ type I RVE of the cross-section of the lamina (as shown in Figure 5-1(b)) is firstly generated by the DEM software 'PFC2D'. The generated RVE are discretized with particles by the hexagonal packing arrangement and contains 49 randomly distributed circular fibres of radius $R_f = 3.276\,\mu m$, of which fibre volume fraction is 45.9%. The target defect volume fraction of the RVE is 1.2%. The ratio of the matrix and interfacial defects is set to be 1:1 (i.e., the volume fractions of the matrix and interfacial defects are identical at 0.6%). Thus, 25 randomly distributed circular porous defects of radius $R_{m\_d} = 0.495\,\mu m$ in the matrix are generated in the RVE.

The generation of debonding defects along the fibre-matrix interface is implemented by combining to use the function of 'random. sample' in Python and the DEM software 'PFC 2D 6.0'. To ensure the interfacial defect volume fraction and the randomness of the distribution of interfacial defects, 8 of 49 fibres in the RVE are randomly chosen using the function of 'random. sample' in Python for containing the interfacial defects. Then the locations of defects along fibre-matrix interfaces are determined by the DEM

software ‘PFC 2D 6.0’. Totally 28 defects along the eight fibre-matrix interfaces with equal lengths are generated in the type I RVE.

For the type II RVE, the fibre and the defect volume fractions are approximately 44% and 1.2%, respectively. The volume fractions of the matrix defect and the interfacial defect are set identically as 0.6%. As shown in Figure 5-1(c), there are 42 fibres with a uniform fibre radius of 3.465μm and 20 randomly distributed matrix defects of a radius of 0.527μm. There are also 28 defects along eight fibre-matrix interfaces with equal lengths in the type II RVE.

Besides the RVEs with periodically distributed fibres, the RVE of the defective lamina with random fibre distribution (type III) is generated lastly. The dimension of this type of RVE is also $60\ \mu m\ \times\ 60\ \mu m$. The radii of the fibre and the matrix defect are $3.32\ \mu m$ and $0.37\ \mu m$, respectively. An example of type III RVE, as shown in Figure 5-1(d), contains 64 fibres with a uniform fibre radius of $3.32\ \mu m$ and 39 randomly distributed matrix defects of radius $0.37\ \mu m$. The number of the interfacial defects is 28. These are also along eight fibre-matrix interfaces with equal lengths. The fibre and defect volume fractions of this type III RVE are approximately 60% and 1.2%, respectively. The above geometry configurations of RVEs mentioned above are in the acceptable and reasonable ranges for “good materials properties” [45, 46].

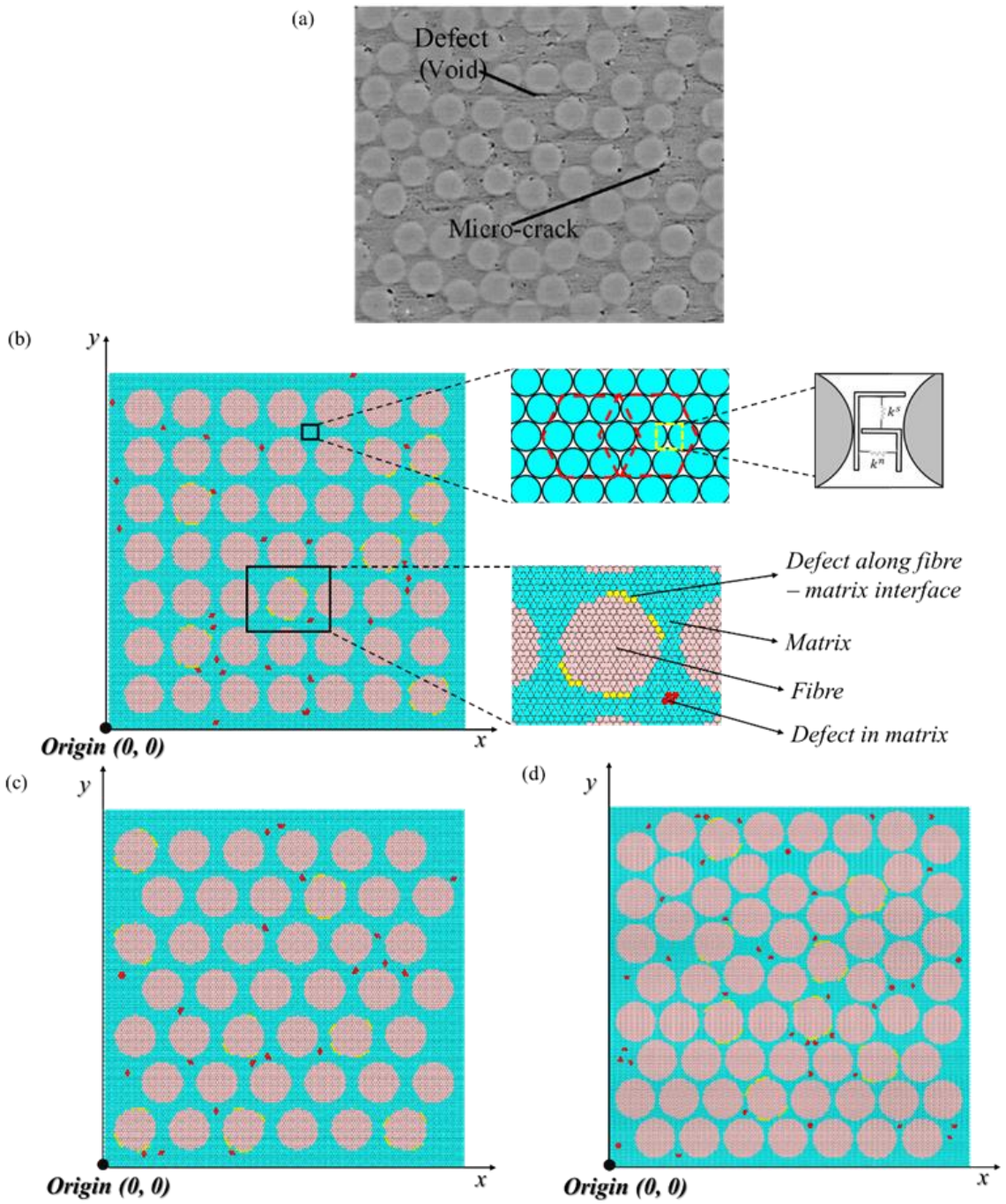

Figure 5-1: (a) An example SEM image of UD FRP composite with defects, adopted from [150]. (b) A DEM approached RVE generation and its discretization (type I: rectangular arrangement of fibres). (c) RVE with a hexagonal arrangement of fibres (type II). (d) RVE with randomly distributed fibres (type III).

5.1.2. Contact models and the calibrations

In the RVEs shown in Figure 5-1(b)-(d), the areas coloured by the red particles are the matrix defects, and the areas coloured by the yellow particles are the defects along the fibre-matrix interface. In the DEM simulations, the contact bonds between particles within the areas of matrix defects and interfacial defects are ignored by deleting this type of contact bonds. As a result, three types of contact bonds remain the contact bond between two fibre particles, the contact bond between two matrix particles and the contact bond between a fibre particle and a matrix particle. In the DEM model for simulating the mechanical response, particles of fibres and particles of the matrix are respectively bonded at contacts by parallel bonds. The behaviour of parallel bonds is described using the parallel bond model. Contacts of fibre and matrix interface are represented by soft bonds and modelled by the soft-bond model.

Similar to the calibrations of the macro and micro parameters in the study for the mechanical response of the defect-free UD FRP lamina, the micromechanical properties that characterize the DEM model are also calibrated by the macroscopic properties of each composite constituent obtained from experimental tests. The material properties of fibre, matrix and fibre/matrix interface for the defective FRP composite lamina are also found in Table 3-1. It is assumed that both the fibres and the matrix are isotropic in the DEM model. The contact stiffness used in the DEM model can be expressed explicitly as functions of Young's modulus and Poisson's ratio of fibres and matrix [138]. The relationship between the macro strength of the matrix and the micro strength of the matrix bonds was linear, and the linear coefficient was also used as 1.7 [139], which results in the micro-contact tensile strength of the matrix bond is therefore 105 MPa. The micro-contact tensile strength of the fibre bond is set as a very large value as it is assumed that there is no fibre damage under the loading of transverse tension.

Additionally, the fibre-matrix interface strength used in the DEM model is also obtained using the Mohr-Coulomb criterion. The fibre-matrix interface strength for studying the effect of defects in the lamina is taken as the double values of the cohesion yield stress, which gives a fixed normal interface strength of $78.2\ MPa$. The 2D RVE-based DEM model is eventually developed.

5.2 DEM model simulation

5.2.1. DEM Model validation

A constant tensile velocity of 5 mm/s is applied simultaneously on the particles located at both the left and right boundaries of the DEM model to study the transverse mechanical behaviour of the defective UD FRP lamina. An RVE of UD FRP lamina with the same 60% fibre volume fraction and an almost identical fibre distribution to the experimental sample see Figure 5-2(a)) is simulated using the DEM. Figure 5-2 (b) shows that the simulated cracks have a good agreement with the crack patterns measured by the in-suit microscopic test (see Figure 5-2(a)). It can be concluded that the DEM model can provide accurate and reliable simulation results for studying the fracture process of defective UD FRP laminae.

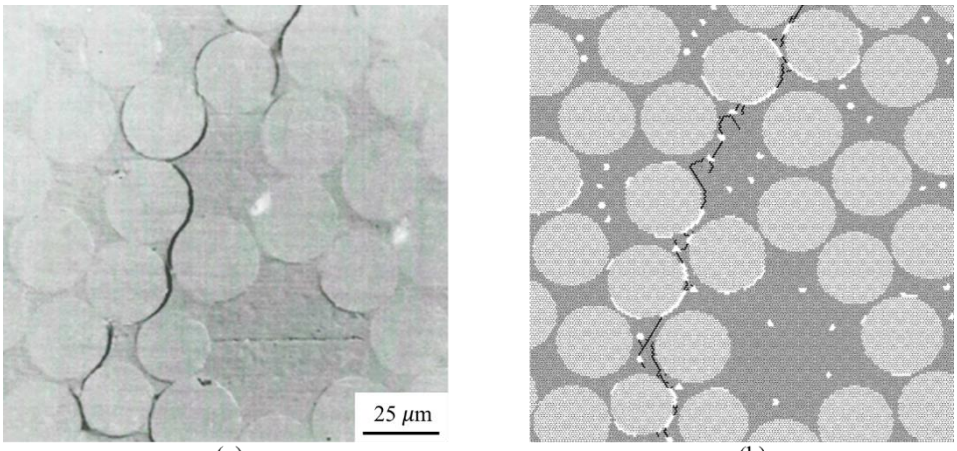

Figure 5-2: Crack path of defective UD FRP laminae under transverse tension. (a)Experimental result [151]. (b)DEM simulation result.

5.2.2. Effect of the presence of defects in matrix and interface

The effect of the presence of defects on the mechanical response for the three types of RVEs under transverse tension is studied. The experimental results of transverse cracks in the two RVEs with periodic fibre distributions are shown in Figure 5-3. Firstly, it is shown that the presence of matrix and interfacial defects in the Type I RVE affects the stress-strain curves (see Figure 5-4(e)). The maximum stress of the Type I RVE is 52.03MPa at around 0.544% strain, which is 20.7MPa lower than that (72.75MPa) of the RVE without defects at around 0.731% strain. The simulated crack initiation and propagation of the RVE are shown in Figure 5-4(a-d). The presence of the defects induces stress concentrations, which leads to crack initiation. As shown in positions *X* and *Y* in Figure 5-4(a), the cracks initiate around the two defects in the fibre/matrix interfaces at the middle of the RVE, where there are relatively dense matrix defects and defects. Subsequently, several cracks propagate through the matrix (see Figure 5-4(b)), of which stress reaches the maximum, i.e., 52.914MPa (point B in Figure 5-4(e)). After that, the cracks continue to grow up and down through the matrix and interfacial defects

(Figure 5-4(c)). The corresponding stress and strain are approximately 41.728MPa and 0.608% (point C in Figure 5-4(c)), respectively. In Figure 5-4(d), long cracks at the failure (point D) are connected among matrix and interfacial defects. Due to the presence of the defects in the matrix and along the fibre-matrix interface, the DEM simulated crack path in type I defective RVE at failure (see Figure 5-4(d)) is slightly different compared to the experimental one (see Figure 5-3(a)). The experimental result shows that cracks propagate through the fibres in the middle of the lamina, while the crack propagation in the defective RVE obtained from the DEM model is altered and influenced by interfacial defects and matrix defects. In addition, the stiffness is slightly affected by the defects. The stiffness of the defective RVE is smaller than that of the defect-free RVE. It can be also seen that the presence of defects causes the ultimate failure at a lower overall strain compared with the RVE without any defect (see Figure 5-4(e)).

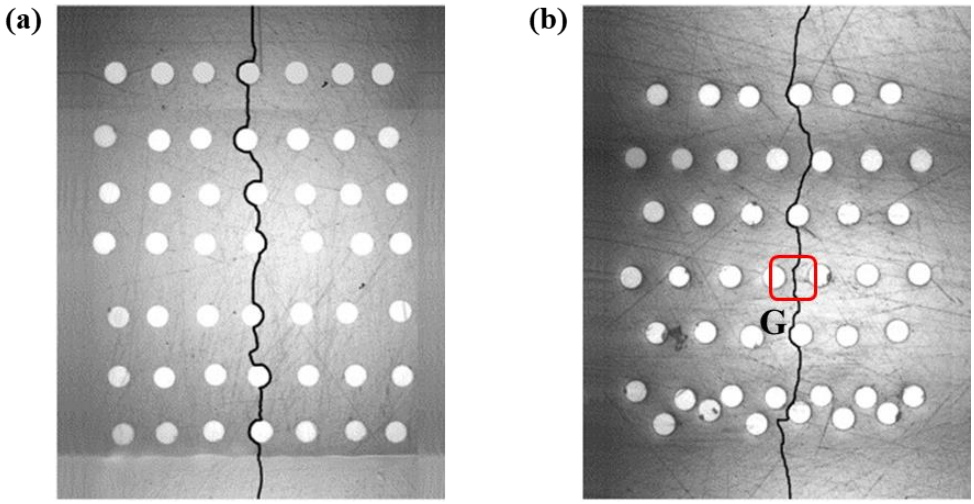

Figure 5-3: Experimental tests of cracks in (a) type I RVE and (b) type II RVE. [152]

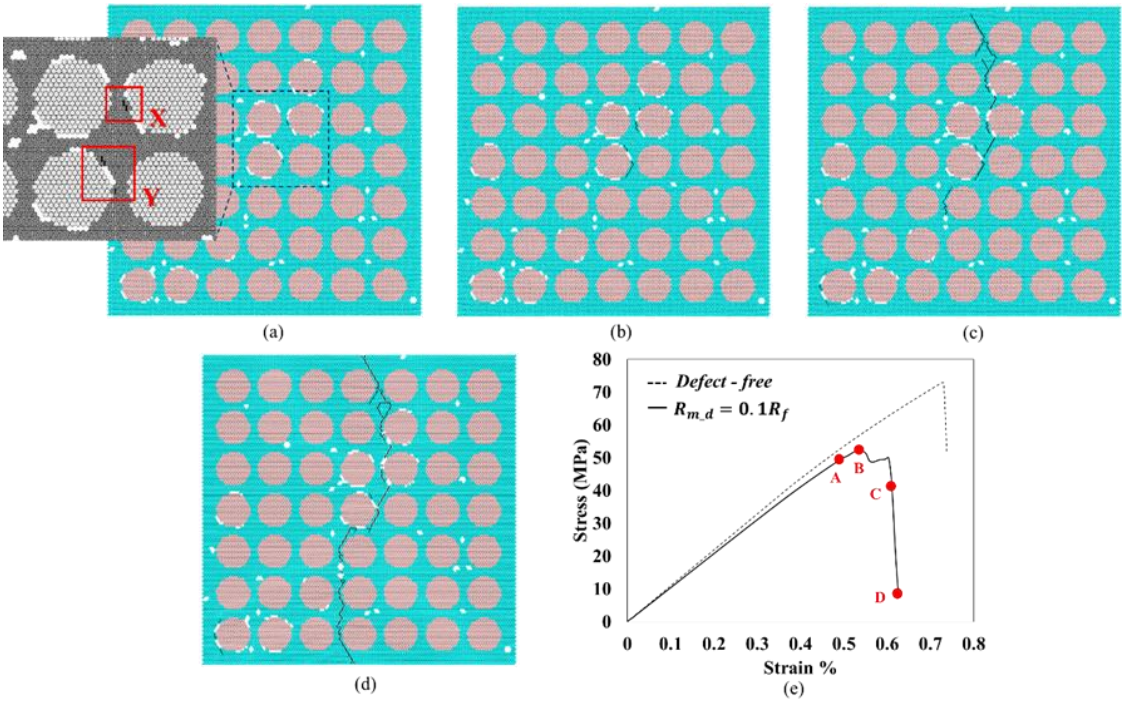

Figure 5-4: The mechanical behaviour of a type I RVE with $V_f = 45\%$ and $V_d = 1.2\%$, $R_{m\_d} = 0.1\ R_f$ under transverse tension. (a-d)Cracks at the strains of 0.499%, 0.536%, 0.608% and 0.633%. (e)Stress-strain curve.

Similarly, the damage progression and the stress-strain curve of the Type II RVE are also obtained and analysed using the DEM model. In Figure 5-5(d) and Figure 5-3(b), it is seen that the presence of the defects in the matrix and fibre-matrix interface affects the trajectory of crack development with the comparison to the crack path in a lamina obtained from the experimental test. In detail, the initial cracks occur around the two fibres with interfacial defects (see positions *X* and *Y* in Figure 5-5(a)). Then the cracks propagate and an additional short crack develops from one of the interfacial defects in the middle of the RVE when the stress reaches the maximum stress of 49.408MPa (point B in Figure 5-5(e). This short crack grows in the matrix between two horizontally neighbouring fibres at position *H* in Figure 5-5(b), which shows a good agreement with the experimental observation of the crack path in the lamina with the hexagonal fibre distribution (see position *G* in Figure 5-3(b)). With the increase of loading, cracks

generated from the matrix and interfacial defects coalesce with an ultimate strain of 0.744%. Compared to the crack path of the Type I RVE, the crack path of the Type II RVE is slightly longer with a larger strain, which suggests that crack propagation of the Type II RVE requires greater fracture energy to reach the final failure.

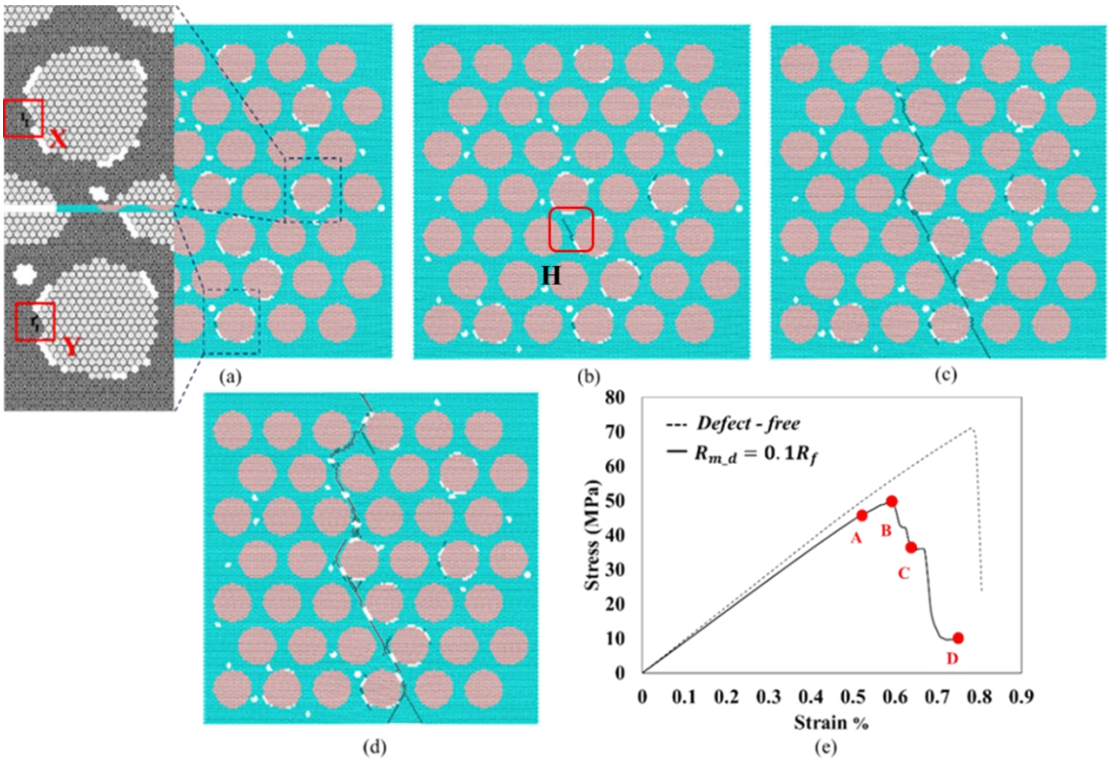

Figure 5-5: The mechanical behaviour of a type II RVE with $V_f = 45\%$ and $V_d = 1.2\%$, $R_{m\_d} = 0.1R_f$ under transverse tension. (a-d)Cracks at the strains of 0.529%, 0.596%, 0.64% and 0.744%. (e)Stress-strain curves.

The effect of the presence of matrix and interfacial defects in the Type III RVE on the mechanical response is shown in Figure 5-6. The cracking in this RVE initiates from the three interfacial defects on the right of the RVE, as shown in Figure 5-6(a) at the positions *X*, *Y* and *Z*. The corresponding stress and strain of the RVE are approximately 45MPa and 0.31% (point A in Figure 5-6(e)), respectively. Several cracks propagate through the matrix (see Figure 5-6(b)) when the stress reaches the maximum stress (point B in Figure 5-6(e)). After that, the cracks are connected (Figure 5-6(c)-(d)) across the defects, forming the final crack path at failure (Point D). In addition, the Type III

RVE has a maximum stress of 50.6MPa at around 0.379% strain, which is 8.9MPa smaller than that (59.5MPa) of the RVEs with a random fibre distribution but without defects. The presence of defects in this RVE also causes earlier ultimate failure (see Figure 5-6(f)).

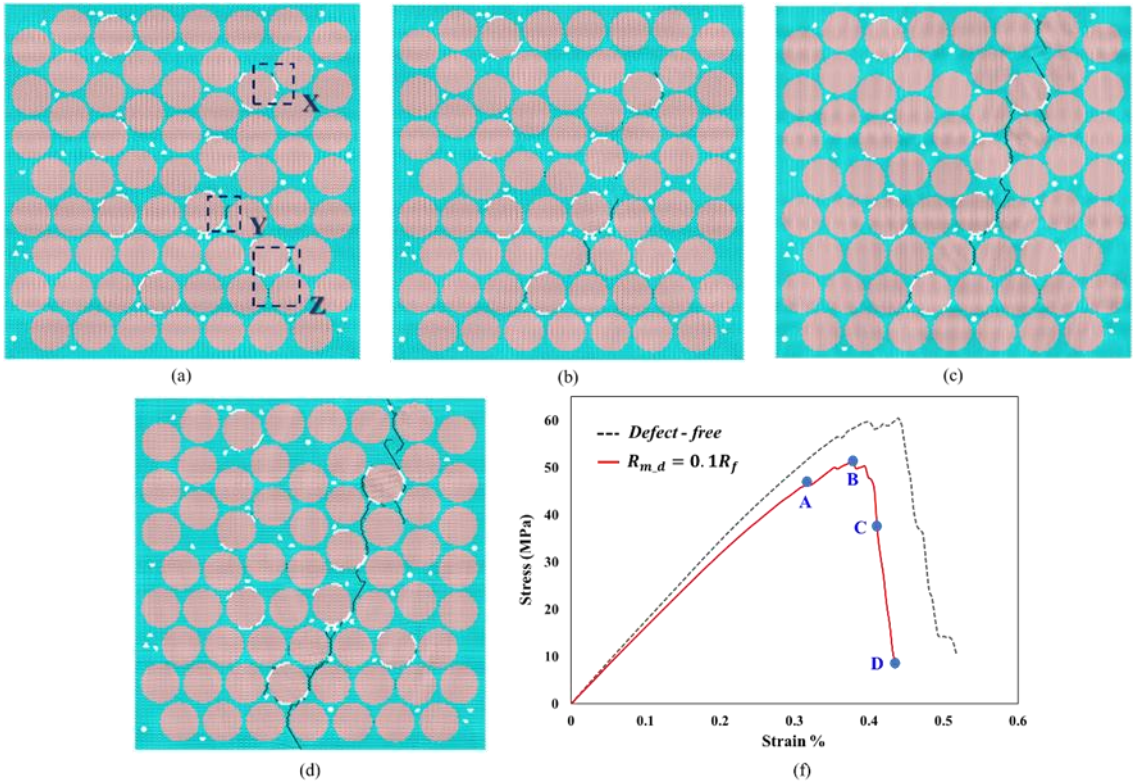

Figure 5-6: Effect of the presence of defects on the mechanical behaviour under transverse tension of an RVE with $V_f = 45\%$ and $V_d = 1.2\%$, $R_{m\_d} = 0.1R_f$. (a)Crack path of a typical RVE without defects. (b-e)Cracks of the RVE with defects at the strain of 0.312%, 0.378%,0.401%, and 0.435%. (f)Stress-strain curves.

5.2.3. The effect of the size of defects distributed in the matrix

The effect of the size of defects distributed in the matrix on the behaviour of the stress-strain curve and crack path at the failure point are illustrated in Figure 5-7 and Figure 5-8. In Figure 5-7, the RVEs contain the same fibre distribution with fibre

volume fraction $V_f = 60\%$ and defect volume fraction $V_d = 1.2\%$, but different sizes of porous defects in matrix, $R_{m\_d} = 0.1R_f, 0.15R_f, 0.2R_f$ and $0.25R_f$. The distribution of fibre-matrix interfacial defects in these four RVEs is not changed. It can be implemented in the DEM software 'PFC 2D'. Detailly, the 'PFC 2D' can generate matrix defects with different sizes while maintaining the target volume fraction of 60% and the distribution of interfacial defects. The trends of the stress-strain curves of the four RVEs are similar, and all their strengths are approximately $50.5MPa$, which shows that the tensile strength is not affected by the size of matrix defects. However, the damage paths of all cases at final failure are relatively different, and it is found that the damage path is sensitive to the distribution and size of matrix defects. The cracks always occur from the interfacial defects and propagate through the matrix defects. With the increase of the radii of defects, cracks merge among matrix defects more frequently (see Figure 5-7(c-d)), which indicates that large matrix defects affect more on the crack paths. Moreover, it is found that the ultimate strain at failure increases as the radius of the matrix defect increases. The RVE with the largest radius of matrix defect ($R_{m\_d} = 0.25R_f$) has the largest ultimate strain.

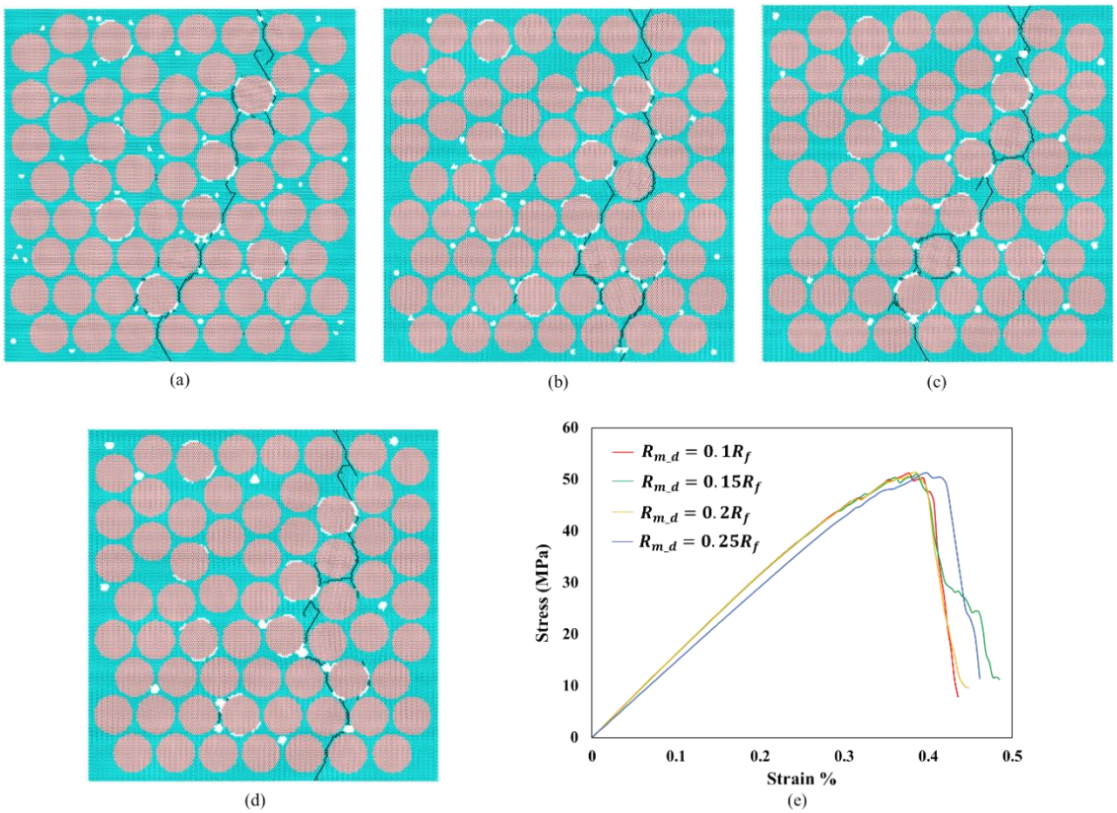

Figure 5-7: Effect of matrix defect size on the mechanical behaviour under transverse tension of an RVE containing $V_f = 60\%$ and $V_d = 1.2\%$. (a) $R_{m\_d} = 0.1R_f$. (b)$R_{m\_d} = 0.15R_f$. (c)$R_{m\_d} = 0.2R_f$. (d)$R_{m\_d} = 0.25R_f$. (e)Stress-strain curves.

The mechanical behaviours of RVEs containing the same fibre distribution with fibre volume fraction $V_f = 45\%$ and defect volume fraction $V_d = 1.2\%$, but different sizes of porous defects in the matrix, $R_{m\_d} = 0.1R_f, 0.15R_f, 0.2R_f$ and $0.25R_f$ are also analysed and presented in Figure 5-8. The stress-strain response of the four RVEs is relatively similar. The tensile strengths of the four RVEs are not affected by the size of matrix defects much and the corresponding stiffness is not changed as the radii of the matrix defects change. In addition, compared to the stress-strain curves of the RVEs with the 60% fibre volume fraction, it is found that the ultimate strain at failure of the RVE with a higher fibre ratio (60%) is smaller than that of the RVE with a lower fibre ratio (45%). On the other hand, the crack paths of all cases at final failure are relatively similar. The cracks first occur from the interfacial defects and propagate through the

defects in the matrix and interface. The damage path is not much dependent on the distribution and size of matrix defects in the RVEs. It is indicated that the interfacial defects play important roles in crack propagation in the RVEs with the 45% fibre volume fraction.

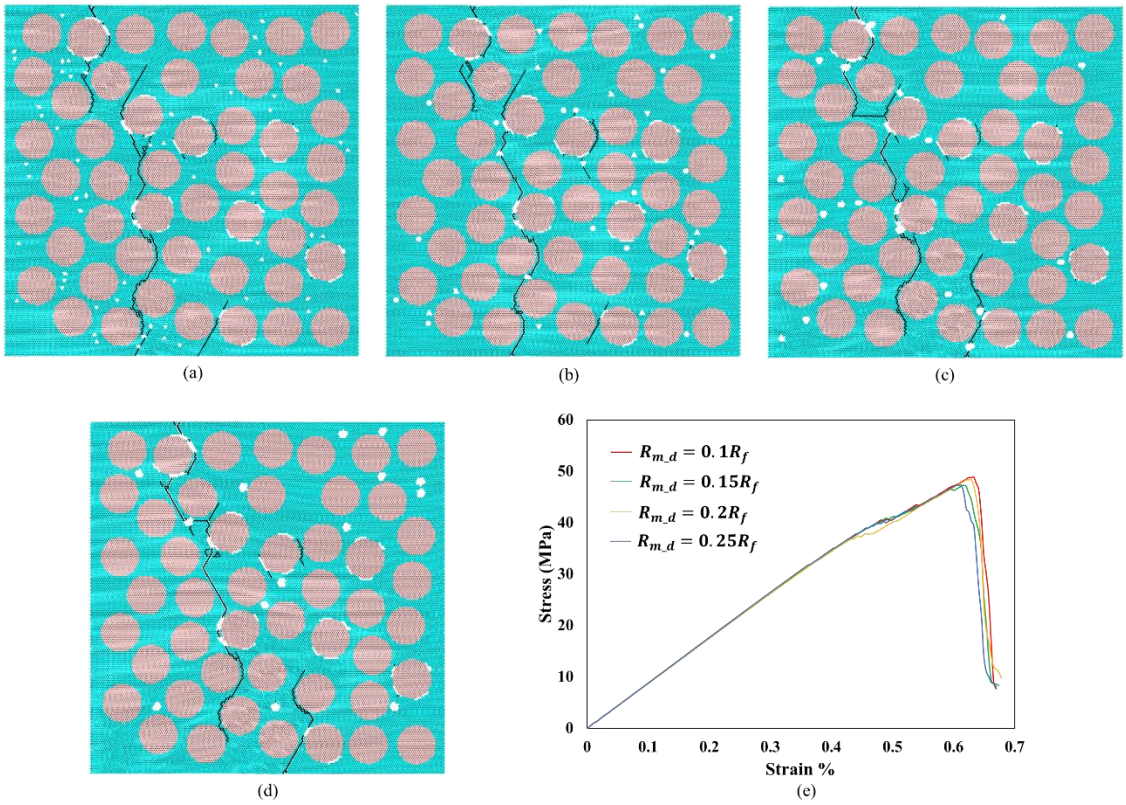

Figure 5-8: Effect of matrix defect size on the mechanical behaviour under transverse tension of an RVE containing $V_f = 45\%$ *and* $V_d = 1.2\%$ *. (a)* $R_{m\_d} = 0.1R_f$ *. (b)*$R_{m\_d} = 0.15R_f$*. (c)*$R_{m\_d} = 0.2R_f$*. (d)*$R_{m\_d} = 0.25R_f$*. (e)Stress-strain curves.*

Then, the DEM simulations of RVEs containing the same fibre distribution (45%) but different matrix and interfacial defects distributions are carried out and shown in Figure 5-9. It is found that the crack paths in the four RVEs are completely different, which is indicated that the distributions of both matrix defects and interfacial defects influence the crack path. Combining the results shown in Figure 5-8, it can be confirmed that the interfacial defects affect the crack propagation in the RVEs with lower fibre volume fraction the most, leading to different crack paths at failure.

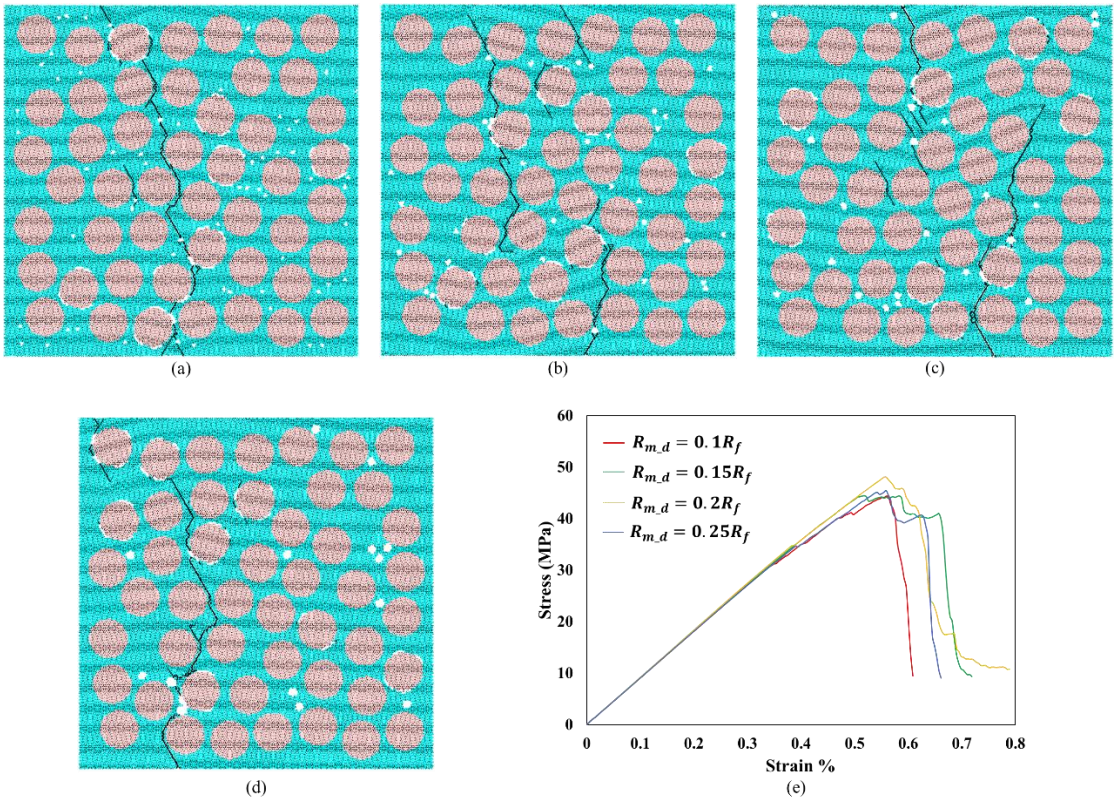

Figure 5-9: Effect of matrix defect size on the mechanical behaviour under transverse tension of an RVE containing $V_f = 45\%$ and $V_d = 1.2\%$. (a) $R_{m\_d} = 0.1R_f$. (b)$R_{m\_d} = 0.15R_f$. (c)$R_{m\_d} = 0.2R_f$. (d)$R_{m\_d} = 0.25R_f$. (e)Stress-strain curves.

5.2.4. Effect of the distribution of the defects

For the two types of defects considered, namely, matrix and interfacial defects, the effect of the distribution of the defects on the deformation and failure of the composite lamina is studied and presented in Figure 5-10. The stress-strain curves of three typical Type III RVEs having the same fibre distribution with fibre volume fraction $V_f = 60\%$ and the same defect volume fraction $V_d = 1.2\%$,but three different distributions of the defects, i.e., all matrix defects, half matrix defects and half interfacial defects, and all interfacial defects, are shown in Figure 5-10(a). The stress-strain curves show that the distribution of defects affects both the strength and stiffness of the material. An increase

in interfacial defects reduces both strength and stiffness. To show the variations of the strength and stiffness caused by different random fibre distributions, the average values of the two mechanical properties from the 13 RVEs with different fibre distributions but the same volume of defects are calculated and plotted in Figure 5-10(b). The average strengths of the RVEs with the three different distributions of defects are 56.85MPa, 52.36MPa and 49.03MPa. Their corresponding stiffness is 14.67GPa, 14.11GPa, and 13.34GPa.

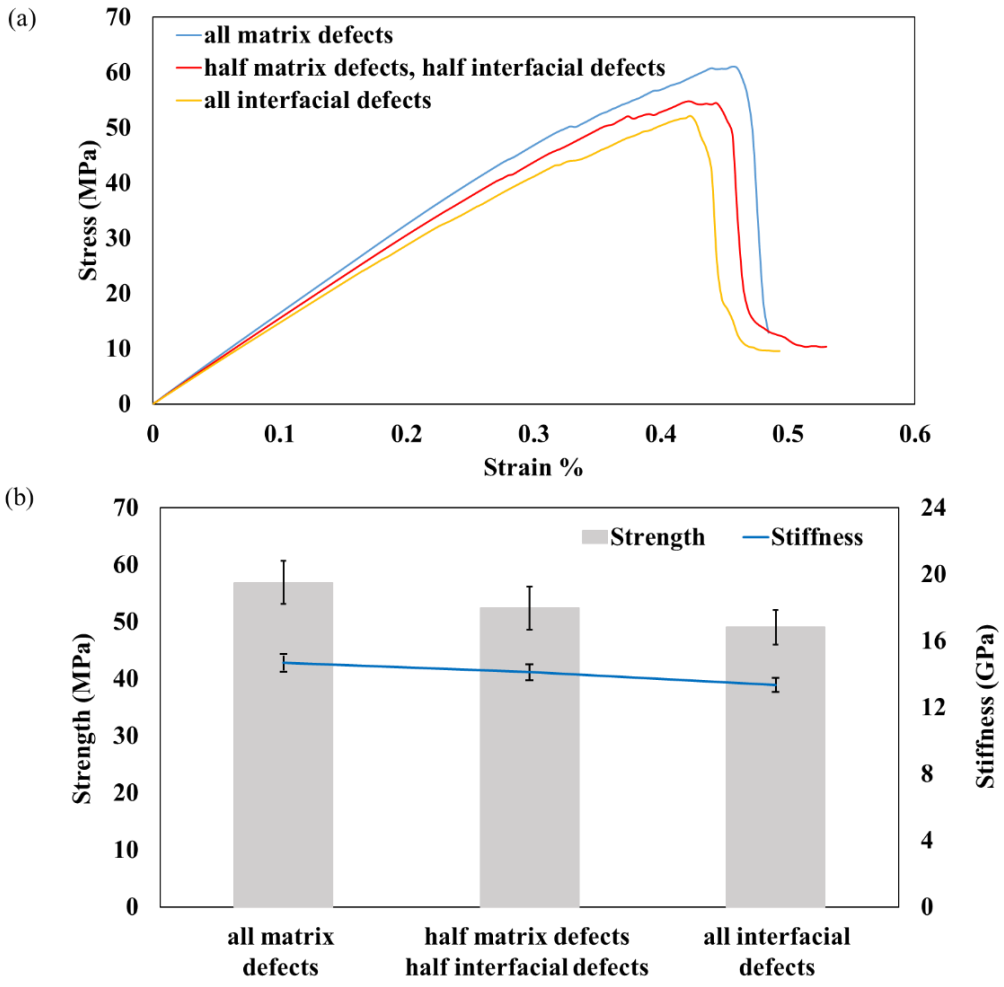

Figure 5-10: Effect of the distribution of the defects on the mechanical behaviour of type III RVEs under transverse tension. (a)Stress-strain curves. (b)The average strength and the average stiffness, and their corresponding variances.

5.3 Development of data-driven deep learning models

To verify that the initial cracks are closely related to the distribution of defects, deep neural network (DNN) regression models are constructed to predict the initial cracks and instantaneous stresses of the defective UD FRP laminae with the two types of periodic fibre arrangements (Types I and II in Figure 5-1(b) and (c)). The deep learning models are trained and tested by the data from the DEM simulations.

5.3.1. Data generation

The data set generated for predicting the initial crack and its stress of UD FRP laminae with rectangular distributed fibres or hexagonal distributed fibres and randomly distributed defects contains 500 RVE samples of dimension $60\,\mu m \times 60\,\mu m$. Therefore, 1000 RVE samples are generated according to the specifications mentioned in Section 5.1.1. To ensure the randomness of the distribution of interfacial defects, 8 of 49 fibres in each RVE are chosen by using the function of 'random. sample' in Python containing the interfacial defects. The locations of defects in fibre-matrix interfaces are determined by the DEM software 'PFC 2D 6.0'. Totally 28 defects along the eight fibre-matrix interfaces with equal lengths are generated in the RVE (see Figure 5-11).

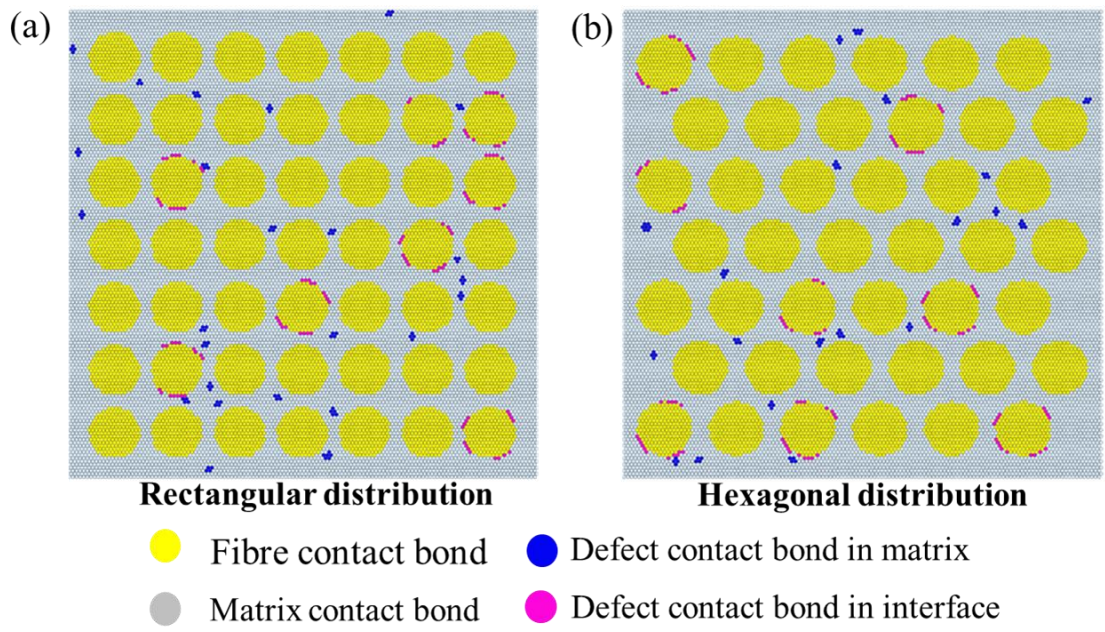

Figure 5-11: RVEs with (a)rectangular distributed fibres and (b)hexagonal distributed fibres.

In the DEM simulation, the contact bond will break if the contact force exceeds the contact strength. Therefore, the same to the last chapter, the target of the developed deep learning model is to regress the contact force of each contact bond in the RVE at the time step just before the first crack occurs, so that fracture of the contact bond can be determined from the regressed contact forces. It has been mentioned in the last chapter that the force of contact bond at the time step immediately before the initial cracking is taken approximately as the critical force of cracking as the time step used in the calculation is sufficiently small ($<2.5e^{-11}s$). It is relatively difficult to calculate the contact force at the exact time of cracking.

There are around 59000 contact bonds in each defective RVE sample obtained by removing the bonds where there are defects, including the defective bond in the matrix-matrix contacts, and in the fibre-matrix interface contacts (see Figure 5-11). To further reduce the size of data to be trained in the DNN model, only the data from the bonds that are likely to crack are collected from the DEM model. In detail, in the matrix, there

are three types of contact bonds with different angles based on the hexagonally packed particles: contact bonds with 0 degree, 60 degrees and 120 degrees, respectively, to the horizontal direction. In all 500 samples for each type of RVEs, the initial crack occurs in the 0-degree contact bond only as the transverse tension applied on the RVE is in the perpendicular direction. The number of the 0-degree contact bonds in each RVE is 9400. As a result, the deep learning model will train and test 4700000 data which are the 4700000 (9400×500) matrix-matrix contact bonds of the 500 RVEs.

To predict the stress of an RVE, when the initial crack occurs, the deep learning model will train and test 500 data according to the results of the DEM simulations (500 for Type I or Type II RVE as in Figure 5-1(a)(b)). The critical stress of the initial crack in an RVE is the single-output, which makes the prediction a single-output regression problem.

5.3.2. Data pre-processing

From the DEM modelling, it is found that the initial cracks are always around the defects, which suggests that each of the contact bonds and the distribution of the defects are critical features and should play an essential role in the training process of the data-driven model for initial crack prediction. As shown in Figure 5-12, the input features are selected as the positions of the matrix-matrix contact bonds (denoted (pos_x_c, pos_y_c)), the distances between every contact bond to each defect (denoted d_{cd_i}) and their corresponding angles with the $x-$axis (denoted θ_{cd_i}), which are computed by Python codes as follows:

$$d_{cd_i} = \sqrt{(pos\_x_c - pos\_x_{d_i})^2 + (pos\_y_c - pos\_y_{d_i})^2} \quad (5\text{-}1)$$

(i = 1, 2, …, 53 or 48)

$$\theta_{cd_i} = arcsin\left(\frac{pos\_y_{d_i}}{d_{cd_i}}\right) \quad (5\text{-}2)$$

where pos_x_c, pos_y_c and $pos\_x_{d_i}$, $pos\_y_{d_i}$ are the $x-$ and $y-$ coordinates of the centre of matrix-matrix contact bond with 0 degree and defect *i*. For one contact bond in the type I RVE, there are 54 pairs of 2D feature vectors, including the positions of the contact bond, 25 pairs of distance and angle to the matrix defects and 28 pairs of distance and angle to the interfacial defects. Similarly, there are 49 pairs of 2D feature vectors for one contact bond in the type II RVE, including the contact bond's positions, 20 pairs of distance and angle to the matrix defects and 28 pairs of distance and angle to the interfacial defects.

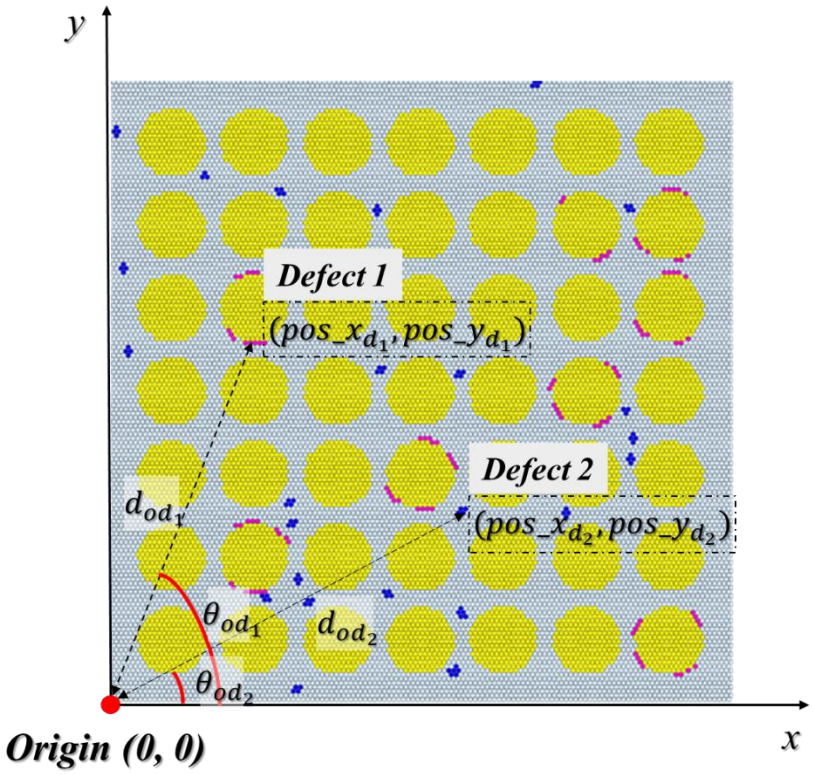

Figure 5-12: Feature selections for predicting the initial crack.

The features for the model predicting the stress of the initial crack are considered based on the randomly distributed defects in RVEs. Therefore, the positions of the randomly distributed defects corresponding to the origin of the RVE, for instance, $(x_{d_1}$,

y_{d_1}) and (x_{d_2}, y_{d_2}), and the distance to the origin (denoted d_{od_i}) and the corresponding angle with $x-$axis (denoted θ_{od_i}), are used as the input features to represent the relative spatial distribution of the defects (see Figure 5-13). Additionally, the distances are set in an ascending order to the nearest to the farthest to improve the efficiency of the training of the DNN model. Therefore, 53 and 48 pairs of 2D input features are determined for the type I and II RVEs, respectively.

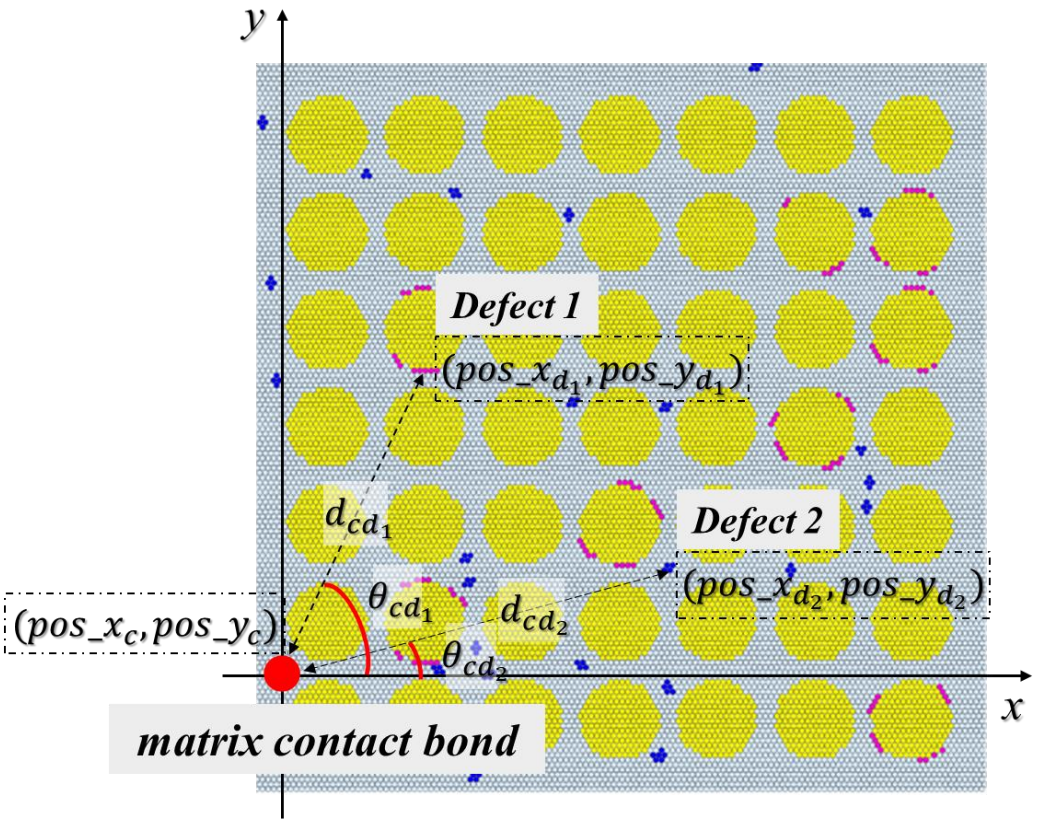

Figure 5-13: Feature selections for predicting stress of the initial crack.

In the DNN model for predicting the initial crack, for each composite configuration, 90% of the data (450 samples) from 500 RVEs are used as training data for the DNN predictive model and the rest 10% of the data (50 samples) are used as testing data. And in the DNN model for predicting stress, 90% of the data (450 RVE samples) are used as training data, and the rest samples (50 RVE samples), are used as testing data. Finally, to ensure that all the features are of the same scales, Z-score normalization is used to

rescale the features in the training set and the testing set in the predictive models independently.

5.3.3. Configuration of the DNN models

As shown in Figure 5-14, a back-propagation DNN model is developed for this study. In the model for predicting the initial crack in type I or type II RVE, there are 54 or 49 pairs of 2D feature vectors in the input layer, as discussed in Section 5.3.2, and the contact force of each contact bond is the single output in the output layer. There are four hidden layers with the same neuron number in each layer, 810 for type I RVE with and 735 for type II REV. For the model for predicting stress, there are 53 or 48 2D feature vectors in the input layer. The target output is the stress the overall RVE $\sigma_{initial}$ when the initial crack occurs. Four hidden layers with the same neuron number in each layer are defined (530 for the type I RVE and 480 for the type II RVE). The setting of activation functions of the model is that the activation function used from the input layer to the first hidden layer and between any two hidden layers is the rectified linear activation function (ReLU), and the activation function applied between the last hidden layer and the output layer is the 'linear' function. The DNN predictive models presented above are finally determined after doing a set of trials of DNN models with different numbers of hidden layers and neurons, which has good performances in training and predicting processes.

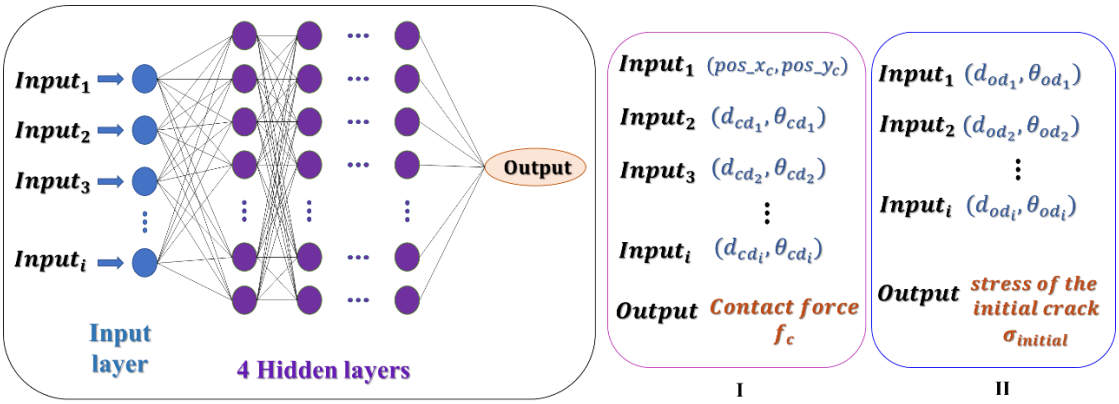

Figure 5-14: A back-propagation DNN model for predicting the initial crack and its stress.

5.4 Results and discussion

5.4.1. DNN predictive model for the initial crack and its stress of defective composite laminae with rectangular fibre distribution

The DNN model for predicting the initial crack in RVEs with the two periodic fibre distributions trained the amount of data extracted from 450 DEM simulations and tested the data from 50 DEM simulations. Two levels of evaluation criterions are used in the analysis. The accuracy of the models for the Type I RVE is shown in Table 5-1. The first criterion is that if the predicted initial crack (by DNN) is close to the one determined by the DEM model within a distance smaller or equal to the diameter of the ball (4.62e-4mm), the predicted crack is regarded as an accurate result. According to this criterion, the initial cracks in the 41 RVE samples can be predicted successfully, thus, the accuracy is 82% (41/50). It means that the DNN model can find out the highest contact force among 9400 contact bonds of each RVE successfully. Figure 5-15(a) shows the comparison of the DNN and DEM results of the contact forces. The black triangle at the bottom-left in Figure 5-15(a) is the predicted highest contact force, which is -44.94N.

The DEM simulated contact force of this contact bond is also the highest and is -48.13N. The position of this contact bond in the RVE is plotted as the black triangle in Figure 5-15(b), which shows that the DNN predicted initial crack is at exactly the same position as that of the DEM simulated initial crack.

The second criterion is that the DNN prediction can be treated as acceptable if the initial crack simulated by the DEM model is among the first five cracks predicted by the DNN model ordered by their contact forces. Based on the 2nd criterion, the initial cracks in the 47 RVEs can be successfully predicted, thus the accuracy of the DNN prediction increases to 94 %. For instance (Figure 5-15(c-d)), the initial crack predicted by the DEM model, is at position *M* in the RVE, which is the position with the second-highest contact force from the DNN prediction. Thus, by the 2nd criterion, it is acceptable as it is among the first five possible cracks. The first crack predicted by the DNN model is at position N in the RVE. Although it is not the exact position of the first crack predicted by the DEM model, it is found that the position is among the first 5 cracks to appear and will be merged with other cracks to form the final crack path predicted by the DEM model, as shown in Figure 5-15(e). Nevertheless, by the 2nd criterion, the DNN model can effectively predict positions with high fracture risk.

Table 5-1: DNN prediction results for the initial crack in type I RVEs.

Criterion	Result	Accuracy
Criterion 1: The DNN predicted crack is around the DEM simulated initial crack.	41	82%
Criterion 2: The contact bond around the DEM simulated initial crack is in the list of DNN-predicted cracks with the top five highest risks.	47	94%

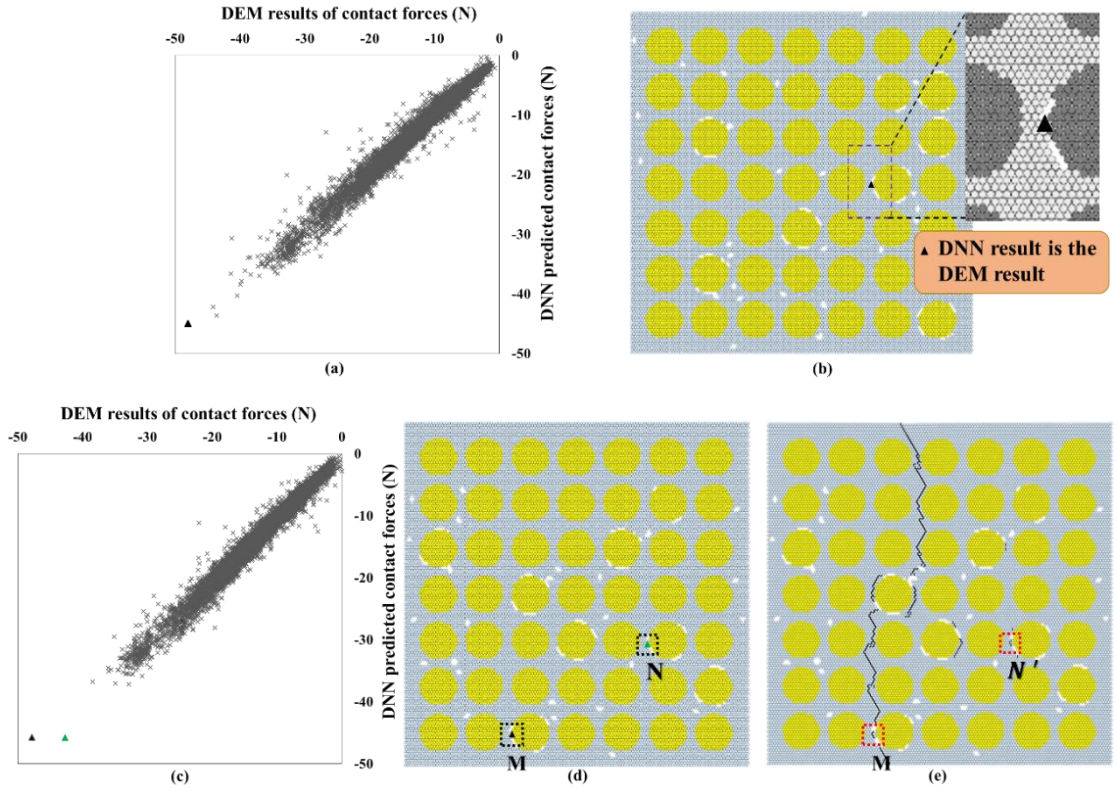

Figure 5-15: Two examples of the DNN predictions of the initial crack in RVEs with rectangular fibre distribution. (a-b) The DNN and DEM results for an example of criterion one. (c-e) The DNN and DEM results for an example of criterion two.

The stress at the initial cracking obtained from the DEM simulations and the DNN predictive model are plotted in Figure 5-16. The stresses predicted by the DNN are close to the ones predicted by the DEM. The average stresses from the DEM simulations and

the DNN predictions are 44.21MPa and 44.38MPa, respectively, with standard deviations of 1.85MPa and 1.25MPa. Therefore, it can be concluded that the trained DNN model can satisfactorily predict the stress when the initial crack occurs.

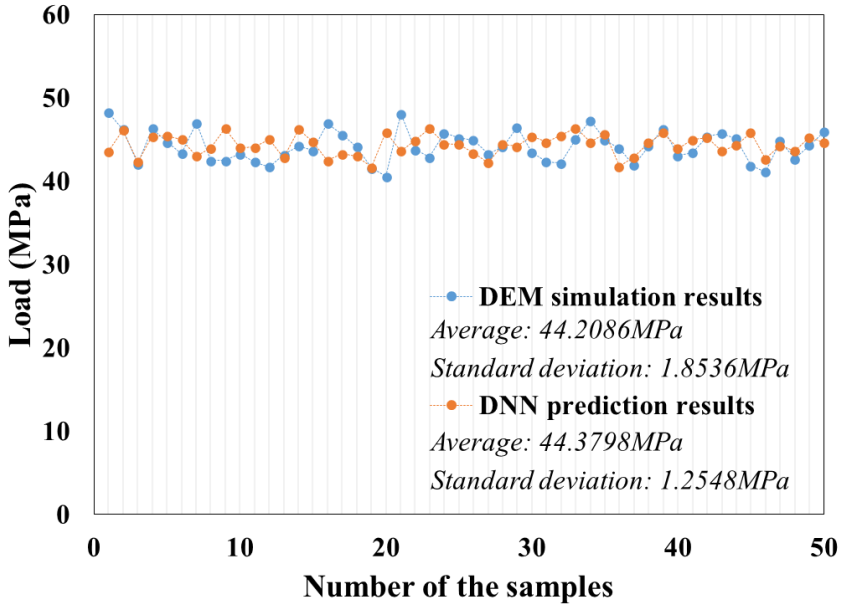

Figure 5-16: Comparison of predictions of the stress of RVE with rectangular fibre distribution from the DNN model to the DEM simulation results.

5.4.2. DNN predictive model for the initial crack and its stress of defective composite laminae with hexagonal fibre distribution

Similar to the discussion on the DNN predictions in the Type I RVE, the two criterions are also used to evaluate the performance of the DNN model (see Table 5-2) for the Type II RVE. Based on criterion 1, the initial cracks in the 40 Type II RVEs can be predicted with relatively high accuracy (40/50 = 80%), indicating that the highest contact force can be found by the DNN accurately. An example of this scenario is shown in Figure 5-17(a-b). The black triangle represents the highest contact force predicted by the DNN model, as shown in Figure 5-17(a), which is -46.34N. The position of the

initial crack is determined then by the position of the DNN predicted highest contact force by DNN, which is the same as the position obtained from the DEM model where the contact force is -45.14N. The position of this contact bond in the RVE is denoted by the black triangle in Figure 5-17(b).

Based on criterion 2, the initial cracks in the 47 Type II RVEs are predicted with an accuracy of 94% (47/50) by the DNN model. For instance (Figure 5-17(c-d)), the initial crack predicted by the DEM model, is at position *P*, which is the position with the fourth-highest contact force predicted by DNN. The first crack predicted by the DNN model is at position *Q* in the RVE. As observed in Type I RVEs, the position is also among the first five cracks to appear and will be merged with other cracks to form the final crack path predicted by the DEM model (see Figure 5-17(e)).

Table 5-2: DNN prediction results for the initial crack in type II RVEs.

Criterion	Result	Accuracy
Criterion 1: The DNN predicted crack is around the DEM simulated initial crack.	40	80%
Criterion 2: The contact bond around the DEM simulated initial crack is in the list of DNN-predicted cracks with the top five highest risks.	47	94%

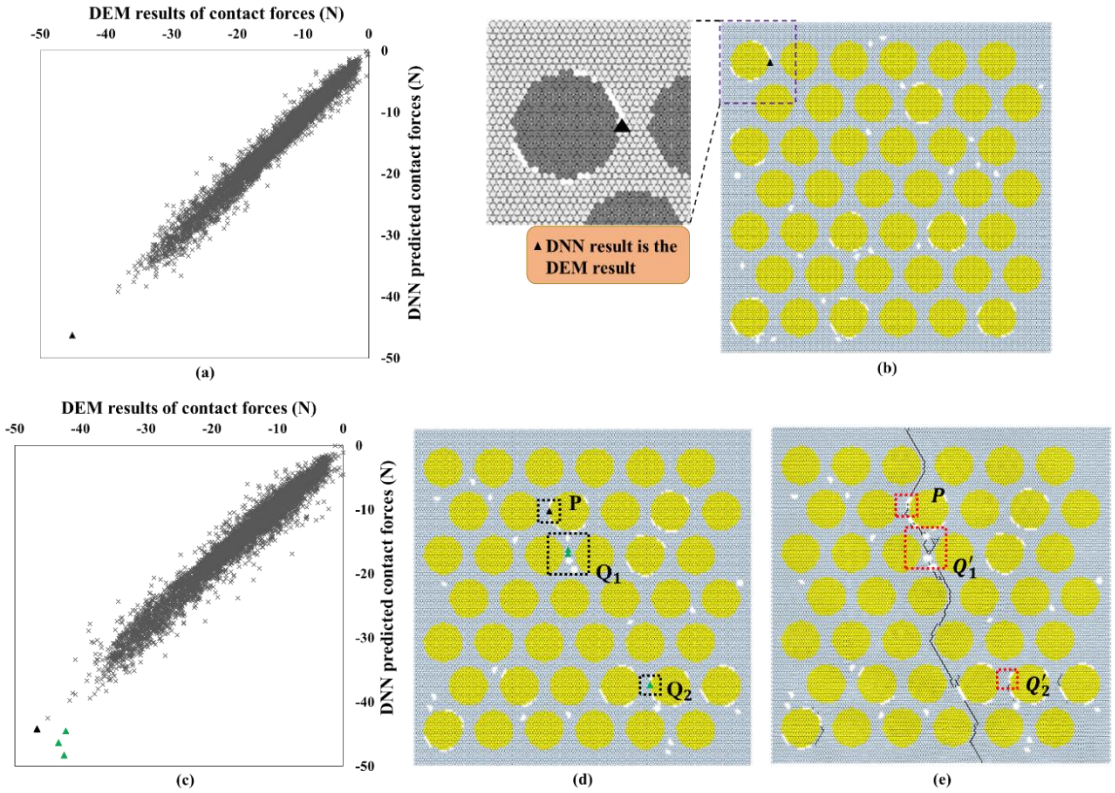

Figure 5-17: Two examples of the DNN predictions of the initial crack in RVEs with hexagonal fibre distribution. (a-b) The DNN and DEM results for an example of criterion one. (c-e) The DNN and DEM results for an example of criterion two.

Figure 5-18 presents the stress of the initial crack from the DEM results and the DNN predictions, which shows good agreement. The averages (46.35MPa and 45.99MPa) and standard deviations (2.84MPa and 1.51MPa) of the stresses obtained from the DEM and DNN are very close, which indicates that the trained DNN model can be used to provide a reliable result of the stress at initial cracking.

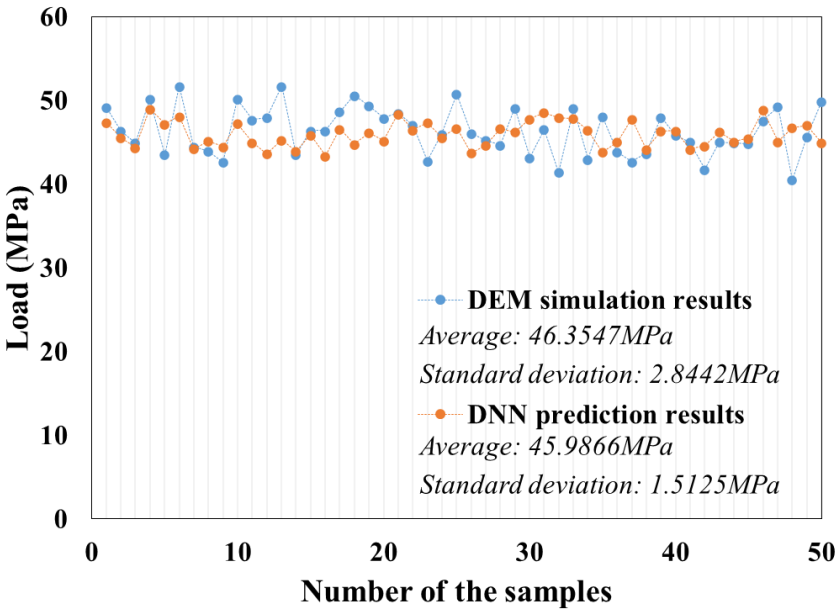

Figure 5-18: Comparison of predictions of the stress of RVE with hexagonal fibre distribution from the DNN model to the DEM simulation results.

5.5 Summary

In this chapter, an RVE-based DEM model has been developed to study the effect of defects on the transverse mechanical responses in UD FRP laminae. The defects in both the matrix and the fibre-matrix interfaces are considered. It can be found that the simulated crack path can very well fit the experimental test when randomly distributed defects are considered. The presence of defects affects the mechanical behaviours of both the stress-strain response and crack progression. Both the strength and the stiffness of the defective RVE are less than that of the defect-free RVE. The crack path is dependent on the distribution of the defects. The cracks often occur among fibre-matrix interfaces with a high density of defects. It is because of the stress concentration on the tip of the defects. It can also be found that the presence of defects causes a faster coalescence of cracks thus, the ultimate failure achieves earlier. The crack paths in the

RVEs with higher fibre volume fraction (60%) are more sensitive to the distribution and size of matrix defects. The crack paths in the RVEs with lower fibre volume fraction (45%) are more sensitive to the distribution of interfacial defects. In addition, the simulation results showed that the proportional distribution of the defects in the matrix and interface influences the tensile strength and stiffness significantly. It can be found that the strength and stiffness decreased with the increase in the proportion of interfacial defects.

Then, multi-layer DNN regression models with back-propagation are generated for the prediction of the position of the initial crack and its stress of defective FRP composite laminae with two periodic fibre distributions based on the data extracted from the results of the RVE-based DEM model. Considering the random distributions of both matrix and interfacial defects in the microstructures of RVEs, the developed DNN regression models show reasonably high prediction accuracies in predicting the position of the initial crack for both two periodic fibre arrangements. Based on criterion I, the accuracies are 82% and 80%, respectively. Based on criterion 2, both accuracies are 94%. On the other hand, the overall stress of the material at the time, when the initial crack occurs in the RVEs can be accurately predicted in both two types of RVEs.

Chapter 6

6 Conclusions and Future Works

6.1 Conclusions

In this thesis, a 2D RVE-based Discrete Element Method (DEM) model is first developed for modelling the mechanical behaviour of defect-free UD FRP composite laminae under the loading of transverse tension. RVEs of UD FRP laminae are generated based on experimentally validated sized fibres. A constant tensile velocity of 5 mm/s is applied simultaneously on the left and right boundaries of the RVE. The developed DEM model can accurately predict the transverse mechanical properties of the defect-free UD FRP lamina, as it can be validated with the results of the experimental tests. The DEM simulated stress-strain responses of RVEs are also compared with that of the FEM analyse, which shows a good agreement. The mechanical responses in the RVEs based on the different settings of fibre volume fractions (45% and 60%) are analysed. For the stress-strain response, the strength of the UD FRP lamina becomes larger with the increase of fibre volume fractions, however, the deformation until reaching the failure point becomes smaller. For tracking the crack initiation and propagation, the DEM simulation result shows that the crack usually occurs in the matrix where the distance between the two fibres is very small, which is caused by the stress concentration. Then the crack propagates in the RVE, and the final crack path occurs. Based on a large set of data generated from the microscale RVE-based DEM model, lastly, in Chapter 3, a four-layer DNN model with back-propagation is constructed for predicting two transverse mechanical properties (tensile strength and Young's modulus) of an FRP composite lamina at the macroscopic level with

consideration of two features related to the fibre distribution. Latin Hypercube sampling (LHS), one commonly used Design of Experiments (DoE) method, is implemented to generate 200 sets of two independent variables (fibre volume fraction and fibre radius) given their corresponding boundaries. Based on the 200 sets of variables, 2000 RVE-based DEM model simulations are generated for the training process and the testing process of the DNN model. The data is normalized using both Min-max normalization and Z-score normalization, and the analysis of the comparison of their performances in the predictive model is done. To validate as well as improve prediction performance, a 3-fold cross-validation is conducted. The DNN model shows good accuracies for predicting the two mechanical properties. The better performance of predicting the tensile strength is obtained by using the trained DNN model with the Min-max normalization method as the value of the performance indicator R^2 is higher. And the performance in the prediction of transverse Young's modulus, as indicated by the respective R^2 values obtained using the two different normalization methods, is not affected significantly by the normalization method. Additionally, the comparison among the DNN model and two existing analytical models for obtaining Young's modulus shows that the DNN model has its superiority, as the impact of the random fibre distribution and varied fibre diameters can be considered.

The simulated damage evolution of the FRP composites is accurate, however, it usually takes a long time and costs huge power of computing even if only to the initial crack. Thus, machine learning models are employed to understand the relationship between the microstructure of UD FRP composite laminae and its crack path and then predict the transverse cracks. In Chapter 4, two relatively simple and easily used ML models, Gaussian Naïve Bayes classifier and Artificial Neural Networks (ANNs) are first developed for predicting the crack path of the UD FRP lamina. The data used in

the ML models are extracted from the DEM simulations of 500 reduced-size RVE samples. Every single particle in the RVE is considered a data point. The target of this prediction problem is whether this particle is cracking or not. Undersampling, as a method for overcoming the problem of data imbalance, is employed on the data for deleting some data points that are not cracking. The training accuracies of both the Gaussian Naïve Bayes classifier and ANN are good, however, their prediction results show not very satisfied accuracy. In the training and testing processes of the ANN model, a 3-fold cross-validation is used. Three different ratios of training data (17.5%, 26%, and 40 %) are used in the training process. It is found that the accuracy of the training process increases by enlarging the number of training data**.** As the prediction performance is not very satisfactory, dropout is used, which gives a better prediction result than the original network.

An improved predictive model is then developed. Compared to the data size used in the previous two ML models, the data size is enlarged and based on the results of 1600 DEM simulations. A four-layer DNN model with back-propagation is constructed to predict the crack areas of an FRP composite lamina. It is shown that most initial cracks and the overall trend of cracking paths can be predicted successfully by the DNN model. Moreover, both occurrence of local crack areas and the cracking density of the RVE sample can be predicted accurately with full consideration of random fibre distribution.

In addition, for the purpose of a fast determination of the initial cracks in the UD FRP lamina, a DL prediction for the crack initiation of the UD FRP composite with random fibre distribution is investigated in the last part of Chapter 4. Two DNN models train a set of suitable and representative features obtained from the DEM simulations and then predict the initial and the second cracks in order. The input features in the DNN model for the initial crack are selected for representing the randomness of fibres

in each RVE, as the initial crack is highly dependent on the fibre distribution. The target output for predicting the initial crack is the contact force of the contact bond in the RVE. Two criterions are used for analysing the prediction performance of the initial crack. The first one is the DNN predicted crack is around the DEM simulated initial crack. The second one is the contact bond around the DEM simulated initial crack is in the lists of DNN predicted cracks with the top five highest risk. The accuracies according to the criterions are 65% and 92%, respectively. Then, new features based on the initial crack are added for the prediction of the second crack, which is the distance from the contact bond to the initial crack and its corresponding angle with x – axis. After training the model, the second cracks in 65 RVEs are predicted successfully, of which the accuracy is $92\% * 65\% \approx 60\%$. It is indicated that the problem of predicting the second crack is a bit complex based on the current input features. The relatively small data size may affect the training and test performance of the crack initiation prediction. Much more data obtained from the DEM simulations are needed to improve the accuracy of the prediction. The work presented in Chapter 4 shows a promising framework to predict the initial crack of UD FRP composite by combining the advantages of both DEM modelling and the DNN algorithm. The current results could demonstrate the feasibility and effectiveness of the method.

In Chapter 5, a DEM model for simulating the effect of defects on the transverse mechanical responses in UD FRP laminae with the rectangular arrangement of fibres (type I), the hexagonal arrangement of fibres (type II) and the random arrangement of fibres (type III) are validated developed. The defects in both the matrix and the fibre-matrix interfaces are considered. The defects in the matrix and along fibre-matrix interfaces are randomly distributed, which is implemented using a function in Python. It is found that the presence of matrix and interfacial defects in the composite laminae

reduced the tensile strength and affected the form of damage progression. The cracks often occur among fibre-matrix interfaces with a high density of defects due to the stress concentration on the tip of the defects. It is also found that the crack paths of RVEs are different caused by the radii of the defects and their locations. The crack propagation depends much more on the distribution of fibre-matrix interfacial defects. In addition, the proportional distribution of the defects in the matrix and interface in the RVE influences the strength and stiffness. It can be concluded that both the strength and stiffness are decreased with the increase in the proportion of interfacial defects. Next, DNN is used to verify that the initial crack is closely related to the distribution of defects. In this way, the trained DNN can also help to obtain the initial crack and its corresponding load effectively. Totally 1000 samples for type I and type II RVEs with randomly distributed defects are generated and simulated by the DEM model. The DNN regression models show reasonably high prediction accuracies in predicting the the initial crack according to two criterions. Based on criterion I, the accuracies of the two types of RVEs are 82% and 80%, respectively. Based on criterion 2, both accuracies are 94%. The predicted overall stress at the time when the initial crack occurs in the RVEs in both two types of RVEs, is accurate and reliable as indicated by the respective average and standard deviation of the DEM and DNN predicted results.

The machine learning application in the predictions of mechanical behaviour of the UD FRP laminae based on the data of DEM simulation shows its efficiency and accuracy. After training the predictive model using the data extracted from the DEM simulations, an accurate result can be obtained in less than one second by the predictive model rather than requiring an approximately 5-hour DEM simulation.

6.2 Suggestions for Future Works

In terms of the DEM model, it can be found that the 2D RVE-based DEM has powerful ability and reliable computing for studying the transverse behaviour of both defect-free and defective UD FRP laminae. However, it would be better if the 2D DEM model could be extended to a 3D model to study mechanical behaviour more comprehensively and accurately. Additionally, the study on the effects of defects in the mechanical response of the lamina is expanded to biaxial loading.

The study on crack prediction can reflect that the DNN model, which is a black-box deep learning model, has the power to capture the complex intrinsic relations between the inputs and the outputs without imposing any assumptions or simplifications for such a complex and challenging prediction problem. The results of the DNN model for the initial crack demonstrate the feasibility and effectiveness of the deep learning prediction. Therefore, combining the advantages of DEM modelling and the deep learning algorithm for fracture mechanics may provide new avenues to design engineering materials, for instance, high-performance composites, and how these materials respond to various scenarios of crack propagation.

References

[1] Clyne TW, Hull D. An introduction to composite materials: Cambridge university press, 2019.

[2] Sanjay M, Arpitha G, Naik LL, Gopalakrishna K, Yogesha B. Applications of natural fibers and its composites: An overview. Natural Resources. 2016;7:108-14.

[3] Marsh G. Composites get in deep with new-generation engine. Reinforced plastics. 2006;50:26-9.

[4] Spitalsky Z, Tasis D, Papagelis K, Galiotis C. Carbon nanotube–polymer composites: chemistry, processing, mechanical and electrical properties. Progress in polymer science. 2010;35:357-401.

[5] Gay D, Hoa SV. Composite materials: design and applications: CRC press, 2007.

[6] Chung DD. Composite materials: science and applications: Springer Science & Business Media, 2010.

[7] Heidari-Rarani M, Bashandeh-Khodaei-Naeini K, Mirkhalaf S. Micromechanical modeling of the mechanical behavior of unidirectional composites–A comparative study. Journal of Reinforced Plastics and Composites. 2018;37:1051-71.

[8] Affdl JH, Kardos J. The Halpin-Tsai equations: a review. Polymer Engineering & Science. 1976;16:344-52.

[9] Halpin J, Tsai S. Environmental factors in composite materials design. US Air Force Technical Report AFML TR. 1967;67423.

[10] Huang Z-m. Micromechanical prediction of ultimate strength of transversely isotropic fibrous composites. International journal of solids and structures. 2001;38:4147-72.

[11] Hill R. Elastic properties of reinforced solids: some theoretical principles. Journal of the Mechanics and Physics of Solids. 1963;11:357-72.

[12] Swaminathan S, Ghosh S, Pagano N. Statistically equivalent representative volume elements for unidirectional composite microstructures: Part I-Without damage. Journal of Composite materials. 2006;40:583-604.

[13] Totry E, Molina-Aldareguía JM, González C, LLorca J. Effect of fiber, matrix and interface properties on the in-plane shear deformation of carbon-fiber reinforced composites. Composites Science and Technology. 2010;70:970-80.

[14] Vaughan T, McCarthy C. A micromechanical study on the effect of intra-ply properties on transverse shear fracture in fibre reinforced composites. Composites Part A: Applied Science and Manufacturing. 2011;42:1217-28.

[15] Yang L, Yan Y, Liu Y, Ran Z. Microscopic failure mechanisms of fiber-reinforced polymer composites under transverse tension and compression. Composites Science and Technology. 2012;72:1818-25.

[16] Vaughan T, McCarthy C. A combined experimental–numerical approach for generating statistically equivalent fibre distributions for high strength laminated composite materials. Composites Science and Technology. 2010;70:291-7.

[17] Hojo M, Mizuno M, Hobbiebrunken T, Adachi T, Tanaka M, Ha SK. Effect of fiber array irregularities on microscopic interfacial normal stress states of transversely loaded UD-CFRP from viewpoint of failure initiation. Composites Science and Technology. 2009;69:1726-34.

[18] Romanov V, Lomov SV, Swolfs Y, Orlova S, Gorbatikh L, Verpoest I. Statistical analysis of real and simulated fibre arrangements in unidirectional composites. Composites Science and Technology. 2013;87:126-34.

[19] Buryachenko V, Pagano N, Kim R, Spowart J. Quantitative description and numerical simulation of random microstructures of composites and their effective elastic moduli. International journal of solids and structures. 2003;40:47-72.

[20] Wongsto A, Li S. Micromechanical FE analysis of UD fibre-reinforced composites with fibres distributed at random over the transverse cross-section. Composites Part A: Applied Science and Manufacturing. 2005;36:1246-66.

[21] Melro A, Camanho P, Pinho S. Generation of random distribution of fibres in long-fibre reinforced composites. Composites Science and Technology. 2008;68:2092-102.

[22] Yang L, Yan Y, Ran Z, Liu Y. A new method for generating random fibre distributions for fibre reinforced composites. Composites Science and Technology. 2013;76:14-20.

[23] Ismail Y, Yang D, Ye J. Discrete element method for generating random fibre distributions in micromechanical models of fibre reinforced composite laminates. Composites Part B: Engineering. 2016;90:485-92.

[24] Sun C-T, Vaidya RS. Prediction of composite properties from a representative volume element. Composites Science and Technology. 1996;56:171-9.

[25] Gusev AA, Hine PJ, Ward IM. Fiber packing and elastic properties of a transversely random unidirectional glass/epoxy composite. Composites Science and Technology. 2000;60:535-41.

[26] Li S. General unit cells for micromechanical analyses of unidirectional composites. Composites Part A: Applied Science and Manufacturing. 2001;32:815-26.

[27] Zhang Y, Xia Z, Ellyin F. Nonlinear viscoelastic micromechanical analysis of fibre-reinforced polymer laminates with damage evolution. International journal of solids and structures. 2005;42:591-604.

[28] González C, LLorca J. Mechanical behavior of unidirectional fiber-reinforced polymers under transverse compression: microscopic mechanisms and modeling. Composites Science and Technology. 2007;67:2795-806.

[29] Wang X, Zhang J, Wang Z, Zhou S, Sun X. Effects of interphase properties in unidirectional fiber reinforced composite materials. Materials & Design. 2011;32:3486-92.

[30] Vaughan T, McCarthy C. Micromechanical modelling of the transverse damage behaviour in fibre reinforced composites. Composites Science and Technology. 2011;71:388-96.

[31] Naderi M, Apetre N, Iyyer N. Effect of interface properties on transverse tensile response of fiber-reinforced composites: Three-dimensional micromechanical modeling. Journal of Composite materials. 2017;51:2963-77.

[32] Ghayoor H, Hoa SV, Marsden CC. A micromechanical study of stress concentrations in composites. Composites Part B: Engineering. 2018;132:115-24.

[33] Olivier P, Cottu J, Ferret B. Effects of cure cycle pressure and voids on some mechanical properties of carbon/epoxy laminates. Composites. 1995;26:509-15.

[34] Kang MK, Lee WI, Hahn HT. Formation of microvoids during resin-transfer molding process. Composites Science and Technology. 2000;60:2427-34.

[35] Kuentzer N, Simacek P, Advani SG, Walsh S. Correlation of void distribution to VARTM manufacturing techniques. Composites Part A: Applied Science and Manufacturing. 2007;38:802-13.

[36] Strong AB. Fundamentals of composites manufacturing: materials, methods and applications: Society of manufacturing engineers, 2008.

[37] Stone D, Clarke B. Ultrasonic attenuation as a measure of void content in carbon-fibre reinforced plastics. Non-destructive testing. 1975;8:137-45.

[38] Costa ML, De Almeida SfM, Rezende MC. The influence of porosity on the interlaminar shear strength of carbon/epoxy and carbon/bismaleimide fabric laminates. Composites Science and Technology. 2001;61:2101-8.

[39] Hagstrand P-O, Bonjour F, Månson J-A. The influence of void content on the structural flexural performance of unidirectional glass fibre reinforced polypropylene composites. Composites Part A: Applied Science and Manufacturing. 2005;36:705-14.

[40] Suarez J, Molleda F, Guemes A. Void content in carbon fibre/epoxy resin composites and its effects on compressive properties. ICCM/9 Composites: Properties and Applications. 1993;6:589-96.

[41] Hapke J, Gehrig F, Huber N, Schulte K, Lilleodden E. Compressive failure of UD-CFRP containing void defects: In situ SEM microanalysis. Composites Science and Technology. 2011;71:1242-9.

[42] Chew H, Guo T, Cheng L. Effects of pressure-sensitivity and plastic dilatancy on void growth and interaction. International journal of solids and structures. 2006;43:6380-97.

[43] Moraleda J, Segurado J, Llorca J. Finite deformation of porous elastomers: a computational micromechanics approach. Philosophical Magazine. 2007;87:5607-27.

[44] Liebig WV, Viets C, Schulte K, Fiedler B. Influence of voids on the compressive failure behaviour of fibre-reinforced composites. Composites Science and Technology. 2015;117:225-33.

[45] Vajari DA, González C, Llorca J, Legarth BN. A numerical study of the influence of microvoids in the transverse mechanical response of unidirectional composites. Composites Science and Technology. 2014;97:46-54.

[46] Vajari DA. A micromechanical study of porous composites under longitudinal shear and transverse normal loading. Composite Structures. 2015;125:266-76.

[47] Danzi F, Fanteria D, Panettieri E, Palermo M. A numerical micro-mechanical study of the influence of fiber–matrix interphase failure on carbon/epoxy material properties. Composite Structures. 2017;159:625-35.

[48] Cundall PA, Strack OD. A discrete numerical model for granular assemblies. geotechnique. 1979;29:47-65.

[49] Potyondy DO, Cundall P. A bonded-particle model for rock. International journal of rock mechanics and mining sciences. 2004;41:1329-64.

[50] Ghaboussi J, Barbosa R. Three-dimensional discrete element method for granular materials. International Journal for Numerical and Analytical Methods in Geomechanics. 1990;14:451-72.

[51] Mishra B, Rajamani RK. The discrete element method for the simulation of ball mills. Applied Mathematical Modelling. 1992;16:598-604.

[52] Camborde F, Mariotti C, Donzé F. Numerical study of rock and concrete behaviour by discrete element modelling. Computers and geotechnics. 2000;27:225-47.

[53] Hentz S, Daudeville L, Donzé FV. Identification and validation of a discrete element model for concrete. Journal of engineering mechanics. 2004;130:709-19.

[54] Abbas A, Masad E, Papagiannakis T, Harman T. Micromechanical modeling of the viscoelastic behavior of asphalt mixtures using the discrete-element method. International journal of geomechanics. 2007;7:131-9.

[55] Tavarez FA, Plesha ME. Discrete element method for modelling solid and particulate materials. International Journal for Numerical Methods in Engineering. 2007;70:379-404.

[56] Li X, He S, Luo Y, Wu Y. Discrete element modeling of debris avalanche impact on retaining walls. Journal of Mountain Science. 2010;7:276-81.

[57] Iliescu D, Gehin D, Iordanoff I, Girot F, Gutiérrez M. A discrete element method for the simulation of CFRP cutting. Composites Science and Technology. 2010;70:73-80.

[58] Itasca C. PFC2D (particle Flow Code in 2-dimensions), Version 3.10. 2004.

[59] Ma Y, Huang H. DEM analysis of failure mechanisms in the intact Brazilian test. International journal of rock mechanics and mining sciences. 2018;102:109-19.

[60] Bathe K-J, Wilson EL. Numerical methods in finite element analysis: Prentice Hall, 1976.

[61] Yang D, Sheng Y, Ye J, Tan Y. Discrete element modeling of the microbond test of fiber reinforced composite. Computational Materials Science. 2010;49:253-9.

[62] Sheng Y, Yang D, Tan Y, Ye J. Microstructure effects on transverse cracking in composite laminae by DEM. Composites Science and Technology. 2010;70:2093-101.

[63] Yang D, Ye J, Tan Y, Sheng Y. Modeling progressive delamination of laminated composites by discrete element method. Computational Materials Science. 2011;50:858-64.

[64] Yang D, Sheng Y, Ye J, Tan Y. Dynamic simulation of crack initiation and propagation in cross-ply laminates by DEM. Composites Science and Technology. 2011;71:1410-8.

[65] Maheo L, Dau F, Andre D, Charles J-L, Iordanoff I. A promising way to model cracks in composite using Discrete Element Method. Composites Part B: Engineering. 2015;71:193-202.

[66] Hebb DO. The Organization of Behavior: A Psychological Theory: Wiley New York, 1949.

[67] Singh J. Big data analytic and mining with machine learning algorithm. Int J Inform Comput Technol. 2014;4:33-40.

[68] Gupta R, Tanwar S, Tyagi S, Kumar N. Machine learning models for secure data analytics: A taxonomy and threat model. Computer Communications. 2020;153:406-40.

[69] Schmitt J, Bönig J, Borggräfe T, Beitinger G, Deuse J. Predictive model-based quality inspection using Machine Learning and Edge Cloud Computing. Advanced engineering informatics. 2020;45:101101.

[70] Gauerhof L, Munk P, Burton S. Structuring validation targets of a machine learning function applied to automated driving. International Conference on Computer Safety, Reliability, and Security: Springer; 2018. p. 45-58.

[71] Burton S, Gauerhof L, Heinzemann C. Making the case for safety of machine learning in highly automated driving. International Conference on Computer Safety, Reliability, and Security: Springer; 2017. p. 5-16.

[72] Wu M, Chen L. Image recognition based on deep learning. 2015 Chinese Automation Congress (CAC): IEEE; 2015. p. 542-6.

[73] Fujiyoshi H, Hirakawa T, Yamashita T. Deep learning-based image recognition for autonomous driving. IATSS research. 2019;43:244-52.

[74] Chowdhury A, Kautz E, Yener B, Lewis D. Image driven machine learning methods for microstructure recognition. Computational Materials Science. 2016;123:176-87.

[75] Sharma A, Mukhopadhyay T, Rangappa SM, Siengchin S, Kushvaha V. Advances in computational intelligence of polymer composite materials: machine learning assisted modeling, analysis and design. Archives of Computational Methods in Engineering. 2022:1-45.

[76] Ayodele TO. Types of machine learning algorithms. New advances in machine learning. 2010;3:19-48.

[77] Caruana R, Niculescu-Mizil A. An empirical comparison of supervised learning algorithms. Proceedings of the 23rd international conference on Machine learning2006. p. 161-8.

[78] Celebi ME, Aydin K. Unsupervised learning algorithms: Springer, 2016.

[79] Hastie T, Tibshirani R, Friedman J. Unsupervised learning. The elements of statistical learning: Springer; 2009. p. 485-585.

[80] Stein M. Large sample properties of simulations using Latin hypercube sampling. Technometrics. 1987;29:143-51.

[81] Loh W-L. On Latin hypercube sampling. The annals of statistics. 1996;24:2058-80.

[82] Kempthorne O. The design and analysis of experiments. 1952.

[83] Fang K-T, Lin DK, Winker P, Zhang Y. Uniform design: theory and application. Technometrics. 2000;42:237-48.

[84] de Aguiar PF, Bourguignon B, Khots M, Massart D, Phan-Than-Luu R. D-optimal designs. Chemometrics and intelligent laboratory systems. 1995;30:199-210.

[85] Owen AB. Orthogonal arrays for computer experiments, integration and visualization. Statistica Sinica. 1992:439-52.

[86] Alam FM, McNaught KR, Ringrose TJ. A comparison of experimental designs in the development of a neural network simulation metamodel. Simulation Modelling Practice and Theory. 2004;12:559-78.

[87] Gu Z, Liu Y, Hughes DJ, Ye J, Hou X. A parametric study of adhesive bonded joints with composite material using black-box and grey-box machine learning methods: Deep neuron networks and genetic programming. Composites Part B: Engineering. 2021;217:108894.

[88] Rajmohan T, Palanikumar K. Application of the central composite design in optimization of machining parameters in drilling hybrid metal matrix composites. Measurement. 2013;46:1470-81.

[89] Raja RS, Manisekar K. Experimental and statistical analysis on mechanical properties of nano flyash impregnated GFRP composites using central composite design method. Materials & Design. 2016;89:884-92.

[90] Wang GG, Shan S. Review of metamodeling techniques for product design with computation-intensive processes. Proceedings of the Canadian Engineering Education Association (CEEA). 2005.

[91] Basavarajappa S, Arun K, Davim JP. Effect of filler materials on dry sliding wear behavior of polymer matrix composites–a Taguchi approach. Journal of minerals and materials characterization and engineering. 2009;8:379.

[92] Zhang SL, Zhang ZX, Xin ZX, Pal K, Kim JK. Prediction of mechanical properties of polypropylene/waste ground rubber tire powder treated by bitumen composites via uniform design and artificial neural networks. Materials & Design. 2010;31:1900-5.

[93] Rajmohan T, Palanikumar K. Modeling and analysis of performances in drilling hybrid metal matrix composites using D-optimal design. The International journal of advanced Manufacturing technology. 2013;64:1249-61.

[94] Johnston J, Chattopadhyay A. Effect of material variability on multiscale modeling of rate-dependent composite materials. Journal of Aerospace Engineering. 2015;28:04015003.

[95] Dey S, Mukhopadhyay T, Adhikari S. Metamodel based high-fidelity stochastic analysis of composite laminates: A concise review with critical comparative assessment. Composite Structures. 2017;171:227-50.

[96] Liu Y, Liu K, Gao Z, Yao Y, Sfarra S, Zhang H, et al. Non-destructive defect evaluation of polymer composites via thermographic data analysis: A manifold learning method. Infrared Physics & Technology. 2019;97:300-8.

[97] Balreira DS, Moura LA, Parente Jr E. Sequential approximate optimization of composite structures using radial basis functions. Proceedings of the 4th Brazilian Conference on Composite Materials, Pontifícia Universidade Católica do Rio de2018. p. 939-46.

[98] Blum AL, Langley P. Selection of relevant features and examples in machine learning. Artificial intelligence. 1997;97:245-71.

[99] He H, Garcia EA. Learning from imbalanced data. IEEE Transactions on knowledge and data engineering. 2009;21:1263-84.

[100] Johnson JM, Khoshgoftaar TM. The effects of data sampling with deep learning and highly imbalanced big data. Information Systems Frontiers. 2020;22:1113-31.

[101] Krawczyk B. Learning from imbalanced data: open challenges and future directions. Progress in Artificial Intelligence. 2016;5:221-32.

[102] Patro S, Sahu KK. Normalization: A preprocessing stage. arXiv preprint arXiv:150306462. 2015.

[103] Kotsiantis SB, Zaharakis I, Pintelas P. Supervised machine learning: A review of classification techniques. Emerging artificial intelligence applications in computer engineering. 2007;160:3-24.

[104] Sen PC, Hajra M, Ghosh M. Supervised classification algorithms in machine learning: A survey and review. Emerging technology in modelling and graphics: Springer; 2020. p. 99-111.

[105] Rodriguez-Galiano V, Sanchez-Castillo M, Chica-Olmo M, Chica-Rivas M. Machine learning predictive models for mineral prospectivity: An evaluation of neural networks, random forest, regression trees and support vector machines. Ore Geology Reviews. 2015;71:804-18.

[106] Diskin M. Definition and uses of the linear regression model. Water Resources Research. 1970;6:1668-73.

[107] Duda RO, Hart PE, Stork DG. Pattern classification and scene analysis: Wiley New York, 1973.

[108] Kononenko I. Comparison of inductive and naive Bayesian learning approaches to automatic knowledge acquisition: Current trends in knowledge acquisition. IOS Press, 1990.

[109] Rish I. An empirical study of the naive Bayes classifier. IJCAI 2001 workshop on empirical methods in artificial intelligence2001. p. 41-6.

[110] John GH, Langley P. Estimating continuous distributions in Bayesian classifiers. Proceedings of the Eleventh conference on Uncertainty in artificial intelligence: Morgan Kaufmann Publishers Inc.; 1995. p. 338-45.

[111] Hkdh B. Neural networks in materials science. ISIJ international. 1999;39:966-79.

[112] Zhang Z, Friedrich K. Artificial neural networks applied to polymer composites: a review. Composites Science and Technology. 2003;63:2029-44.

[113] El Kadi H. Modeling the mechanical behavior of fiber-reinforced polymeric composite materials using artificial neural networks—A review. Composite Structures. 2006;73:1-23.

[114] Liu X, Tian S, Tao F, Yu W. A review of artificial neural networks in the constitutive modeling of composite materials. Composites Part B: Engineering. 2021;224:109152.

[115] LeCun Y, Bengio Y, Hinton G. Deep learning. nature. 2015;521:436-44.

[116] Wang S-C. Artificial neural network. Interdisciplinary computing in java programming: Springer; 2003. p. 81-100.

[117] Chicco D, Warrens MJ, Jurman G. The coefficient of determination R-squared is more informative than SMAPE, MAE, MAPE, MSE and RMSE in regression analysis evaluation. PeerJ Computer Science. 2021;7:e623.

[118] Townsend JT. Theoretical analysis of an alphabetic confusion matrix. Perception & Psychophysics. 1971;9:40-50.

[119] Refaeilzadeh P, Tang L, Liu H. Cross-validation. Encyclopedia of database systems. 2009;5:532-8.

[120] Browne MW. Cross-validation methods. Journal of mathematical psychology. 2000;44:108-32.

[121] Arlot S, Celisse A. A survey of cross-validation procedures for model selection. Statistics surveys. 2010;4:40-79.

[122] Liu X, Gasco F, Goodsell J, Yu W. Initial failure strength prediction of woven composites using a new yarn failure criterion constructed by deep learning. Composite Structures. 2019;230:111505.

[123] Chen G, Wang H, Bezold A, Broeckmann C, Weichert D, Zhang L. Strengths prediction of particulate reinforced metal matrix composites (PRMMCs) using direct method and artificial neural network. Composite Structures. 2019;223:110951.

[124] Rahman A, Deshpande P, Radue MS, Odegard GM, Gowtham S, Ghosh S, et al. A machine learning framework for predicting the shear strength of carbon nanotube-polymer interfaces based on molecular dynamics simulation data. Composites Science and Technology. 2021;207:108627.

[125] Xu B-W, Ye S, Li M, Zhao H-P, Feng X-Q. Deep learning method for predicting the strengths of microcracked brittle materials. Engineering fracture mechanics. 2022:108600.

[126] Liu J, Zhang Y, Zhang Y, Kitipornchai S, Yang J. Machine learning assisted prediction of mechanical properties of graphene/aluminium nanocomposite based on molecular dynamics simulation. Materials & Design. 2022;213:110334.

[127] Zhou Y, Zheng S, Huang Z, Sui L, Chen Y. Explicit neural network model for predicting FRP-concrete interfacial bond strength based on a large database. Composite Structures. 2020;240:111998.

[128] Jahangir H, Eidgahee DR. A new and robust hybrid artificial bee colony algorithm–ANN model for FRP-concrete bond strength evaluation. Composite Structures. 2021;257:113160.

[129] Yuan M, Zhao H, Xie Y, Ren H, Tian L, Wang Z, et al. Prediction of stiffness degradation based on machine learning: Axial elastic modulus of [0m/90n] s composite laminates. Composites Science and Technology. 2022;218:109186.

[130] Pathan M, Ponnusami S, Pathan J, Pitisongsawat R, Erice B, Petrinic N, et al. Predictions of the mechanical properties of unidirectional fibre composites by supervised machine learning. Scientific reports. 2019;9:1-10.

[131] Yao L, Shao X, Feng Q. Predicting the mechanical properties of unidirectional fiber reinforced plastics from fiber and resin properties using data mining. Computational Materials Science. 2020;185:109986.

[132] Moore BA, Rougier E, O'Malley D, Srinivasan G, Hunter A, Viswanathan H. Predictive modeling of dynamic fracture growth in brittle materials with machine learning. Computational Materials Science. 2018;148:46-53.

[133] Hunter A, Moore BA, Mudunuru M, Chau V, Tchoua R, Nyshadham C, et al. Reduced-order modeling through machine learning and graph-theoretic approaches for brittle fracture applications. Computational Materials Science. 2019;157:87-98.

[134] Schwarzer M, Rogan B, Ruan Y, Song Z, Lee DY, Percus AG, et al. Learning to fail: Predicting fracture evolution in brittle material models using recurrent graph convolutional neural networks. Computational Materials Science. 2019;162:322-32.

[135] Hsu Y-C, Yu C-H, Buehler MJ. Using deep learning to predict fracture patterns in crystalline solids. Matter. 2020;3:197-211.

[136] Elapolu MS, Shishir MIR, Tabarraei A. A novel approach for studying crack propagation in polycrystalline graphene using machine learning algorithms. Computational Materials Science. 2022;201:110878.

[137] Sepasdar R, Karpatne A, Shakiba M. A data-driven approach to full-field nonlinear stress distribution and failure pattern prediction in composites using deep learning. Computer Methods in Applied Mechanics and Engineering. 2022;397:115126.

[138] Kačianauskas R, Vadluga V. Lattice-based six-spring discrete element model for discretisation problems of 2D isotropic and anisotropic solids. Mechanics. 2009;76:11-9.

[139] Ismail Y, Sheng Y, Yang D, Ye J. Discrete element modelling of unidirectional fibre-reinforced polymers under transverse tension. Composites Part B: Engineering. 2015;73:118-25.

[140] Labuz JF, Zang A. Mohr–Coulomb failure criterion. Rock mechanics and rock engineering. 2012;45:975-9.

[141] Soden PD, Hinton MJ, Kaddour A. Lamina properties, lay-up configurations and loading conditions for a range of fibre reinforced composite laminates. Failure criteria in fibre-reinforced-polymer composites: Elsevier; 2004. p. 30-51.

[142] Thomason J. The influence of fibre length, diameter and concentration on the modulus of glass fibre reinforced polyamide 6, 6. Composites Part A: Applied Science and Manufacturing. 2008;39:1732-8.

[143] Langtangen HP, Langtangen HP. A primer on scientific programming with Python: Springer, 2011.

[144] Gulli A, Pal S. Deep learning with Keras: Packt Publishing Ltd, 2017.

[145] CX Ling VS. Class imbalance problem. Encyclopedia of Machine Learning and Data Mining. 2017.

[146] Srivastava N, Hinton G, Krizhevsky A, Sutskever I, Salakhutdinov R. Dropout: a simple way to prevent neural networks from overfitting. The journal of machine learning research. 2014;15:1929-58.

[147] N Kuentzer PS, SG Advani, S Walsh. Correlation of void distribution to VARTM manufacturing techniques. 2007.

[148] Vajari D. A micromechanical study of porous composites under longitudinal shear and transverse normal loading. 2015

[149] Hernández S, Sket F, Molina-Aldareguı J, González C, LLorca J. Effect of curing cycle on void distribution and interlaminar shear strength in polymer-matrix composites. Composites Science and Technology. 2011;71:1331-41.

[150] Liu Y, Qi Z, Chen W, Li J, Wang E. Mesh Size Optimization of Unidirectional Fiber-Reinforced Composite Model for Precisely Characterizing the Effective Elastic Property. Journal of Materials Engineering and Performance. 2020;29:2707-19.

[151] Gamstedt K. Fatigue damage mechanisms in polymer matrix composites: Luleå tekniska universitet, 1997.

[152] Vejen N, Pyrz R. Transverse crack growth in glass/epoxy composites with exactly positioned long fibres. Part I: experimental. Composites Part B: Engineering. 2001;32:557-64.